Doctoral Dissertation

Study of Charge States of Oxygen Adatoms on Rutile TiO_2(110) Surface by Atomic Force Microscopy and Kelvin Probe Force Microscopy

Quanzhen Zhang

December 2019

Graduate School of Engineering,
Osaka University

Abstract

Catalytic reaction based on noble metal nanoclusters on transition metal oxides has fascinated the scientific community for several decades, and it has been widely used in many applications and electronic devices. The prototypical catalytic system of Au nanoclusters on rutile TiO_2 is drawing extraordinary research interest, because of its high catalytic efficiency. In the Au/TiO_2 catalytic system, the physicochemical and electronic properties of the point defects, the adsorbed oxygen adatoms and the Au nanoclusters on rutile TiO_2 can dramatically determine the catalytic activity, which have been investigated by a lot of experimental and theoretical works. However, a large amount of researches about the catalytic reactants have still remained investigation topics, and the catalytic mechanism has not been fully understood yet. It is of high importance to clarify and manipulate the electronic properties of the oxygen adatoms and Au nanoclusters on rutile TiO_2 surface, experimentally and theoretically.

In this doctoral dissertation, I focused on the investigation of charge states of oxygen adatoms on rutile TiO_2(110) surface by noncontact atomic force microscopy and Kelvin probe force microscopy with atomic resolution at 78 K. Firstly, the charge states of the oxygen adatoms were experimentally clarified with atomic resolution for the first time, and the oxygen adatoms were assigned with one and two electrons charged, respectively, depending on the different image contrast. In addition, we measured the values of short-range force and local contact potential difference as a function of tip-sample distance to distinguish the different charge states of the oxygen adatoms. Secondly, we proposed and demonstrated several strategies to manipulate the charge states of oxygen adatoms. For example, the charge states of the oxygen adatoms could be reversibly switched by applying the bias voltage with different polarities and by changing the tip-sample distance,

respectively. Thirdly, the conductance states of the oxygen adatoms were investigated depending on its different charge states. We demonstrated that the oxygen adatoms charged by one electron had higher conductance state than that of charged by two electrons, and the conductance behavior of the oxygen adatoms could be reversibly switched between high and low conductance states by manipulating its charge states. In the transition process of the charge state and conductance state of the oxygen adatoms, we proposed that the manipulation mechanism of the reversible switching process was attributed to the tunneling electrons accompanied with the local electric field effects. Fourthly, we demonstrated that the subsurface hydrogen on rutile TiO_2(110) could be characterized by simultaneous multi imaging method with atomic resolution. Four different configurations of the subsurface hydrogen were observed and distinguished with different atomic structures. Moreover, for the first time, the charge distribution of subsurface hydrogen was experimentally clarified to be localized around the nearby subsurface Ti atoms. Besides characterization, we demonstrated that the subsurface hydrogen could be reversibly migrated between the surface and subsurface layers by the voltage pulse with different polarities. Lastly, the charge states of the Au nanoclusters on oxidized rutile TiO_2(110) surface were demonstrated, and the charge transfer between the Au nanoclusters and oxygen adatoms was experimentally clarified. Our present work could contribute to investigation of the catalytic mechanism of the catalytic reactions based on noble metal catalysts on transition metal oxides.

Contents

Chapter 1 Introduction

1.1 Background

1.1.1 Surface science and catalysis

Surface science is a wide research topic and has attracted the research interest of the scientific community for several decades. [1-4] Generally, surface science is a study that mainly focus on the chemical and physical reactions and corresponding phenomena occurring on the interface of two phases, such as the liquid-solid, liquid-gas and solid-liquid interfaces. The study of surface science now is usually divided into two common subjects: surface physics and surface chemistry. The surface physics mainly investigate the physical reactions on the surface and interfaces, such as the surface states, adsorbates diffusion, fabrication of nanostructures and so on. [1] Comparatively, the surface chemistry contains more research topics and is widely employed in many technological and practical applications and devices, such as the semiconductor devices, catalysis, electrochemistry and geochemistry.

In the course of surface chemistry, the heterogeneous catalysis is one prototypical research topic since the pioneering definition works by Berzelius in 1836. [3,4] Heterogeneous catalysis is the foundation of the chemistry industry, and provides the basic information and guidelines for the investigation of the chemical reactions on the surface and interface. In addition, heterogeneous catalysis has been widely employed in tremendous areas and devises, and the applications of the heterogeneous catalysis significantly improve the human living conditions and contributes billions of pounds and more jobs to the word economic industry. [5-8] Therefore, it is very important to fully investigate the heterogeneous catalysis and understand the catalytic mechanism of the catalytic reactions.

Usually, the heterogeneous catalysis system is composed of the noble metal nanoclusters (such

as the Pd, Pt and Au nanoclusters) on the transition metal oxides with wide bandgap (such as CeO_2, TiO_2). [9,10] The noble metal nanoclusters act as the catalyst and can dramatically decrease the energy barriers of the chemical reactions without being consumed during the catalytic reactions. Moreover, besides the ability to accelerate the chemical reactions by decreasing the activation energy barriers, the catalyst can also be designed to selectively catalyze the specific chemical reactions, not all the chemical reactions. [1] Figure 1.1 shows one example of the catalyst effect on the activation energy barrier and the selective catalytic reactions. It shows that the catalyst can dramatically decrease the activation energy barrier of the preferred catalytic product of B, and have no effect on the activation energy of the undesired product C. The pronounced and selective catalytic activity of the catalyst in the heterogeneous catalysis provides an efficient way to accelerate the chemical reactions in a controllable manner and can significantly promote the development and improvement of the nanotechnology.

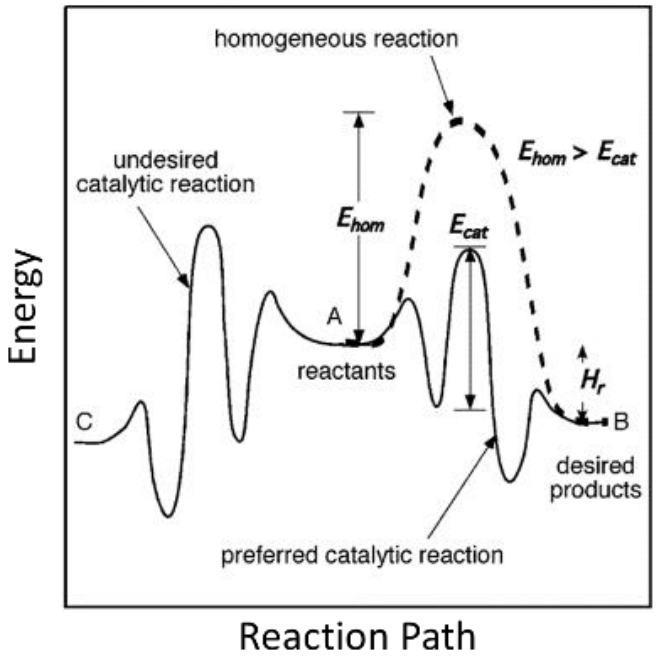

Fig. 1.1 The catalyst effect on the activation energy barrier and the selective catalytic reactions. E_{hom}, energy barrier of the homogeneous reaction. E_{cat}, energy barrier with catalyst. [1]

1.1.2 Au/TiO_2 catalytic system

In the heterogeneous catalysis, the metal oxides are usually employed as the catalytic reaction substrates due to its unique chemical and electronic properties. [11,12] In addition, as the metal oxides can be transformed from the stoichiometric form to semiconductors, and various defects can be formed on the surface or in the interstitial layers, the metal oxides can possess excess electrons on the surface and subsurface as well as the different electronic and optical properties. [13-15]

Titania, TiO_2, compared to other insulators or semiconductors of the metal oxides, has attracted much more research interest in the investigation of the catalysis. Usually, there are two most important crystalline forms of the TiO_2, rutile TiO_2 (bandgap of ~ 3.03 eV) and anatase TiO_2(bandgap of ~ 3.2 eV), in which the rutile TiO_2 is widely used in the photocatalytic reactions due to its interesting photocatalytic properties. [13,16,17] In rutile TiO_2, the TiO_2(110)-(1×1) plane is demonstrated as the most thermal-dynamically stable facet and the best characterized surface, and hence it is the most widely used facet for the catalysis. As the typical catalytic system, Au/TiO_2 is the most widely employed catalytic reactions, due to its high catalytic efficiency and activity. The schematic model of the Au/TiO_2 catalytic system is shown in Figure 1.2.

Tremendous experimental works combined with the theoretical calculations have been performed to investigate the morphological and electric properties of the TiO_2(110) surface, point defects and adsorbates using noncontact atomic force microscopy (nc-AFM), scanning tunnelling microscopy (STM), Kelvin probe force microscopy (KPFM) and X-ray photoelectron spectroscopy (XPS), in order to understand and explain the catalytic mechanism of the Au/TiO_2 catalytic reaction. We review and discuss these past researches about the Au/TiO_2 catalytic reaction in Chapter 4 in details.

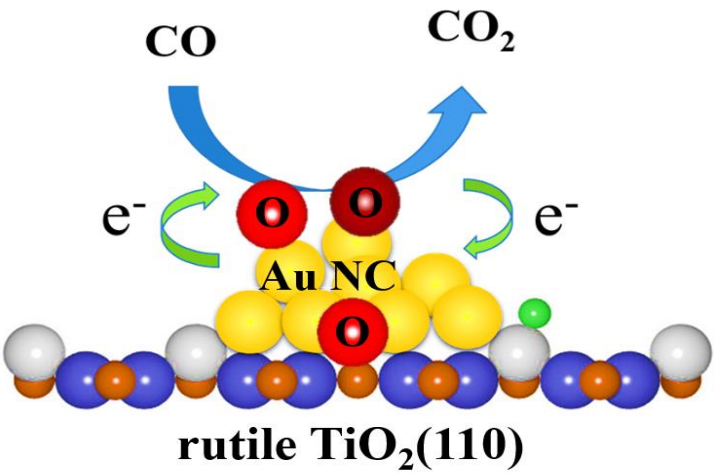

Fig. 1.2 Schematic of Au/TiO_2 catalytic reaction.

However, some critical researches still remain the unexplored research topics in the Au/TiO_2 catalytic system, which are important to understand the catalytic mechanism and deliberately control the catalytic reaction at the ultimate spatial limit, as listed below:

- **Investigation of the subsurface defect on rutile TiO_2 with atomic resolution**

As the electron reservoirs for the catalytic reactions and the preferable adsorption sites of the adsorbates, the morphological arrangement, distribution and electronic properties of the point defects on rutile $TiO_2(110)$ surface play a key role in affecting and controlling the catalytic efficiency of the catalytic reactions. The reversible manipulation of the point defects offers an efficient way to deliberately control and arrange the point defects, hence the distribution of the excess electrons. Though the surface defects have been fully investigated and controllably manipulated, the systematic investigation and deliberate manipulation of the subsurface defects on rutile TiO_2 remain an unexplored research topic at the single atom level.

- **Clarification and manipulation of the charge state of the oxygen adatoms**

The oxygen-rich rutile $TiO_2(110)$ surface has been investigated for more than ten years using

STM at various temperatures, and the adsorption and dissociation behaviours of the oxygen adatoms have been fully discussed and clarified experimentally and theoretically. However, up to now, there is no experimental or theoretical works to clarify and manipulate the charge states of the oxygen adatoms at the atomic scale level, which is important to understand the catalytic mechanism and deliberate control the catalytic reactions.

- **Conductance state of oxygen adatoms**

The conductance state of the oxygen adatoms can exclusively determine its electron transfer ability and the catalytic efficiency in the catalytic reactions, which plays a key role in understanding and explaining the catalytic machinimas. However, few experimental works have investigated the conductance behaviour of the oxygen adatoms up to now.

- **Charge transfer between Au nanoclusters and oxygen adatoms**

The charge transfer plays a critical role in explaining and understanding the catalytic mechanism of the Au/TiO_2 catalytic system. While, at the atomic scale level, no experimental works have been performed to clarify the charge transfer between the Au nanoclusters and oxygen adatoms on the rutile $TiO_2(110)$ surface. In addition, the charge state of the Au nanoclusters on oxidized rutile $TiO_2(110)$ has not been clearly clarified, both experimentally and theoretically.

These research problems listed above are important factors to clarify and understand the catalytic mechanism of the Au/TiO_2 catalytic reaction. Moreover, we believe that, by systematically investigating and manipulating the geometric and electronic properties of the point defects and surface adsorbeate, we can deliberate control the catalytic reactions with the optimized catalytic efficiency. Therefore, our main purpose of this dissertation is to systematically investigate and manipulate the the geometric and electronic properties of the point defects and surface adsorbeate, and finally to clarify the catalytic mechanism and control the catalytic reactions.

1.1.3 Research by noncontact atomic force microscopy

Various analysis techniques are proposed and employed to characterize and investigate the catalytic reactions at the ultimate spatial limit, such as nc-AFM, STM, KPFM, XPS. Among them, the AFM and STM are the most-widely used techniques to investigate the catalytic reactions due to its atomic resolution and high sensitivity. Most importantly, the invention of nc-AFM and STM successfully extends the research scale of the surface science from the micrometer level to atomic level.

STM was firstly invented by Binning and Rohrer at 1982 using the tunneling current effect, [18] which significantly revolutionizes the scientific research about the morphological and electronic properties of the adsorbates at the atomic scale level. While, in the STM measurement, as the tunneling current between the tip and the conductive samples was employed as the detecting signal, the STM can only be applied in the conducting substrates, which seriously limits its application category in insulators and semiconductors. In order to overcome the substrate limitation of the STM, Binning *et al* created the AFM at 1986, [19] which was operated based on the interaction force between the tip and samples to characterize the surface at the atomic scale level. The employment of the interaction force widens the characterization ranges of the target samples from the conductive to nonconductive ones. With the further development of various operation modes of the AFM, the noncontact mode of the AFM (nc-AFM) becomes the most-widely used technique to measure the surface topography, atomic and molecular structures and even the chemical bonds with atomic/subatomic resolution. [20] In addition, in the nc-AFM operation, the force curve as a function of the tip-sample distance $\Delta f(z)$ can be recorded, which can provide precise information of the interaction force on every single atom with high sensitivity. The schematic diagrams of the nc-AFM and STM are shown in Figure 1.3.

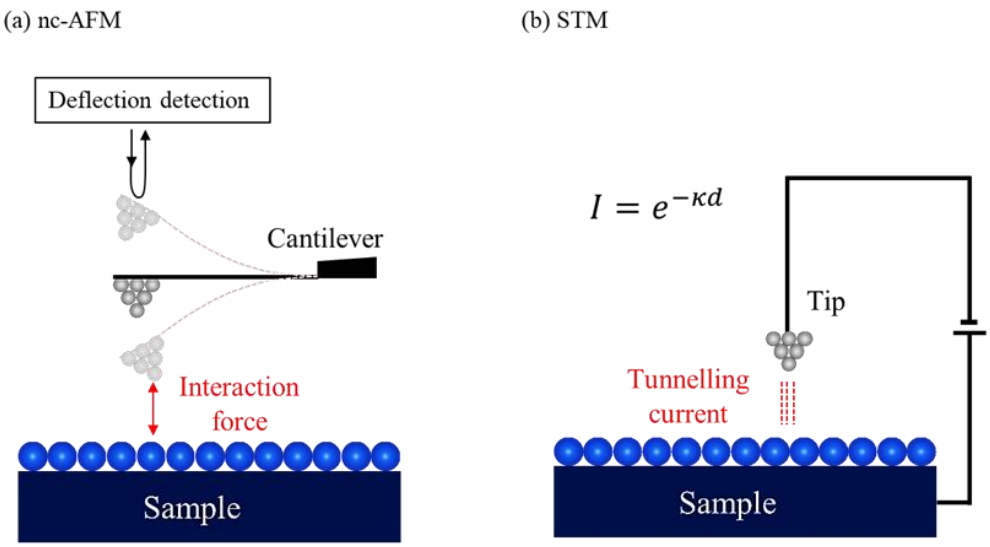

Figure 1.3 Schematic diagrams of the (a) nc-AFM and (b) STM.

In the elementary development stage of the nc-AFM, the nc-AFM was mainly used as an imaging technique to characterize and investigate the surface properties with the atomic scale resolution, and the researchers tried various methods to enhance the images resolution, such as using the ultra-high vacuum (UHV) condition, employing the stiffer cantilever.

Gradually, it is proposed and demonstrated that the nc-AFM cannot only be used as an imaging tool, but also an efficient tool to manipulate the surface atoms with single-atom level precision. [21-23] Depending on the manipulation mode, the atom manipulation based on nc-AFM can be divided into two modes, the lateral manipulation and vertical manipulation. In the lateral manipulation, the distance between the nc-AFM tip apex and the sample was gradually decreased, and the surface atoms can be pulled or pushed by the tip due to the attractive or repulsive interaction force following the predetermined moving direction. After reaching the target site, the tip was gradually raised up and the manipulated atom can precisely locate on the predetermined location with atomic level precision. On the other hand, in the vertical manipulation mode, by approaching and retracting the tip from the sample, the targeted manipulation atom can be picked

up and redeposited to the surface due to the attractive interaction force. The atomic manipulation based on nc-AFM has been widely employed in various substrates, such as the semiconductor and insulting films. [23,24] One example of the lateral and vertical atom manipulation is presented in Figure 1.4. During the atom manipulation process, the threshold force needed to move an atom can be precisely measured as a function of the tip-surface distance. [24] The atom manipulation based on the nc-AFM provides an efficient method to move the target atoms with predetermined movement direction and assembly various nanostructures and nanoscale patterns.

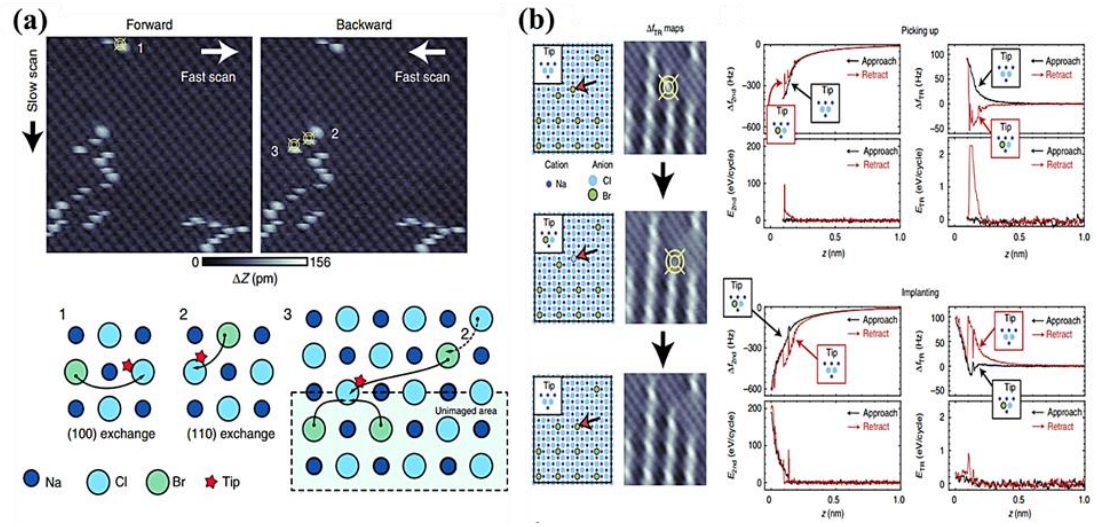

Figure 1.4 Lateral (a) and vertical (b) manipulation of the atoms on insulating film by nc-AFM. [23]

Recently, it is experimentally demonstrated that, the nc-AFM, besides the tremendous capability to build various nanostructures and nanoscale patterns by the direct atom manipulation using the tip, has been gradually employed as an efficient and sensitive tool to measure the charge states of the adsorbates with a single electron sensitivity. [25,26] As mentioned above, the interaction force between the foremost tip apex and the sample was used as the detection signals

to characterize the surface, which can completely avoid the tunneling current effect on the unexpected changes of the charge states of the adsorbed atoms and molecules by STM. In addition, the nc-AFM can be operated in various substrates, including the conductors and insulator samples. As such, the charge states of the adsorbed metal atoms on insulating films have been clearly distinguished, and the neutrally, negatively and positively charged metal atoms were characterized with different image contrast and brightness. [26] It is noticed that the negatively charged atoms always show the brightest contrast due to the strongest attractive force between the tip apex and the charged atom.

In addition to measuring the charge states of the adsorbated atoms or molecules, the nc-AFM has been developed as a tool to deliberately switch different charge states of the adsorbates by various methods. [39-42] Among the various charge states switching strategies, two critical parameters are the most important factors to modify the charge states, the applied bias voltage and the tip-sample distance. For example, the Kelvin probe force spectroscopy (KPFS) was used to switch the charge states of the adsorbates on insulating films with single electron sensitivity. By weeping the bias voltage in positive or negative ranges, the tunneling electrons can be injected to or extracted from the adsorbed atoms with the single electron sensitivity, which can result in the reversible charge states switching. [26] In the charge states witching process, a jump in the frequency shift as a function of the bias voltage $\Delta f(V)$ can be clearly observed, which indicates a successful charge state switching event. Alternatively, the charge states of the adsorbed atoms can also be switched by a voltage pulse with some specific positive or negative values. The voltage pulse was precisely applied on the top of the target atoms with a time duration of several seconds, and a sudden drop of the tunneling current as a function of the time can be observed during the voltage pulse application, which suggests a successful charge states manipulation. In this manipulation process, the charge states switching is always attributed to the inelastic electron

tunneling (IET). [27] On the other hand, the tip-sample distance can act as a tunneling barrier for the tunneling electrons. By gradually approaching the tip to the target atoms, the tunneling electrons can be injected to the adsorbates after reaching the threshold tip-sample distance, and a dip in the frequency shift as a function of the tip-sample distance $\Delta f(z)$ can be clearly observed. [28] Actually, the applied bias voltage and tip-sample distance can influence each other during the injection and extraction of the tunneling electrons, and they offered the efficient way to control and manipulate the charge states of the adsorbates.

Based on the nc-AFM, a large amount of other measurement and analysis techniques have been further developed to collect more physical information about the surface properties. Among them, the KPFM is a prototypical microscopy that can directly measure the work function of the samples with the known work function of the tip, which can record contact potential difference (CPD) between the tip and samples. [29,30] With the definition of local work function, the CPD can be defined as the local CPD (LCPD), and the LCPD images of the sample can be characterized with atomic resolution, providing the potential information of the sample surface and single atoms. KPFM contains several operation modes, including frequency modulation KPFM (FM-KPFM), amplitude modulation KPFM (AM-KPFM) and heterodyne amplitude modulation KPFM (heterodyne AM-KPFM), and usually the FM-KPFM is the most-widely used operation mode due to its high sensitivity and relatively low stray capacitance effect of the cantilever. [30]

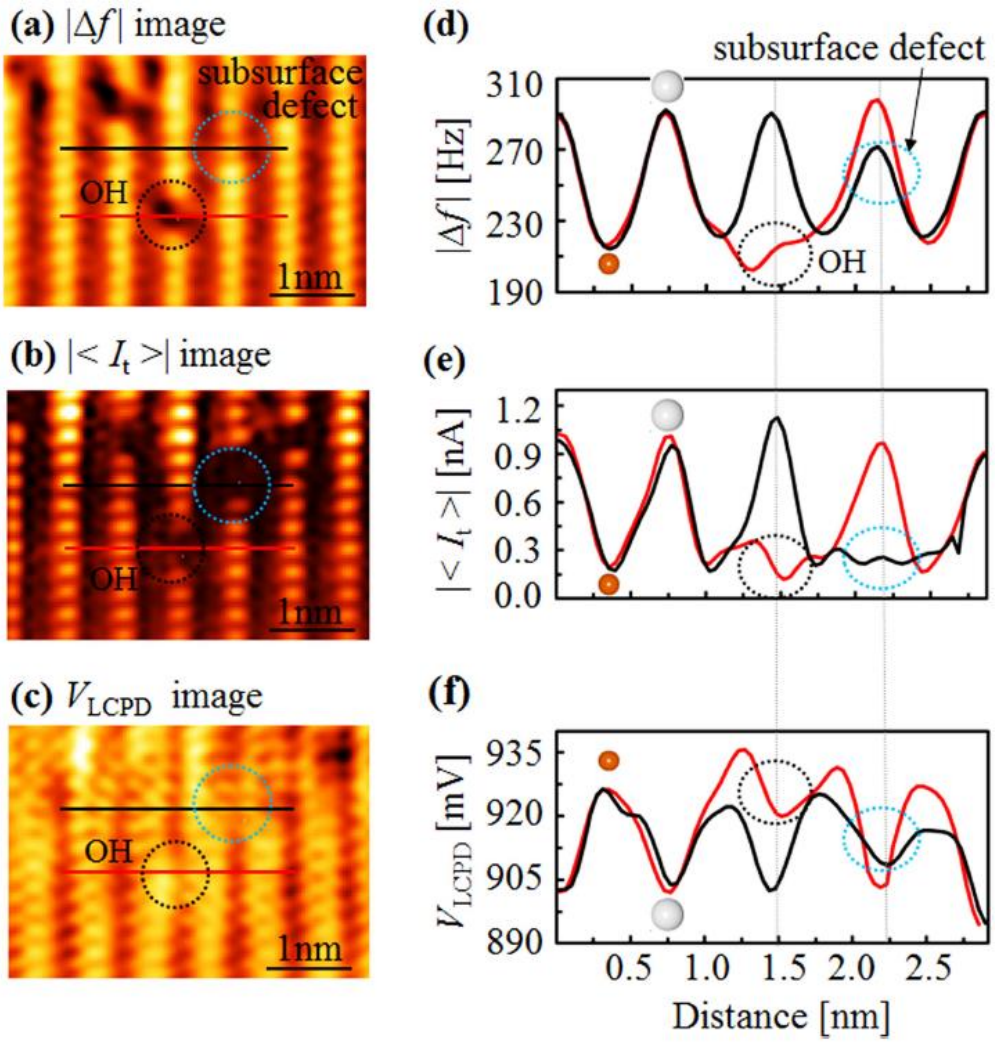

Figure 1.5 Frequency shift, tunneling current and local contact potential difference images of the rutile TiO_2(110) surface simultaneously recorded by KPFM without bias voltage feedback. [32]

Conventionally, the KPFM with bias feedback method was employed to measure the surface potential and topographic images simultaneously, in which an AC bias voltage plus a DC bias voltage are applied in the circuit. The DC bias voltage is always variable to nullify the electrical force originating from the LCPD during measurement. [29] Using such operation mode, the topographical and potential images of the surface can be simultaneously recorded with atomic resolution. With the further development of the KPFM, a new operation mode of the KPFM

without the bias voltage feedback was firstly proposed by the Shigakawa group. [31] In this operation mode, the DC bias voltage keeps a constant value, which completely avoids the phantom force effect in the surface potential measurement. Moreover, the KPFM without bias voltage feedback method offers an efficient way to simultaneously recorded the surface topographic, tunneling current and surface potential images, which offers an effective surface analysis technique to characterize the surface morphological, electronic and potential distribution of the samples. The surface properties of the rutile TiO_2(110) surface using this method has been obtained by our group, as shown in Figure 1.5. [32] In addition, the dual-channel image method of nc-AFM and STM measurement can characterize the surface morphological and electronic properties simultaneously, which provides access to record more physical information of the same scanning area. [33]

The introduction of the nc-AFM significantly revolutionizes the characterization and investigation of the surface science. Compared to STM operation based on the tunneling current between the foremost tip apex and the conductive samples, the interaction force modulation mechanism of the nc-AFM provides an efficient way to characterize the adaorbates and surface properties with atomic resolution on all kinds of materials, including the insulators. Besides the imaging capability with atomic resolution, nc-AFM has been developed as a versatile tool to directly manipulate the adsorbates and surface atoms with atomic precision, to measure and manipulate the charge states of the adsorbates. Based on nc-AFM, the new characterization and analysis methods are developed such as the KPFM, and the multi-channel imaging technique on the basis of nc-AFM can additionally provide more physical information about the surface properties with atomic resolution simultaneously. The nc-AFM opens up an unprecedented research area for the investigation of the surface science and specifically the heterogeneous catalysis.

1.2 Purpose of this research

In this doctoral dissertation, I mainly focused on the investigation and manipulation of the geometric and electronic properties of the reaction components in the Au/TiO_2 catalytic system, including the point defects, oxygen adatoms and Au nanoclusters on rutile TiO_2(110) surface, by using noncontact atomic force microscopy and Kelvin probe force microscopy at 78 K under ultra-high vacuum condition. Such characterization and manipulation of the electronic and geometric properties of the reactants provide an efficient way to explain and understand the catalytic mechanism, and to deliberately control the catalytic reactions in a controllable manner. Firstly, we demonstrate that the subsurface hydrogen on rutile TiO_2(110) can be characterized with atomic resolution by the simultaneous multi imaging method, and the charge distribution of the subsurface hydrogen is experimentally clarified using KPFM for the first time. In addition, we demonstrate that the subsurface defects can be reversibly migrated between the surface and subsurface layers for the first time, which is electrically activated by the voltage pulse with different polarities. Secondly, the charge states of the oxygen adatoms are experimentally clarified for the first time at the atomic scale level, and several manipulation methods are proposed to switch the charge states of oxygen adatoms with single electron sensitivity in a controllable manner. Thirdly, the conductance states of the oxygen adatoms are investigated by using nc-AFM and STM with atomic resolution. We demonstrate that the conductance behavior of the oxygen adatoms exclusively depends on its charge states, and can be reversibly switched between high and low conductance states by controlling its charge states. Lastly, the charge transfer between the Au nanoclusters and oxygen adatoms was experimentally demonstrated using the simultaneous measurement of nc-AFM and KPFM in constant height mode, and the charge state of the Au nanoclusters on oxidized TiO_2(110) surface are experimentally demonstrated. Our work provides a systematic investigation and manipulation of the geometric and electronic properties

of the catalytic reactions components with atomic resolution, and can contribute to the understanding and controlling of the catalytic reactions based on novel metal catalysts on transition metal oxides.

1.3 Thesis outline

The dissertation is organized as follows:

■ In chapter 1, we firstly introduce the importance of the surface science and heterogeneous catalysis, and generally discuss the research progress about the Au/TiO_2 catalytic system. Specifically, the unsolved problems in the Au/TiO_2 catalytic reactions are discussed in details. On the other hand, the importance of the noncontact atomic force microscopy and the related scanning probe microscopies in the characterization of surface morphological and electronic properties, atom and charge manipulation are reviewed. At last, the purpose of this dissertation is briefly discussed.

■ In chapter 2, we talk about the theory of the nc-AFM, STM and KPFM. Firstly, the operation modes of the nc-AFM, interactions force between tip and sample, deconvolution of interaction force from frequency shift and the noise in the system are presented in details. Then, the KPFm and STM are introduced briefly.

■ In chapter 3, we describe the experimental setup of our home-built scanning probe microscopy system in detail. In the first section, the equipment of the low temperature UHV system are explained in details. In the second section, the unit of the nc-AFM, including sample and cantilever stages, the deflection detection system is presented. In addition, the schematic system circuits of FM-AFM, FM-KPFM are presented.

■ In chapter 4, we systematically reviewed and discussed the past researches on rutile TiO2(110) surface, including the clean sample preparation method, the surface and subsurface defects, the

adsorption and dissociation of the oxygen specie and the theoretical works about the charge states of the oxygen molecules and Au nanoclusters. Specifically, we point out the problems in the research progress of the Au/TiO_2(110) catalytic reactions, and we focus on systematically investigating these problems in our dissertation.

■ In chapter 5, we present a systematic characterization and reversible manipulation of the subsurface defect on rutile TiO_2(110) by nc-AFM/STM/KPFM in constant height mode for the first time. The geometric and electronic properties of the subsurface hydrogen on rutile TiO_2(110) are investigated with atomic resolution. In addition, the reversible migration of the subsurface hydrogen between the subsurface and surface layers was demonstrated by controlling the polarities of the voltage pulse, and the migration mechanism is tentatively attributed to the inelastic tunneling electrons and the local electric field.

■ In chapter 6, we successfully distinguish the charge states of the adsorbed oxygen adatoms on rutile TiO_2 surface using the nc-AFM and KPFM measurement. The measurement of short range and LCPD values as a function of tip-sample distance strongly support our assignment of the different charge states of the oxygen adatoms. Moreover, several methods are proposed to switch the charge states of the oxygen adatoms with single electron sensitivity.

■ In chapter 7, the conductance behavior of the single oxygen adatoms is investigated by simultaneous nc-AFM and STM characterization. We find that the conductance states of the oxygen adatoms are exclusively dependent on its charge states, and the high and low conductance states can be reversibly switched by controlling its charge states.

■ In chapter 8, the Au nanoclusters deposited on oxygen-rich rutile TiO_2 surface were characterized by simultaneous nc-AFM and KPFM measurement. The charge state of the Au nanoclusters was clarified as the positively charged, and the LCPD gradually increased as a function of the size of the Au nanoclusters. Moreover, the structural fluxionality of the Au

nanoclusters is experimentally demonstrated.

■ In chapter 9, we summarize the importance of our experimental results in this dissertation, and propose the potential applications of our investigation in the improvement of catalytic reactions based on transition metal oxides. At last, an outlook about the future work is given briefly.

Chapter 2 Principle of scanning probe microscopy (SPM)

2.1 Introduction

In chapter 2, we briefly introduce the principles of several prototypical scanning probe microscopies (SPM), for example, the noncontact atomic force microscopy (nc-AFM), scanning tunneling microscopy (STM) and Kelvin probe force microscopy (KPFM). Firstly, we discuss the theory of nc-AFM, including the nc-AFM operation modes, tip-sample interaction force, deconvolution of force from frequency shift, stability of the measurement system and the noise in nc-AFM. Then, a brief introduction of the STM is given with comparison between static STM and dynamic STM. Thirdly, the KPFM principle is briefly introduced with explanation of contact potential difference, and two KPFM measurement methods, namely, with/without bias voltage feedback, are followed. Lastly, a brief conclusion is given in the final part of this chapter.

2.2 Noncontact atomic force microscopy (nc-AFM)

The AFM was invented in 1986 by G. Binning after he firstly inventing the STM in 1981. [1,2] The most important advantage of the AFM is that, unlike the STM that requires the conductive substrate and the tunneling current, [1] the AFM can be operated on insulators, semiconductors and conductors, and the interaction force F_{ts} between the tip and the samples is used as the imaging signal. Depending on the range and strength of the interaction force, the F_{ts} can usually be divided into long-range force, such as van der Waals, electrostatic and magnetic forces, and the short-range force, such as chemical force. [2]

2.2.1 Operation modes

Generally, there are three operation modes of the AFM measurements, namely, the contact mode, the tapping mode and the noncontact mode. [3-5] Among them, the noncontact mode is the most widely employed measurement mode thus far.

- **Contact mode**

In the contact method, the cantilever is brought into contact with the sample surface, and the surface morphology can be characterized in the repulsive force range. Since the probe contacts the sample, the soft cantilever is usually used in the contact mode. The spring constant of the cantilever k determines the detection sensitivity, which varies from 0.01 N/m to 5 N/m. Because of the repulsive force between the tip and sample, the mechanical instability during the scanning always exists. In addition, it is difficult to prevent destruction of the probe tip and the sample surface.

- **Tapping mode**

In tapping mode, the cantilever can periodically contact the sample surface, and the sample morphology can be measured from the change in the vibration amplitude of the cantilever due to the repulsive interaction between the tip and sample. Although the tip is brought into contact with the sample surface for a short time during scanning, it is also likely to damage the tip and the sample surface.

- **Noncontact mode**

In noncontact mode, the measurement is performed at relatively small tip-sample distance, and the tip does not touch the sample surface during scanning. The cantilever is usually oscillated at its resonance frequency f_0, [4] and the characterization is usually performed in the attractive region of the interaction force. In addition, it is possible to prevent destructing the tip of the probe and the sample surface during scanning with high resolution. Usually, the noncontact mode can be

operated with the amplitude modulation (AM) and frequency modulation (FM) methods, as schematically shown in Figure 2.1. [6]

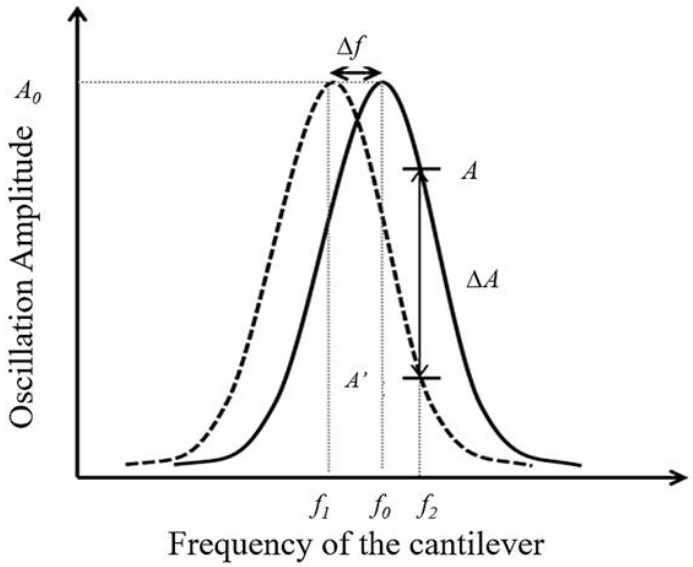

Figure 2.1 Scheme of AM- and FM-AFM measurement methods.

In the AM-AFM method, the cantilever is oscillated at the free resonance frequency f_0. When the tip approaches the sample surface, the attractive force is applied. As a result, the resonance frequency of the cantilever changes from f_0 to f_1 as shown in Figure 2.1, which results in the oscallation amplitude of the cantilever changing from A to A'. In the AM-AFM method, the ΔA is regarded as the detection signal. The minimum detection sensitivity of the AM method can be expressed by equation (2.2.1). [7]

$$(\Delta f)_{AM} = \delta(f - f_0)_{AM} = \sqrt{\frac{27kk_BTB}{f_0 Q\langle Z_{osc}^2\rangle}} \qquad (2.2.1)$$

Where k is the spring constant of the cantilever, k_BT is the thermal energy at temperature T, B is the detection band, f_0 is the cantilever resonance frequency, Q is the Q factor of the cantilever, and $\langle Z_{osc}^2\rangle$ is the mean square value of the vibration amplitude of the cantilever. (The transient response of amplitude is shown in the following equation (2.2.2). [8]

$$\tau_{AM} \cong \frac{2Q}{f_0} \qquad (2.2.2)$$

Usually the Q value is very high under an ultra-high vacuum condition, resulting in the long response time in the AM method. Therefore, the amplitude modulation method is not suitable for the measurement in the ultra-high vacuum condition.

In the FM method, the cantilever is oscillated at a resonance frequency f_0 while keeping the amplitude A constant. With the interaction force between the tip and sample, the resonant frequency of the cantilever shifts from f_0 to f_1, and the Δf is regarded as the detection signal. The minimum detection sensitivity of the frequency modulation method can be expressed by equation (2.2.3). [8]

$$\delta(\Delta f)_{FM} = \sqrt{\frac{4kk_BTB}{f_0 Q\langle Z_{osc}^2\rangle}} \tag{2.2.3}$$

Equation (2.2.4) shows the transient response of the amplitude. [9]

$$\tau_{FM} \cong \frac{1}{f_0} \tag{2.2.4}$$

The transient response is independent of the Q of the cantilever. Based on the above results, we employ the FM-AFM detection method in our experiment, and the corresponding schematic circuit is shown in Figure 2.2.

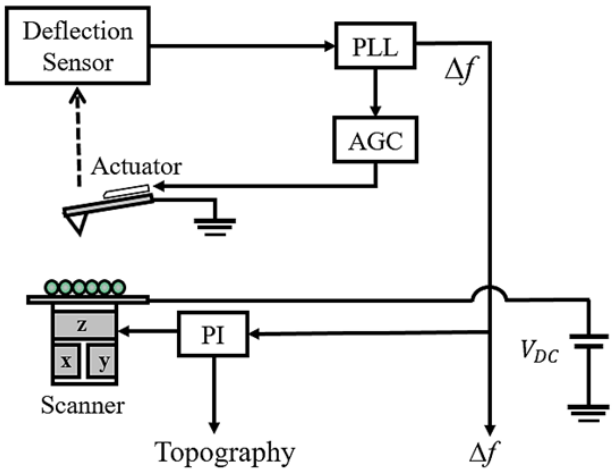

Figure 2.2 Schematic of the detection methods for FM-AFM.

2.2.2 Tip-sample interaction force

In AFM measurement, the interaction forces F_{ts} between a tip and the sample surface is used as the detection signal to characterize the surface structure. Usually, depending on the force range and strength, the interaction forces F_{ts} can be divided into long-range force area (up to 100 nm) and short-range force (within 1 nm). The long-range force includes long-range van der Waals forces, electrostatic forces, and magnetic forces, and the short-range forces are chemical

force and short-range electrostatic force between the tip apex and sample surface. In our research, the van der Waals forces, the electrostatic forces, and the chemical forces are mainly discussed, as shown in Figure 2.3.

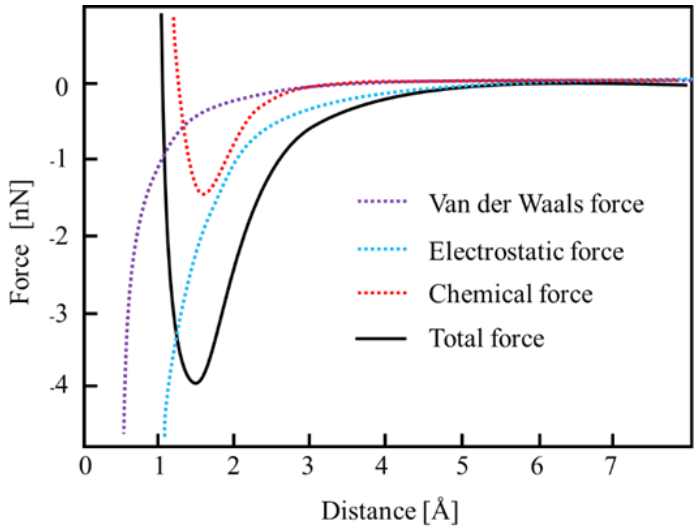

Figure 2.3 Force as a function of the distance between the tip front atom and substrate.

- **van der Waals force**

The van der Waals force is usually based on the Coulomb interaction of the atoms and caused by electric dipole moment fluctuations of atoms and their corresponding mutual polarization. Usually, the van der Waals force plays a key role in the AFM topographic measurement at the nanometer scale.

Here a common sphere-plane model is employed to represent the AFM probe and the sample surface, and the force dependence is [10]

$$F_{vdW} = -\frac{2A_H R^3}{3z^2(z+2R)^2} \tag{2.2.5}$$

where A_H is the Hamaker constant, z is the separation between the sphere and the half-space surface, and R is the sphere radius of the tip apex. Assuming $z < R$, this relation is reduced to:

$$F_{vdW} \cong -\frac{A_H R}{6z^2} \tag{2.2.6}$$

- **Electrostatic force**

Electrostatic force become an important component when there an electrostatic potential difference between the tip apex and sample surface. The electrostatic force can be expressed as:

$$F_{\mathrm{es}} = \frac{\mathrm{d}E_{\mathrm{es}}}{\mathrm{d}z} = -\frac{1}{2}\frac{\mathrm{d}C}{\mathrm{d}z} f(z). \qquad (2.2.7)$$

where the C is capacitance between tip and sample surface, z is the tip-sample distance, and the E_{es} is the electrostatic energy. The electrostatic forces between a sphere and an infinite plane was firstly calculated by Hudlet, [11,12] and can be defined as:

$$F_{es} = \pi\varepsilon_0 V^2\left[\frac{R^2(1-\cos\alpha)}{z[z+R(1-\cos\alpha)]} + k^2\left(\ln\frac{z+R(1-\cos\alpha)}{h}\right) - 1 + \frac{R\sin^2\alpha/\cos\alpha}{z+R(1-\cos\alpha)}\right], \qquad (2.2.8)$$

where $k^2 = \frac{1}{\left[\ln\tan(\pi/2-\alpha)/2\right]^2}$. Assuming the tip apex is really sharp and α is small enough, then the equation can be simplified as:

$$F_{es} = \pi\varepsilon_0 V^2\left[\frac{R^2}{z(z+R)} + k^2\left(\ln\frac{z+R}{h}\right) - 1 + \frac{R\cos\alpha}{z+R}\right]. \qquad (2.2.9)$$

If $z << R$, it suggests an even simpler equation:

$$F_{es} \cong -\frac{\pi\varepsilon_0 R}{z} V^2 \qquad (2.2.10)$$

- **Chemical force**

The chemical force belongs to the short range force, and is formed when two or more atoms come together to form a molecule or chemical substance. In AFM, the chemical force is from the chemical interaction between the foremost tip apex atoms and the sample surface species. Usually, the chemical force plays a key role for the AFM images with the atomic or subatomic resolution. In practice, the chemical force is simplified to predict the bonding strength and polarity. The chemical bonding energy is described by the *Morse* potential formulas, [13] which is given as following:

$$U_{Morse} = -E_{bond}(2e^{-(z-\sigma)/\lambda} - e^{-2k(z-\sigma)/\lambda}) \qquad (2.2.11)$$

here the E_{bond}, σ, λ and z are bonding energy, equilibrium distance, decay length and the distance between atoms, respectively. The Morse potential is induced by approximation of the covalent bonding

interaction. By differentiating U_{Morse} by the decay length, the chemical force is obtained as

$$F_{chem} = -\frac{2E_{bond}}{\lambda}(e^{-2(z-\sigma)/\lambda} - e^{-k(z-\sigma)/\lambda}) \quad (2.2.12)$$

- **The minimum detectable force**

The minimum detectable force is given by:

$$\delta F_{\text{ts min}} = \sqrt{2\pi}k\frac{\delta\Delta f_{\text{min}}}{f_0}\frac{A^{3/2}}{\lambda^{1/2}} \quad (2.2.13)$$

Where k, f_0, A and λ are the spring constant, resonance frequency of the cantilever, tip oscillation amplitude and the tip-sample force decay length. The minimum detectable force gradient $k_{\text{ts min}}$ can be represented as below: [25]

$$k_{ts\,\text{min}} \approx 2k\frac{\delta\Delta f_{\text{min}}}{f_0} \quad (2.2.14)$$

where $\delta\Delta f_{\text{min}}$ is the minimum detectable frequency shift. In this way, we can conclude that the minimum detectable force and the force gradient are strictly dependent on the minimum detectable frequency shift.

- **Relationship between frequency shift and oscillation amplitude of the cantilever**

The relationship between the frequency shift Δf and the oscillation amplitude A of the cantilever can be repressed as below: [11]

$$\Delta f = \frac{f_0}{\pi k A^2}\int_{-A}^{A} k_{\text{ts}}(z-q')\sqrt{A^2 - q'^2}\,dq' \quad (2.2.15)$$

where the f_0, k, A are the resonance frequency of the cantilever, spring constant and oscillation amplitude of the cantilever. k_{ts} is the tip-sample force gradient and q· is deflection of the cantilever. In the equation (2.2.15), the integrated part represents the weighted average of k_{ts} in one oscillation cycle with the oscillation amplitude of A. The weight function w (q', A) is a semicircle with radius A divided

by the area of the semicircle $r = \pi A^2/2$, as shown in Figure 2.4.

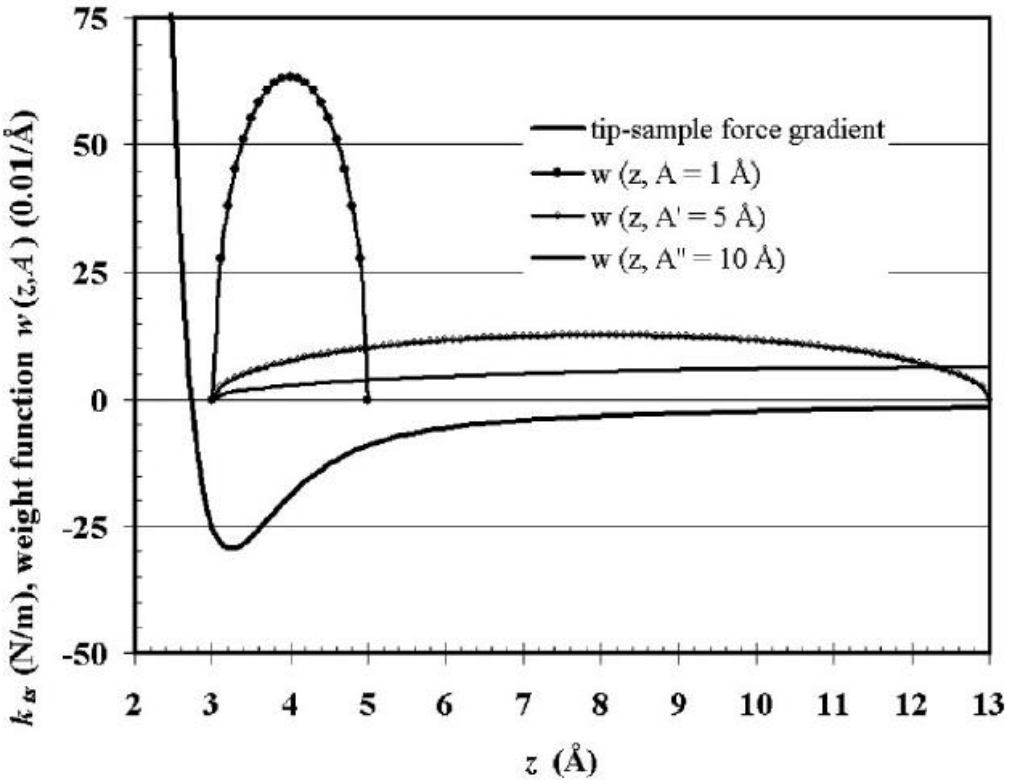

Fig. 2.4 Calculation of the weight function as a function of tip-sample distance with different oscillation amplitude. [11]

We can see that, with the relatively small oscillation amplitude, the weight function is with small radius, and the interaction force between the tip and sample is mainly in the short range force range. The radius of the weight function increases with the increased oscillation amplitude, which results in the tip-sample interaction force mainly in the long range force range. Usually the shot range force is necessary for the high resolution imaging. Therefore, the small oscillation amplitude is advantageous and preferable to obtain the AFM images with high resolution.

2.2.3 Deconvolution of interaction force from frequency shift

- **Relationship between frequency shift and interaction force**

As we have discussed above, the frequency modulation AFM (FM-AFM) method is used in this research. In FM-AFM, the cantilever is oscillated at its resonant frequency shift with a constant oscillation amplitude *A*, as shown in Figure 2.4.

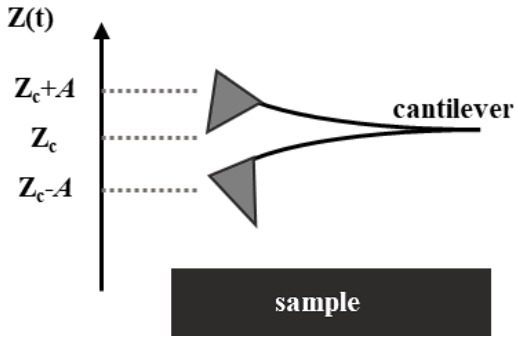

Fig. 2.5 Schematic diagram of the cantilever oscillation. Z_c is the center of cantilever, and A is the oscillating amplitude of the cantilever.

Here, we will investigate the relationship between the frequency shift (Δf) and the interaction force F_{ts} between the tip and the sample surface. The movement of the cantilever can be expressed as shown in Equation (2.2.16).

$$m\frac{d^2z}{dt^2}+\frac{m\omega_0}{Q}\frac{dz}{dt}+kz(t)=kA_{exc}cos\omega t+F_{ts}[z_c+z(t)] \tag{2.2.16}$$

Where m is the effective mass of the cantilever, Q is the Q value of the cantilever, ω_0 is the resonance frequency of the cantilever, k is the spring constant, Z_c is the initial value of the cantilever. Substituting $m = k/{\omega_0}^2$

$$\frac{d^2z}{dt^2}+\frac{\omega_0}{Q}\frac{dz}{dt}+{\omega_0}^2z(t)={\omega_0}^2A_{exc}cos\omega t+\frac{{\omega_0}^2}{k}F_{ts}[z_c+z(t)] \tag{2.2.17}$$

Here z(t) can be expressed by a cosine function.

$$z(t) = A\cos(\omega t - \phi) \tag{2.2.18}$$

Substituting (2.218) into (2.2.17)

$$\frac{\omega_0^2 - \omega^2}{\omega_0^2} A\cos(\omega t - \phi) - \frac{\omega A}{\omega_0 Q}\sin(\omega t - \phi)$$

$$= A_{\text{exc}}\cos\omega t + \frac{1}{k}F_{\text{ts}}[z_{\text{c}} + A\cos(\omega t - \phi)] \tag{2.2.19}$$

In order to use the orthogonality of the trigonometric function, multiplying by cos(ωt-ϕ) and integrating with one period T = 2π/ω gives (2.2.20).

$$\frac{\omega_0^2 - \omega^2}{\omega_0^2} A \int_{\frac{\phi}{\omega}}^{\frac{2\pi+\phi}{\omega}} \cos^2(\omega t - \phi)dt - \frac{\omega A}{\omega_0 Q}\int_{\frac{\phi}{\omega}}^{\frac{2\pi+\phi}{\omega}} \sin(\omega t - \phi)\cos(\omega t - \phi)dt$$

$$= A_{\text{exc}}\int_{\frac{\phi}{\omega}}^{\frac{2\pi+\phi}{\omega}} \cos\omega t\cos(\omega t - \phi)dt \tag{2.2.20}$$

$$+\frac{1}{k}\int_{\frac{\phi}{\omega}}^{\frac{2\pi+\phi}{\omega}} F_{\text{ts}}[z_{\text{c}} + A\cos(\omega t - \phi)]\cos(\omega t - \phi)dt$$

when this is replaced and integrated with $\theta = \omega t - \phi$ and solved for cosϕ, equation (2.2.21) is established.

$$\cos\phi = \frac{\omega_0^2 - \omega^2}{\omega_0^2}\frac{A}{A_{\text{exc}}} - \frac{1}{\pi k A_{\text{exc}}}\int_0^{2\pi} F_{\text{ts}}[z_{\text{c}} + A\cos\theta]\cos\theta d\theta \tag{2.2.21}$$

Similarly, multiplying equation (2.2.18) by sin($\omega t - \phi$) in order to use the orthogonality of trigonometric functions, and similarly solving this for sinϕ by substituting and integrating with $\theta = \omega t - \phi$ and equation (2.2.22) is established.

$$\sin\phi = -\frac{\omega}{\omega_0 Q}\frac{A}{A_{\text{exc}}} - \frac{1}{\pi k A_{\text{exc}}}\int_0^{2\pi} F_{\text{ts}}[z_{\text{c}} + A\cos\theta]\sin\theta d\theta \tag{2.2.22}$$

if $F_{\text{ts}} = 0$ is substituted, $\sin\phi, \cos\phi$ will be expressed by equations (2.2.23) and (2.2.24), respectively.

$$\cos\phi = \frac{\omega_0^2 - \omega^2}{\omega_0^2}\frac{A}{A_{\text{exc}}} \tag{2.2.23}$$

$$\sin\phi = -\frac{\omega}{Q\omega_0}\frac{A}{A_{\text{exc}}} \tag{2.2.24}$$

Substituting equation (2.2.23) and equation (2.2.24) into $\cos^2\phi + \sin^2\phi = 1$ and solving with ω as f, amplitude A and phase lag ϕ are respectively expressed by equation (2.2.25) and the formula (2.2.26).

$$A = \frac{A_{\mathrm{exc}} Q}{\sqrt{\left(1 - \frac{f^2}{f_0^2}\right)^2 Q^2 + \frac{f^2}{f_0^2}}} \tag{2.2.25}$$

$$\tan\phi = -\frac{f_0 f}{(f_0^2 - f^2)Q} \tag{2.2.26}$$

When $f = f_0$, Equation (2.2.27) and Equation (2.2.28) can be derived from Equation (2.2.25) and Equation (2.2.26).

$$A = A_{\mathrm{exc}} Q \tag{2.2.27}$$

$$\phi = -\frac{\pi}{2} \tag{2.2.28}$$

Equations (2.2.27) and (2.2.28) show that the response signal of the cantilever is delayed by 90 ° when the cantilever is excited at the resonance frequency. When $F_{\mathrm{ts}} \neq 0$. At this time, equation (2.2.29) can be derived from equation (2.2.21).

$$\frac{\omega_0^2 - \omega^2}{\omega_0^2} = \frac{A_{\mathrm{ext}}}{A}\cos\phi + \frac{1}{\pi k A}\int_0^{2\pi} F_{\mathrm{ts}}[z_{\mathrm{c}} + A\cos\theta]\cos\theta d\theta \tag{2.2.29}$$

Here the equation (2.2.30) is employed.

$$\frac{(\omega_0^2 - \omega^2)}{\omega_0^2} \approx -2\frac{\Delta\omega}{\omega_0} = -2\frac{\Delta f}{f_0} \tag{2.2.30}$$

Therefore, the frequency shift Δf is expressed by equation (2.2.31) from equations (2.2.29) and (2.2.30).

$$\Delta f = -\frac{f_0 A_{\mathrm{exc}}}{2A}\cos\phi - \frac{f_0}{2\pi k A}\int_0^{2\pi} F_{\mathrm{ts}}[z_{\mathrm{c}} + A\cos\theta]\cos\theta d\theta \tag{2.2.31}$$

The cantilever is now excited at the resonant frequency, so the phase is 90 degrees behind. Therefore, the first term of equation (2.2.31) is 0, so equation (2.2.32) can be derived.

$$\Delta f = -\frac{f_0}{2\pi k A}\int_0^{2\pi} F_{\mathrm{ts}}[z_{\mathrm{c}} + A\cos\theta]\cos\theta d\theta \tag{2.2.32}$$

Also, if equation (2.2.32) is replaced with $\mathrm{u} = \cos\theta$ and $z_{\mathrm{c}} = z + A$, equation (2.2.33) is obtained.

$$\Delta f = -\frac{f_0}{\pi k A}\int_{-1}^{1} F_{\mathrm{ts}}[z + A(1+u)]\frac{u}{\sqrt{1-u^2}} du \tag{2.2.33}$$

Now the relational expression between the frequency shift and the interaction force was derived.

- **Conversion from frequency shift to interaction force**

The interaction force acting between the probe and sample surface can be obtained in equation

(2.2.33) now. The equation for small and large amplitude approximations are shown in Equation (2.2.34) and (2.2.35). [8,9]

$$F_{small}(z) = 2k\int_{z}^{\infty}\Omega(t)dt \tag{2.2.34}$$

$$F_{large}(z) = -\sqrt{2}kA^{\frac{3}{2}}\int_{z}^{\infty}\frac{1}{\sqrt{(t-z)}}\frac{d\Omega(t)}{dz}dt \tag{2.2.35}$$

where $\Delta f/f_0 = \Omega(z)$. In this section, we show how to solve for F_{ts} in a way that has little error regardless of the distance dependence of the amplitude and interaction force considered by Sader and Javis.[14]

First, the interaction force $F_{ts}(z)$ acting between the tip and samples is expressed by the following formula (2.2.36) using the inverse Laplace transform $F_{ts}(z)$.

$$F_{ts}(z) = \int_{0}^{\infty}A(\lambda)\exp(-\lambda z)\,d\lambda \tag{2.2.36}$$

Substituting this into equation (2.2.33) yields equation (2.2.37).

$$\Delta f = -\frac{f_0}{kA}\int_{-1}^{1}\int_{0}^{\infty}A(\lambda)\exp(-\lambda z - \lambda A(1+u))\frac{u}{\sqrt{1-u^2}}dz\,du \tag{2.2.37}$$

When the integral is exchanged, it becomes like (2.2.38)

$$\Delta f = -\frac{f_0}{kA}\int_{0}^{\infty}\int_{-1}^{1}A(\lambda)\exp(-\lambda z - \lambda A(1+u))\frac{u}{\sqrt{1-u^2}}du\,dz \tag{2.2.38}$$

Here we use the modified Bessel function, equation (2.2.39)

$$I_n(z) = \frac{1}{\pi}\int_{0}^{\pi}e^{z\cos\theta}\cos(n\theta)\,d\theta \tag{2.2.39}$$

When n = 1, it becomes like (2.2.40)

$$I_1(z) = \frac{1}{\pi}\int_{0}^{\pi}e^{z\cos\theta}\cos\theta\,d\theta \tag{2.2.40}$$

If equation (2.2.40) is transformed using $\mathrm{u} = \cos\theta$ and $I_1(z) = -I_1(-z)$, equation (2.2.41) is obtained.

$$I_1(z) = -\frac{1}{\pi}\int_{-1}^{1}e^{-z\mathrm{u}}\frac{u}{\sqrt{1-u^2}}du \tag{2.2.41}$$

Therefore, equation (2.2.38) defines $(x) = I_1(x)e^{-x}$ and $T(x)$

$$\frac{\Delta f}{f_0} = \frac{1}{kA}\int_0^\infty A(\lambda)T(\lambda A)e^{-\lambda z}d\lambda \tag{2.2.42}$$

can be written. Also, if both sides are inverse Laplace transformed and equation (2.2.43) is used

$$\mathcal{L}[Y(\lambda)] = \int_0^\infty Y(\lambda)\exp(-\lambda z)\,dz \tag{2.2.43}$$

Equation (2.2.41) is expressed by Equation (2.2.44)

$$A(\lambda) = \frac{kA}{T(\lambda A)}\mathcal{L}^{-1}\left[\frac{\Delta f}{f_0}\right] \tag{2.2.44}$$

Here, the following equation (2.2.45) holds:

$$F_{ts}(z) = \mathcal{L}[A(\lambda)] \tag{2.2.45}$$

Substituting equation (2.2.44) into equation (2.2.45) gives equation (2.2.46)

$$F_{ts}(z) = \mathcal{L}\left[\frac{kA}{T(\lambda A)}\mathcal{L}^{-1}\left[\frac{\Delta f}{f_0}\right]\right] \tag{2.2.46}$$

Here, using the approximate expression (2.2.47) of $T(x)$

$$T(x) = \frac{x}{2}\left(1 + \frac{1}{8}x^{\frac{1}{2}} + \sqrt{\frac{\pi}{2}}x^{\frac{3}{2}}\right)^{-1} \tag{2.2.47}$$

Expression (2.2.46) becomes like Expression (2.2.48).

$$F_{ts}(z) = 2k\left\{\mathcal{L}\left[\lambda^{-1}\mathcal{L}^{-1}\left[\frac{\Delta f}{f_0}\right]\right] + \frac{1}{8}A^{\frac{1}{2}}\mathcal{L}\left[\lambda^{-\frac{1}{2}}\mathcal{L}^{-1}\left[\frac{\Delta f}{f_0}\right]\right] + \sqrt{\frac{\pi}{2}}A^{\frac{3}{2}}\mathcal{L}\left[\lambda^{\frac{1}{2}}\mathcal{L}^{-1}\left[\frac{\Delta f}{f_0}\right]\right]\right\} \tag{2.2.48}$$

Note that $\mathcal{L}^{-1}[\Delta f/f_0]$ is a function of λ, and the following equations (2.2.49), (2.2.50), (2.2.51), using formula (2.2.52)

$$\mathcal{L}[\lambda^{-\alpha}Y(\lambda)] = I^{\alpha}\mathcal{L}[Y(\lambda)] \tag{2.2.49}$$

$$\mathcal{L}[\lambda^{\alpha}Y(\lambda)] = D^{\alpha}\mathcal{L}[Y(\lambda)] \tag{2.2.50}$$

$$I^{\alpha}\varphi(\lambda) = \frac{1}{\Gamma(\alpha)}\int_\lambda^\infty Y(\lambda)\frac{\varphi(t)}{(\mathrm{t}-\lambda)^{1-\alpha}}\,dt \tag{2.2.51}$$

$$D^{\alpha}\varphi(\lambda) = \frac{(-1)^n}{\Gamma(n-\alpha)}\frac{d^n}{d\lambda^n}\int_\lambda^\infty \frac{\varphi(t)}{(\mathrm{t}-\lambda)^{\alpha-n+1}}\,dt \tag{2.2.52}$$

If we put $\Delta f/f_0 = \Omega(z)$, Equation (2.2.48) becomes Equation (2.2.53).

$$F_{ts}(z) = 2k\int_z^\infty \left[\left(1 + \frac{A^{\frac{1}{2}}}{8\sqrt{\pi(t-z)}}\right)\Omega(t) - \frac{A^{\frac{3}{2}}}{\sqrt{2(t-z)}}\frac{d\Omega(t)}{dz}\right]dt \tag{2.2.53}$$

The interaction force acting between the probe samples can be estimated from the frequency shift

value observed from the equation (2.2.53). The fact that the interaction force acting between the probe samples can be estimated from the observed frequency shift value is a major feature of FM-AFM. Equation (2.2.53) is a better approximation than Equations (2.2.34) and (2.2.35). As can be seen by comparing with the equations (2.2.34) and (2.2.35), it can be seen that the small amplitude approximation is the contribution of the first term of the equation and the large amplitude approximation is the contribution of the third term. This corresponds to the first and third terms in the approximate $T(x)$ of the modified Bessel function. Here, $U_{ts}(z)$ is set as shown in equation (2.2.54).

$$U_{ts}(z) = 2k\int_{z}^{\infty}\Omega(t)\left((t-z)+\frac{A^{\frac{1}{2}}}{4}\sqrt{\frac{t-z}{\pi}}+\frac{A^{\frac{3}{2}}}{\sqrt{2(t-z)}}\right)dt \tag{2.2.54}$$

Because equation (2.2.54) satisfies equation (2.2.55)

$$F_{ts}(z) = -\frac{dU_{ts}(z)}{dz} \tag{2.2.55}$$

$U_{ts}(z)$ represents the potential.

2.2.4 Noise in the AFM

In FM-AFM measurement, the prerequisite is that the mechanical vibration between the tip and sample should be smaller than the atomic corrugation of the sample. In general, several kinds of noise in the measurement system should be considered, including the frequency noise, deflection detection noise, oscillator noise and thermal frequency drifts noise.

- **Frequency noise**

The vertical noise in FM-AFM is given by the ratio between the noise in the imaging signal and the slope of the imaging signal with respect to *z* [4]:

$$\delta z_f = \frac{\delta\Delta f}{\left|\partial f / \partial d\right|}, \tag{2.2.56}$$

the thermodynamic lower limit of the frequency noise

$$\delta f_{thermal} = \delta(\Delta f)_{thermal} = \sqrt{\frac{k_B T B f_0}{k A_0^{\,2} \pi Q_0}} \qquad (2.2.57)$$

Thermal noise is constant with respect to f_{mod}:

$$n_{k_{ts\,th}} = \sqrt{\frac{4 k k_B T}{A_0^{\,2} \pi Q f_0}} \qquad (2.2.58)$$

where k_B is the Boltzmann constant, T the absolute temperature, B the detection bandwidth and Q the quality factor of the cantilever. The detection bandwidth B determines the imaging speed.

- **Deflection detection noise**

The oscillation frequency of the cantilever varies very little around the resonance frequency f_0. A constant deflection detector noise density n_q was assumed to denote the precision at which the deflection of the cantilever could be measured. [15, 16] This uncertainty in the deflection measurement also leads to frequency noise, as given by

$$\frac{\delta f_{\mathrm{det}}}{f_0} = \sqrt{\frac{2}{3}} \frac{n_q B^{3/2}}{A f_0}, \qquad (2.2.59)$$

and the deflection detector noise on the force gradient is given by

$$\delta k_{\mathrm{ts\,det}} = \sqrt{\frac{8}{3}} \frac{k n_q}{f_0} \frac{B^{3/2}}{A}. \qquad (2.2.60)$$

- **Oscillator noise**

Recently, a new contribution to frequency noise in FM-KPFM has been discovered, which arises in particular in a low-Q environments. [17] The origin of this noise can be considered as a driving of the cantilever off resonance because the amplitude feedback is fed with a noisy input signal (due to a finite n_q). This noise contribution is proportional to n_q and inversely proportional to Q:

$$\frac{\delta f_{osc}}{f_0} = \frac{n_q B^{1/2}}{\sqrt{2} A Q}, \qquad (2.2.61)$$

with $\delta k_{ts} = 2k\frac{\delta f}{f_0}$, it is given

$$\delta k_{ts\,\mathrm{osc}} = \sqrt{2}\frac{kn_q}{Q}\frac{B^{1/2}}{A}, \tag{2.2.62}$$

Similar to thermal noise, oscillator noise is proportional to the square root of the detection bandwidth B and inversely proportional to amplitude.

Oscillator noise is also constant with f_{mod}:

$$n_{k_{ts\,\mathrm{osc}}} = \sqrt{2}\frac{kn_q}{AQ}. \tag{2.2.63}$$

- **Thermal frequency drifts noise**

An eigenfrequency drift can be induced by the temperature variations. [18]

$$\frac{\delta f_{sensor}}{f_0} = \sqrt{\frac{k_B TB}{kA^2\pi f_0 Q}} \tag{2.2.64}$$

The magnitude of this noise component depends on the drift rate of the frequency r and the measurement period τ. The effect of this noise on the force gradient measurement is given:

$$n_{k_{ts\,\mathrm{drift}}}(f_{\mathrm{mod}}) = \frac{2kr\sqrt{\tau}}{f_0\pi f_{\mathrm{mod}}}. \tag{2.2.65}$$

Because the frequency drift rate is proportional to f_0, the force gradient noise due to thermal drift is proportional to the stiffness of the sensor k.

All noise sources contribute to the experimental noise graphs. The absolute force gradient noise can be transformed in a density representation by

$$n_{k_{ts\,\mathrm{drift}}}(f_{\mathrm{mod}}) = \sqrt{\left.\frac{\partial \delta k^2_{ts}}{\partial B}\right|_{B=f_{\mathrm{mod}}}}, \tag{2.2.66}$$

The total noise of the force gradient measurement is given by

$$\delta k_{ts} = \sqrt{\int_{1/\tau}^{B} n^2_{k_{ts}}(f_{\mathrm{mod}})df_{\mathrm{mod}}}, \tag{2.2.67}$$

$$n^2{}_{k_{ts}}(f_{\mathrm{mod}}) = n^2{}_{k_{ts\,\mathrm{det}}}(f_{\mathrm{mod}}) + n^2{}_{k_{ts\,\mathrm{th}}} + n^2{}_{k_{ts\,\mathrm{osc}}} + n^2{}_{k_{ts\,\mathrm{drift}}}(f_{\mathrm{mod}}), \qquad (2.2.68)$$

thus, minimum detectable interaction force can be given by:

$$\delta F_{ts} = \delta k_{ts} A_0. \qquad (2.2.69)$$

2.2.5 Stable oscillation condition

As the tip is anchored at one end of the cantilever, it is easily to cause the tip to jump to contact the surface during the tip approaching, when the stiffness of the cantilever is less than a certain value. In the quasistatic mode, the cantilever constant *k* should be larger than the maximum of the gradient of the tip-sample force to avoid the tip jumping to the sample, as shown below: [26,27]

$$k > \max\left(-\frac{\partial F_{ts}}{\partial z}\right) = k_{ts}^{\max}. \qquad (2.2.70)$$

For the tip in the oscillating mode, the jump-to-contact of the tip can be avoided by oscillating the cantilever with a large enough amplitude *A*:

$$kA > -F_{ts}^{\max}. \qquad (2.2.71)$$

The restoring force should be larger than the maximum attractive tip-sample force. When the tip is far from the sample, the damping of the cantilever is produced by the cantilever internal dissipation and the energy loss per cycle is then given by

$$\Delta E_{cl} = 2\pi \frac{E}{Q}, \qquad (2.2.72)$$

where $E = kA^2/2$ is the energy of the cantilever. The usual phase difference between the cantilever oscillation and the driving signal is $\pi/2$. Therefore, the driving signal is $A_{drive} = Ae^{i\pi/2}/Q$. Connecting with the equation (2.2.72), A_{drive} is given by

$$|A_{drive}| = |A| \frac{\Delta E_{cl}}{2\pi E}. \qquad (2.2.73)$$

When the tip-sample interaction force is considered, an additional damping force is added, and A'_{drive} is given by

$$|A_{drive}| = |A| \frac{\Delta E_{cl} + \Delta E_{ts}}{2\pi E} = |A| \left(\frac{1}{Q} + \frac{\Delta E_{ts}}{2\pi E} \right), \tag{2.2.74}$$

hence, Q should not be much larger than $2\pi E / \Delta E_{ts}$. Otherwise, if ΔE_{ts} is larger than ΔE_{cl}, it is difficult for the oscillator circuit to maintain a constant value. A new conjecture regarding *A* and *k* is given by [28]

$$\frac{kA^2}{2} \geq \Delta E_{ts} \frac{Q}{2\pi}. \tag{2.2.75}$$

Therefore, in order to keep the cantilever in a stable oscillation, it is better to use the tip with a large amplitude or a high stiffness.

2.3 Kelvin probe force microscopy (KPFM)

2.3.1 Fundamentals of KPFM

- **Work function**

The work function ϕ is defined as the minimum energy needed to remove an electron from the highest occupied level of the solid to the vacuum near the surface. [29] It can be determined by charge states and the crystal facets of the given materials. Usually, the work function can be expressed as

$$\Phi = E_{\mathrm{VAC}} - e\mu \tag{2.3.1}$$

where E_{VAC} is the vacuum level and μ is the nearby surface potential. For a metal, the Fermi level E_{F} almost equals to $e\mu$, hence the work function can be presented as

$$\Phi = E_{\mathrm{VAC}} - E_{\mathrm{F}}. \tag{2.3.2}$$

For a metal surface, the surface electronic charge density can be represented in a jellium background as shown in Figure 2.6. The charge density in the metal is positive ρ_+, and is 0 in the vacuum.

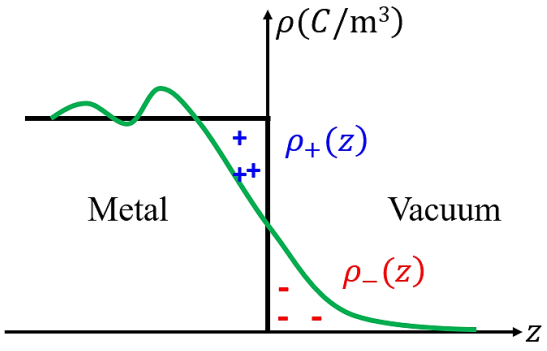

Figure 2.6 Model of a metal surface charge density.

When taking into account the electron density and the wave functions of the respective electron, the potential of the surface $\phi(z)$ is given by

$$\phi(z) = -4\pi\int_z^\infty dz'\int_{z'}^\infty dz''(\rho(z'') - \rho_+(z'')) + \phi(\infty)\,. \tag{2.3.3}$$

The change in electrostatic potential across the dipole layer created by the spilling out of the electrons at the surface can be represented by Poisson's equation

$$\Delta\phi = \phi(\infty) - \phi(-\infty)\,. \tag{2.3.4}$$

The potential inside the metal is given by $v_{eff}(z) = \phi(-\infty) + V_{xc}(\rho_+)$

$$\Delta v_{eff}(z) = v_{eff}(\infty) - v_{eff}(-\infty) = \Delta\phi - V_{xc}(\rho_+)\,. \tag{2.3.5}$$

With reference to the vacuum level, the potential is $-\Delta v_{eff}$, which is the same deep inside the metal. The energy difference between the Fermi level and $v_{eff}(-\infty)$ is $\frac{h^2k_F^2}{2m}$.[21] Therefore, the Fermi level can be represented by

$$\mu = -\Delta v_{eff}(z) + \frac{h^2k_F^2}{2m} \tag{2.3.6}$$

The work function, namely, the electron energy which has the highest value in the metal is given by

$$\Phi = |\,\mu\,| = \Delta\varphi - V_{xc}(\rho_+) - \frac{h^2k_F^2}{2m} \tag{2.3.7}$$

- **Contact Potential Difference (CPD)**

Two different conducting materials usually have the different Fermi levels. When these two materials are electrically contacted, the electrons will flow from the material with higher energy level (lower work function) to the material with lower energy level (higher work function), and the Fermi level of these two materials are equalized. In this case, the contact potential difference (CPD) can be generated. Usually, the surface with higher work function will be positively charged, and the surface with lower work function will be negatively charged due to the electrons flowing. In order to compensate for the V_{CPD}, a bias voltage is applied between these two materials to minimize the electrostatic force. Therefore, the vacuum energy level of these two materials are aligned and the applied bias voltage equals to the V_{CPD} value. Figure 2.7 schematically presents the V_{CPD} between the conductive tip and sample, and the V_{CPD} can be defined as:

$$V_{\mathrm{CPD}} = \frac{\phi_{\mathrm{t}} - \phi_{\mathrm{s}}}{-e} = \frac{\Delta\phi}{e} \tag{2.3.8}$$

where ϕ_{s} and ϕ_{t} are the work functions of the sample and tip, and e is the electronic charge.

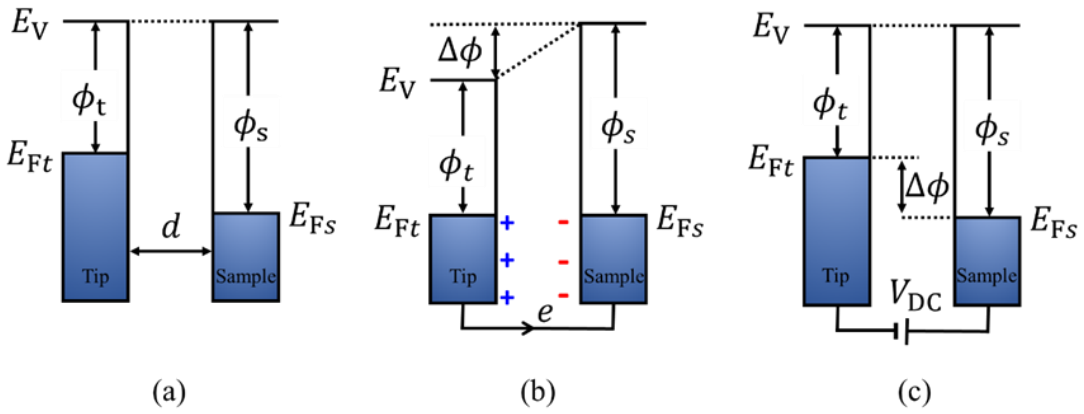

Figure 2.7 Energy levels of the AFM tip and sample: (a) tip and sample are separated by distance d with no electrical contact, (b) tip and sample are in electrical contact, and (c) a bias voltage (V_{DC}) is applied between tip and sample to compensate the CPD and the electrostatic force. E_v is the vacuum energy level. E_{Fs} and E_{Ft} are Fermi energy levels of the sample and tip, respectively.

The frequency shift Δf is proportional to the voltage difference which can be expressed as $\Delta f \propto -(V_{DC} - V_{CPD})^2$, and the relationship between the Δf and V_{DC} is presented in Figure 2.8.

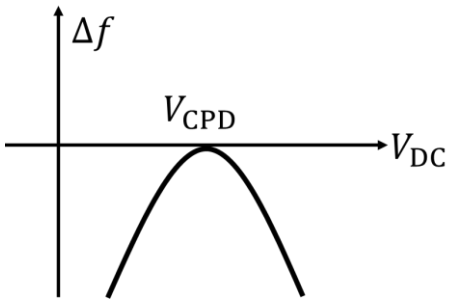

Figure 2.8 The frequency shift verse bias spectroscopy

2.3.2 FM-KPFM with bias voltage feedback

FM-KPFM is a complementary probing technique to the AFM that can measure the CPD between the tip and sample. An AC voltage (V_{AC}) and a DC voltage (V_{DC}) are applied in the KPFM measurement, in which the V_{AC} generates oscillating electrical forces between the AFM tip and sample surface, and the V_{DC} compensates the oscillating electrostatic forces that originated from CPD between tip and sample surface. The electrostatic force (F_{es}) between the AFM tip and sample can be expressed as:

$$F_{es}(z) = -\frac{1}{2}\Delta V^2 \frac{dC(z)}{dz}. \tag{2.3.9}$$

where z is the tip-sample distance, V is the potential difference between V_{CPD} and the applied bias voltage, and dC/dz is the capacitance gradient between tip and sample. As $V_{DC}+V_{AC}\sin(\omega t)$ is applied to the KPFM system, the voltage difference can be:

$$\Delta V = V_{tip} \pm V_{CPD} = (V_{DC} \pm V_{CPD}) + V_{AC}\sin(\omega t). \tag{2.3.10}$$

Note that the ± sign depends whether the bias (V_{DC}) is applied to the tip (−) or the sample (+). [22] Substituting (2.4.10) in (2.4.9), the electrostatic force can be:

$$F_{es}(z,t) = -\frac{1}{2}\frac{\partial C(z)}{\partial z}\left[(V_{DC} \pm V_{CPD}) + V_{AC}\sin(\omega t)\right]^2. \quad (2.3.11)$$

This equation can be divided into three parts:

$$F_{DC} = \frac{\partial C(z)}{\partial z}\left[\frac{1}{2}(V_{DC} \mp V_{CPD})^2\right]. \quad (2.3.12)$$

$$F_{\omega} = -\frac{\partial C(z)}{\partial z}(V_{DC} \pm V_{CPD})V_{AC}\sin(\omega t). \quad (2.3.13)$$

$$F_{2\omega} = -\frac{\partial C(z)}{\partial z}\frac{1}{4}{V_{AC}}^2\left[\cos(2\omega t) - 1\right]. \quad (2.3.14)$$

Here, F_{DC}, F_{ω}, and $F_{2\omega}$ represent the DC, ω, and 2 ω components of F_{es}, respectively. The relation between F_{DC}, F_{ω}, $F_{2\omega}$ and V_{DC} is shown in Figure 2.9.

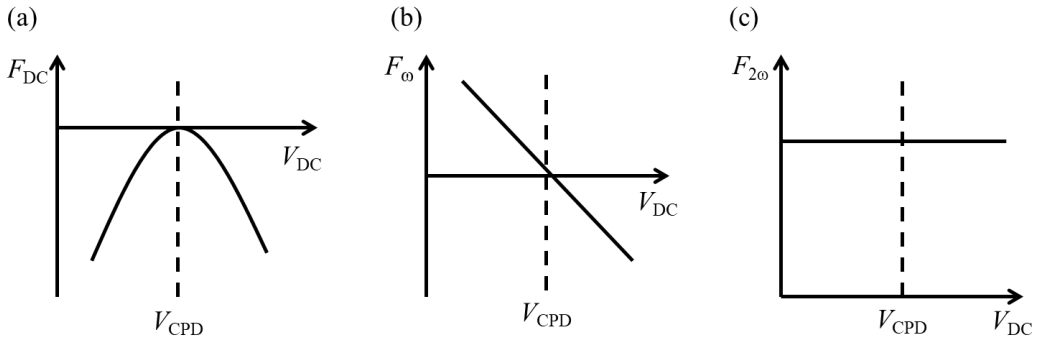

Figure 2.9 Bias voltage dependence of (a) F_{es}, (b) F_{ω}, and (c) $F_{2\omega}$. F_{DC} is a quadratic function of V_{DC}, and when $V_{DC} = V_{CPD}$, F_{es} is the minimum value. F_{ω} is a linear function of V_{dc}. $F_{2\omega}$ is a constant value.

F_{DC} ((2.4.12)) results in a static deflection of the AFM tip. F_{ω} with frequency ω ((2.4.13)) can measure the V_{CPD}, which shows a parabolic form as a function of V_{DC}, just as shown in figure 2.12(a). $F_{2\omega}$((2.4.14)) can be used for capacitance microscopy. [23] When the V_{AC} and V_{DC} are applied to the tip, the electrostatic forces will result in additional oscillating components (due to the electrical force), which will be superimposed to the mechanical oscillation of the AFM tip. In order to measure the V_{CPD},

a lock-in amplifier is used to extract the electrical force component with frequency ω (F_ω). The output signal of the lock-in amplifier is directly proportional to the difference between V_{DC} and V_{CPD}, just as shown in Figure 2.9 (b). The V_{CPD} value can be measured by the applied V_{DC}, as a result, the output signal of the lock-in amplifier is nullified and F_ω equals zero. In this way, the value of V_{DC} is acquired for each point on the sample surface, composing a map of the V_{CPD} of the whole sample surface. The schematic circuit of the FM-KPFM with bias voltage feedback is shown in Figure 2.10.

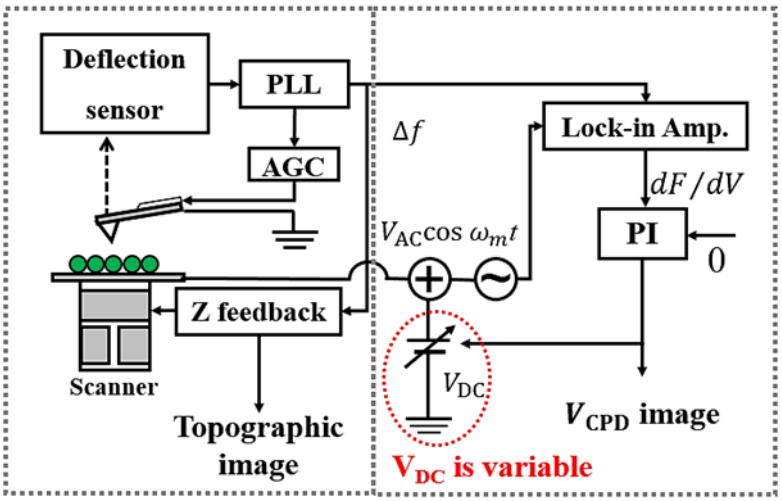

Figure 2.10 Schematic circuit of FM-KPFM with bias voltage feedback based on nc-AFM.

2.3.3 Minimum detectable CPD in KPFM

In AFM measurement, a frequency shift (Δf) and an amplitude variation (ΔA) of the cantilever vibration due to the energy dissipation are given by

$$\Delta f = -f_0 F_c/(2kA) \tag{2.3.15}$$

$$\Delta A = -QF_d/k \tag{2.3.16}$$

where f_0, k, Q and A are the resonant frequency, the spring constant, the quality factor and the oscillation amplitude of the cantilever, respectively. F_c and F_d are the tip-sample conservative

interactions and dissipative interactions, respectively.

Therefore, the minimum detectable force for conservative interaction and that for dissipative interaction are given by

$$\delta F_c = -2kA\delta f / f_0 \tag{2.3.17}$$

$$\delta F_d = k\delta A / Q \tag{2.3.18}$$

Here, δf and δA are the minimum detectable frequency and amplitude, respectively.

For typical AFM measurements in UHV, the δf and δA are given by [24]

$$\delta f = \sqrt{12} f_m n_{ds} \sqrt{B} / \pi A \tag{2.3.19}$$

$$\delta A = n_{ds} \sqrt{B} \tag{2.3.20}$$

Here the n_{ds}, B, f_m are the deflection sensor noise, bandwidth of the lock in amplifier and the modulation frequency, respectively. Therefore, δF_c and δF_d are obtained as:

$$\delta F_c = \frac{4\sqrt{3}kf_m}{\pi f_1} n_{ds} \sqrt{B}, \tag{2.3.21}$$

$$\delta F_d = \frac{k}{Q} n_{ds} \sqrt{B}, \tag{2.3.22}$$

the conservative electrostatic force (F_{esc}) is given by

$$F_{esc} = \frac{\pi \varepsilon_0 RA}{z_{t0}^2} V_{ts}^2, \tag{2.3.23}$$

while the dissipative electrostatic force (F_{esc}) is zero.

The ω_m component of the frequency shift (Δf_m) induced by the electrostatic interaction is given by

$$\Delta f_m = \frac{\pi \varepsilon_0 R f_0 V_{ac}}{k z_{t0}^2} V_{AC} V_{DC}, \tag{2.3.24}$$

from equation $\Delta f = -f_0 F_{esc}/(2kA)$, Minimum detectable CPD in FM-KPFM can be described [24]

$$\delta V_{CPD-FM} = \frac{2\sqrt{6}k_1 {z_{t0}}^2}{\pi^2 \varepsilon_0 RAV_{AC}} \frac{f_m}{f_{01}} n_{ds} \sqrt{B}. \qquad (2.3.25)$$

2.4 Scanning Tunneling Microscopy (STM)

The STM was firstly invented by G. Binning in 1981. [2] It is usually used to characterize the conductive sample surface with atomic resolution. During STM measurement, the tunneling current between the conductive tip and sample was employed as the detection signal to characterize the surface.

2.4.1 Static STM

The STM can investigate the electronic properties of the surface with atomic resolution. In STM measurement, the tunneling current between the tip and sample is used to characterize the sample surface. When a bias voltage is applied between the tip and sample, the electrons can tunnel right through the vacuum barrier to form the tunneling current. [19] The STM image is the convolution of the geometry and electronic properties of the sample surface. The basic experimental setup of the STM is shown in Figure 2.11. A sharp STM tip is brought close to the conductive sample surface, and the tunneling current can flow. Usually, the bias voltage V is applied to the sample with respect to the tip. Depending on the operation modes of constant tunneling current and constant height modes, the topography and tunneling current images can be measured.

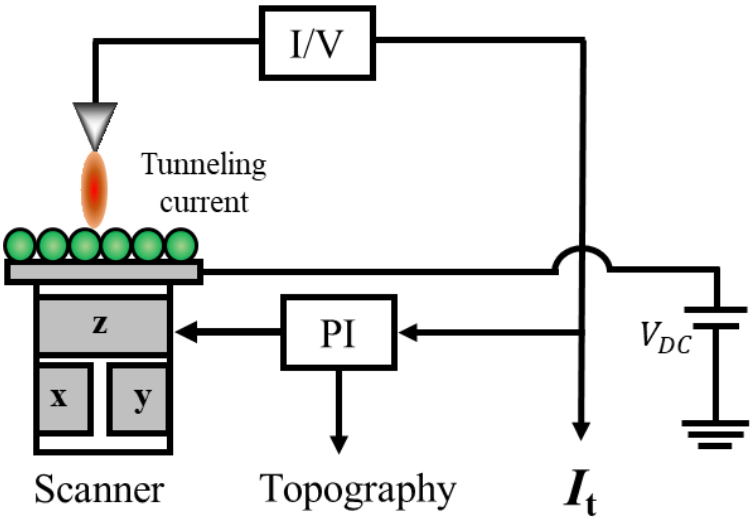

Figure 2.11 Block diagram of the experimental setup for STM.

In classical mechanics, the movement of an electron with energy moving in a potential can be expressed as below

$$\frac{p_z^2}{2m}+U(z)=E, \tag{2.4.1}$$

where m is the electron mass, P_z is the movement momentum of the electron. When $E > U(z)$, the electron has a nonzero momentum p_z. The electron can penetrate through the energy barrier. On the contrary, when $E < U(z)$, the electron cannot penetrate into any region because of the potential barrier. In quantum mechanics, the state the of the electron is described by a wave function $\Psi(z)$ satisfying the Schrödinger's equation, as shown below

$$-\frac{\hbar^2}{2m}\frac{d^2}{dz^2}\psi(z)+U(z)\psi(z)=E\psi(z), \tag{2.4.2}$$

In the classically allowed region, Eq. (2.4.2) has the solutions

$$\psi(z)=\psi(0)e^{\pm ikz} \tag{2.4.3}$$

where k is the wave vector and expressed by

$$k=\frac{\sqrt{2m(E-U)}}{\hbar}. \tag{2.4.4}$$

In the classically forbidden region, Eq. (2.4.2) has a solution

$$\psi(z)=\psi(0)e^{-\kappa z} \tag{2.4.5}$$

where κ is the decay constant and expressed by

$$\kappa=\frac{\sqrt{2m(E-U)}}{\hbar}. \tag{2.4.6}$$

It describes a state of the electron decaying on the z direction.

The probability w for an electron in the nth sample state to present at the tip surface, $z=W$, is

$$w\propto|\psi_n(0)|^2e^{-2\kappa W} \tag{2.4.7}$$

where $\Psi_n(0)$is the value of the nth sample state. κ is the decay constant of the sample state near the Fermi level in the barrier region and expressed by

$$\kappa=\frac{\sqrt{2m\phi}}{\hbar} \tag{2.4.8}$$

The tunneling current is proportional to the number of the sample states within the energy interval eV. By adding all the sample states in the energy interval eV, the tunneling current is

$$I\propto\sum_{E_n=E_F-eV}|\psi_n(0)|^2e^{-2\kappa W} \tag{2.4.9}$$

Eq. 2.4.9 can be conveniently rewritten in terms of the local density of states (LDOS), so LDOS of the sample is defied at a location z and energy E,

$$\rho_S(z,E)\equiv\frac{1}{\varepsilon}\sum_{E_n=E_F-eV}^{E}|\psi_n(z)|^2. \tag{2.4.10}$$

Then the tunneling current can also be rewritten in terms of the LDOS of sample as

$$I\propto V\rho_S(0,E_F)e^{-2\kappa W} \tag{2.4.11}$$

Depending on the polarities of the applied bias voltage, the empty and filled states STM images can be recorded. In the empty state image measurement, a positive bias voltage V is applied to the sample,

and the electrons can tunnel from the filled states of the tip to the empty states in the valance band of the sample. In this way, the tunneling current can flow from the tip to the sample. We can measure the integrated density of full states above the Fermi level in the sample. On the contrary, when a negative bias voltage $-V$ is applied to the sample, and the electrons can tunnel from the filled states of the sample to the empty states of the tip. In this way, the tunneling current can flow from the sample to the tip, and we can measure the integrated density of full states below the Fermi level in the sample. The schematic of the tip-sample tunneling in empty state and filled state STM measurement is presented in Figure 2.12.

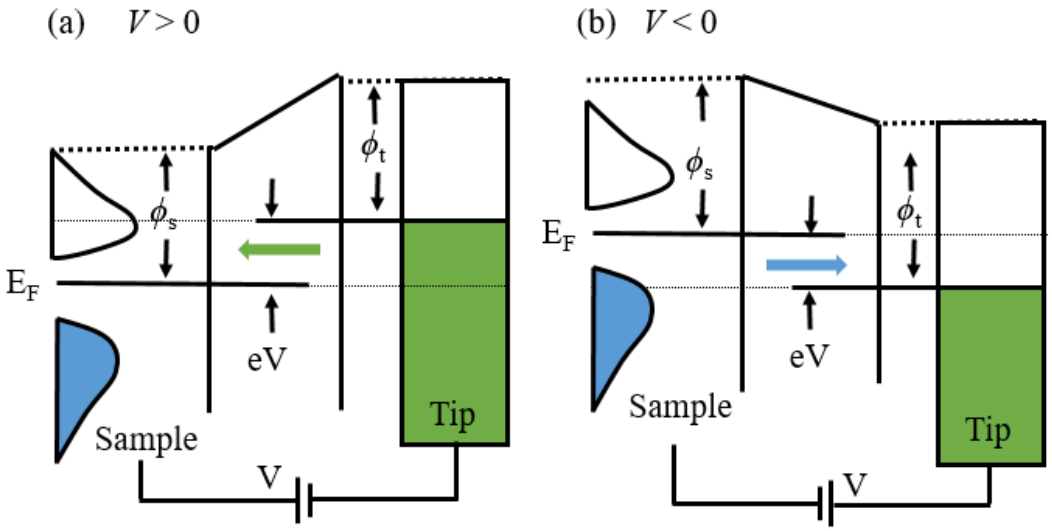

Figure 2.12 Schematic of the tip-sample tunneling in empty state (a) and filled state (b) STM measurement.

2.4.2 Dynamic STM

The simultaneous STM and AFM measurement can be performed using the conductive tip of the cantilever and sample. It is usually performed in the constant height mode in order to avoid the crosstalk between the frequency shift and tunneling current signals. The tunneling current is recorded

by a current-to-voltage converter with a limited bandwidth much smaller than the oscillation frequency of the cantilever f_0. [20] The recorded tunneling current I_t is actually the time-averaged tunneling current $\langle I_t \rangle$, and the tunneling current I_t changes exponentially with the tip-sample distance, as shown in figure 2.13.

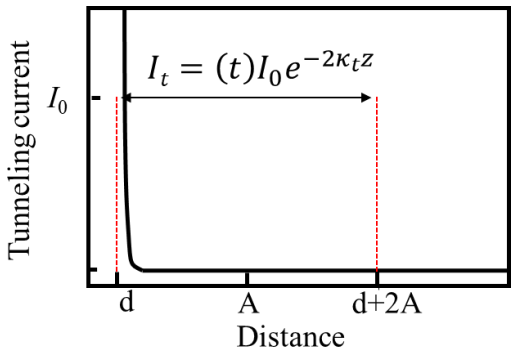

Figure 2.13 Tunneling current I_t versus distance between a sample and oscillating cantilever. d is the closest tip position and the A is the tip oscillation amplitude.

The impact of the modulation of the tip-sample distance on the tunneling current is presented in the Figure 2.14. The harmonic modulation results in the sharp peaks in the current signal. As a consequence, the frequency spectrum of the tunneling current shows higher harmonics of the modulation. Current signal at higher order frequency components is neglected due to the limitation of current amplifier.

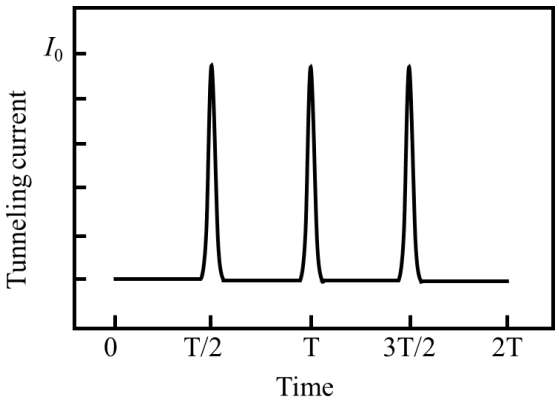

Figure 2.14 Tunneling current versus time with an oscillating cantilever. [30]

The measured tunneling current is given by the time-average over one oscillation cycle.

$$< I >= \frac{1}{T}\int_0^T I(t)dt = g(A,V) \times I_0 \tag{2.4.12}$$

where I_0 is the tunneling current at the closest tip-sample distance and $g(A,V)$ is the proportional coefficient as a function of the oscillation amplitude and sample bias voltage. In the simultaneous STM and AFM measurement, the stiff tip with small oscillation amplitude A is used in order to decrease the noise of the tunneling current measurement with increasing average tunneling current.

2.5 Summary

In this chapter, we present a brief review of the scanning probe microscopy, which will be employed to acquire experimental results in this dissertation. Some key principles and theories are discussed in detail, for example, deconvolution of interaction force from frequency shift, and FM-KPFM with bias voltage feedback method.

Chapter 3 Low temperature UHV SPM

3.1 Introduction

In this chapter, we briefly introduce the setup of the low temperature UHV SPM. In section 3.2, the equipment of the low temperature UHV nc-AFM system and the corresponding vibration isolation system are presented. In section 3.3, the AFM unit including sample and cantilever stages and the deflection detection system are introduced. In section 3.4, we focus on the introduction of the operation circuits, including the FM-AFM, FM-KPFM and STM measurement. In section 3.5, we introduce the sample and cantilever preparation.

3.2 Equipment of low temperature UHV nc-AFM

3.2.1 Chambers

In our study, the experimental equipment is mainly base on the low temperature UHV nc-AFM system, as shown in Figure 3.1 and the corresponding the schematic of side and top views of the system in Figure 3.2. The system consists of a load-lock chamber, a preparation chamber, and an observation chamber, which are all connected and fixed on the active vibration isolation system to avoid the vibration source.

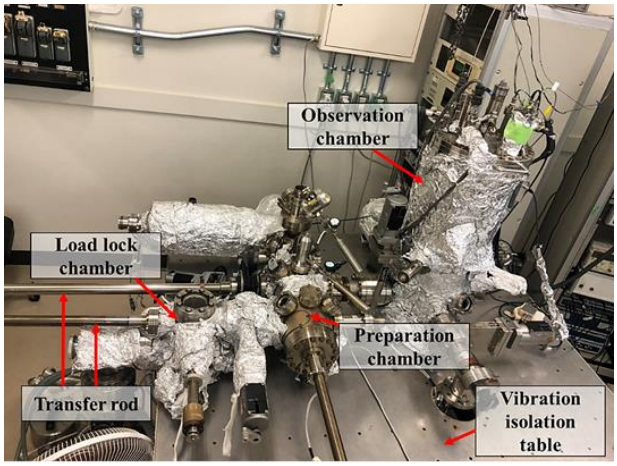

Figure 3.1 Low temperature UHV nc-AFM system.

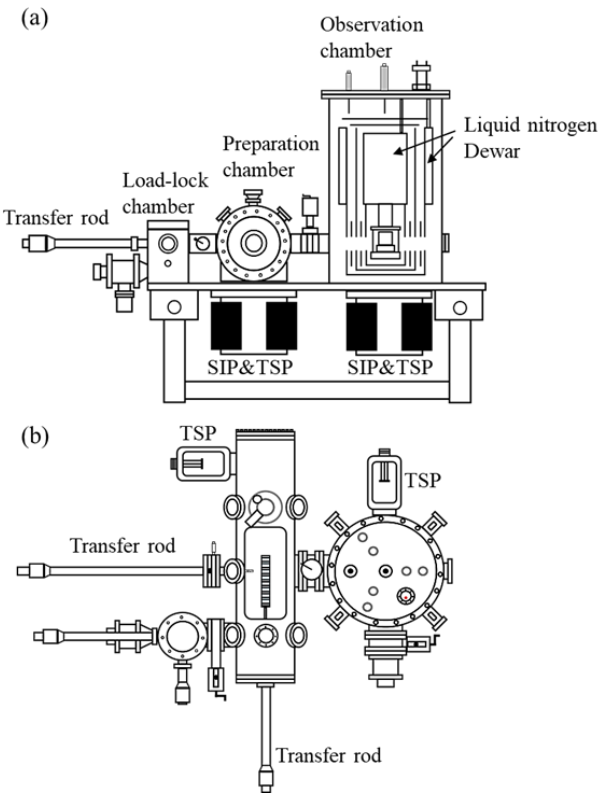

Figure 3.2 schematic of the side (a) and top (b) views of the low temperature UHV nc-AFM.

- **Load-lock chamber**

The load-lock chamber is used for cantilever and sample exchanging between atmosphere and

high vacuum conditions. A gate valve is employed to divide the load lock chamber from the preparation chamber. In order to transfer the tips and sample between load lock chamber and preparation chamber, a transfer rod is used. The vacuum condition can be maintained at about 10^{-10} Torr with a Rotary Pump (RP) and Turbo Molecular Pump (TMP, displacement volume 250L/sec).

- **Preparation chamber**

The preparation chamber is used for preparing sample and tip before measurement. The base vacuum condition can be kept below 3×10^{-11} Torr at room temperature with one Sputter Ion Pump (SIP, displacement volume 70L/sec) and two Titan Sublimation Pump (TSP, displacement volume 1600L/sec). Specifically, it is equipped with an electric heating system for tip and sample annealing, and an Ar-ion sputtering gun for tip and sample sputtering. In addition, an oxygen cylinder with pure oxygen gas is used to oxidize the sample surface. The preparation chamber is separated by a gate valve form the observation chamber, and a transfer rod is used to exchange tip and sample between preparation and observation chambers under the UHV.

- **Observation chamber**

The observation chamber is a chamber that for all the measurement at low temperature. It is mainly composed of an nc-AFM measurement unit and a cryostat. The cryostat consists a two-layer dewar including an inner tank and an outer tank with liquid nitrogen. A triple shield is used to prevent the external heat radiation. The measurement unit can be cooled down to 78 K bu touching the bottom of the dewar with liquid nitrogen for more than 48 hours. The base pressure can be kept better than 3×10^{-11} Torr. An inner vibration isolator is fixed to remove the internal unit and shield vibration.

3.2.2 Vibration isolation system

The vibration isolation system is employed to keep a stable measurement condition to realize the measurements with atomic resolution. During the measurement, the vibration must be suppressed below 0.01Å. In our experiment, the active vibration isolation platform and the vibration isolation unit are used to obtain the effective isolation.

- **Active vibration isolation platform**

The whole nc-AFM measurement system is fixed on top of an active vibration isolation platform to avoid the vibration, especially the low frequency vibrations from approximately 1 to 200 Hz. It consists of sensors, feedback circuit controller and actuators, as shown in Figure 3.3. The sensor can detect the displacement, velocity or acceleration, and the signals can be fed to the feedback circuit controller. Then the controller can activate the actuators to convert the electric voltage to a mechanical force. The mechanical force of the actuators has the same magnitude but a phase angle of 180 degrees as the excitation force, which results in the force cancellation.

- **Vibration isolation unit**

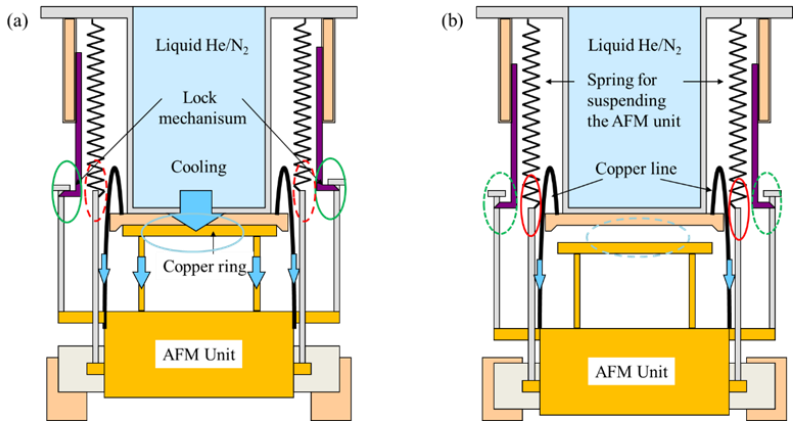

Figure 3.3 Vibration isolation mechanism of SPM unit

The nc-AFM unit cell is suspended from the bottom of the dewar by a coil spring, as shown in Figure 3.3. Magnetic damper is used to prevent vibration of SPM unit cell itself, and four magnets are installed

on the side of the chamber to eliminate the unit interior and shield vibration.

3.2.3 Preparation system

- **Ion-sputtering system**

In our experiment, the ion-sputtering system was used to prepare the clean tip and sample surface, which is schematically presented in Figure 3.4.

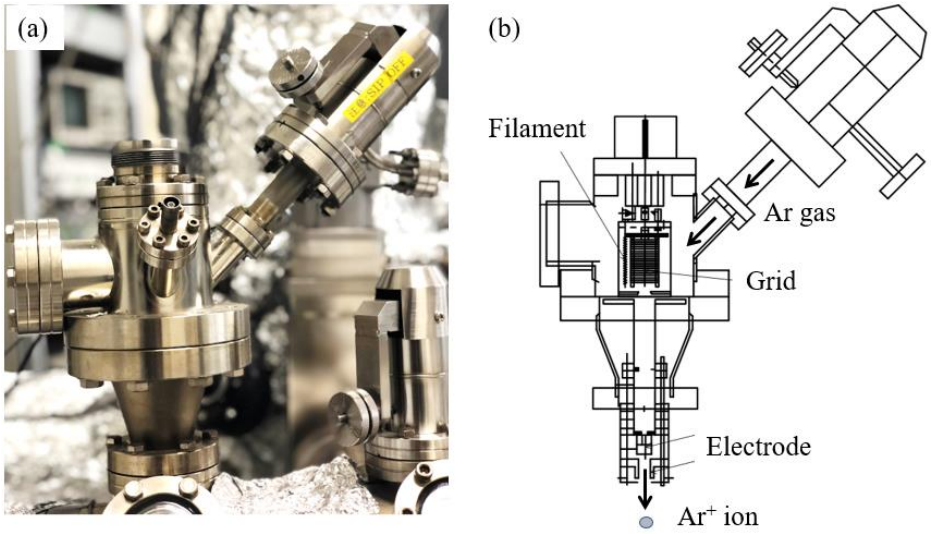

Figure 3.4 (a) Photograph and (b) schematic of the ion-sputtering system.

One ion gun is fixed on the preparation chamber, and the Ar gas atoms are ionized in to the Ar^+ ions by the thermal electrons emitted from the filament in the ion gun. By using the high voltage of the electrode, Ar^+ ions are accelerated to collide against the substrate surface, which can remove the dust attached to the substrate surface and the tip apex.

- **Gas-inlet system**

The mini cylinder is directly fixed on the preparation chamber, in which the O_2, CO gas with high purity are inside. Usually, the O_2 or CO gas is directly exposed to the sample surface in the preparation chamber at room temperature. The photograph of our mini cylinder used in our

experiment is shown in Figure 3.5.

Figure 3.5 Photograph of the mini cylinder.

- **Electron beam evaporation**

One electron beam evaporation system is used in this study to evaporate the Au atoms on sample surface, which is EFM3 manufactured by Omicron. There are mainly four components in the electron beam evaporation system, including the tungsten filament for emitting thermoelectrons, a crucible containing the Au wire, a shutter mechanism and a flux monitor. First, the thermal electrons are emitted from the tungsten filament with a high voltage, and collide with the Au. The temperature of the Au rises due to the impact heat of the thermal electrons, and the Au atoms can be ionized and evaporated, which is accelerated by the acceleration voltage. At this time, when the ionized Au atoms passes through the Flux monitor, a weak current flows by passing through the Flux monitor, and the amount of the current is proportional to the deposition amount. Therefore, the deposition amount can be estimated every hour by the Flux monitor. In addition, the generation of gas from the wall surface is suppressed by water cooling. The photograph and schematic of the electron beam evaporation system are shown in Figure 3.6.

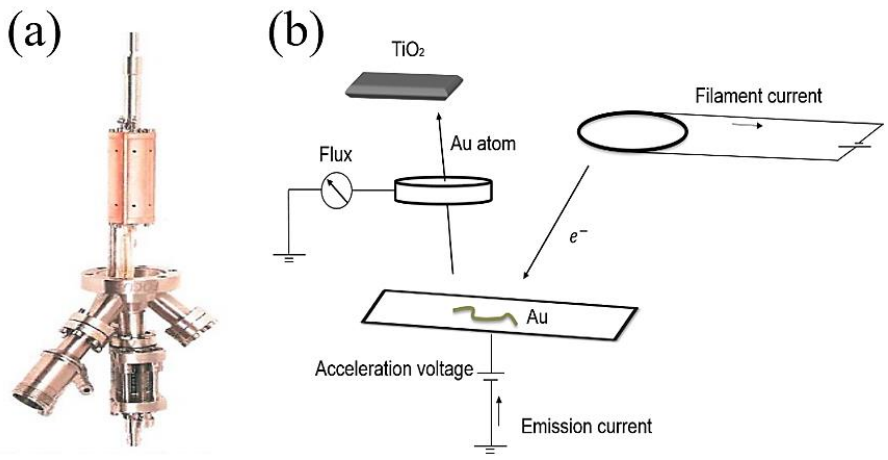

Figure 3.6 (a) Photograph and (b) schematic of the electron beam evaporation system.

The amount d (ML) of the material deposited on the sample surface is calculated as:

$$d = \frac{8 \times 10^6}{1.2} \cdot \frac{pr^2 t}{L^2 \sqrt{MT}} \tag{3.1}$$

where p is the saturated vapor pressure of the deposition material, r is the radius of the rod, t is the deposition time, L is the distance from the deposition material to the sample, M is the molecular weight of the deposition material, and T is the temperature of the deposition source.

3.3 AFM unit

The nc-AFM unit mainly consists of a sample stage and the signal detection system, as shown in Figure 3.7. In the sample stage, the approaching piezoelectric actuator can allow the sample to move toward the cantilever, in which a cantilever holder is fixed on. In addition, the tube scanner can be used for three-dimensional movements of the sample. The signal detection system includes cantilever stage and laser loop. A cantilever holder is fixed on the cantilever stage, and the laser loop is designed to detect the oscillation of cantilever. The advantages of this AFM unit are the high mechanical stability, easy exchanging of the sample and cantilever.

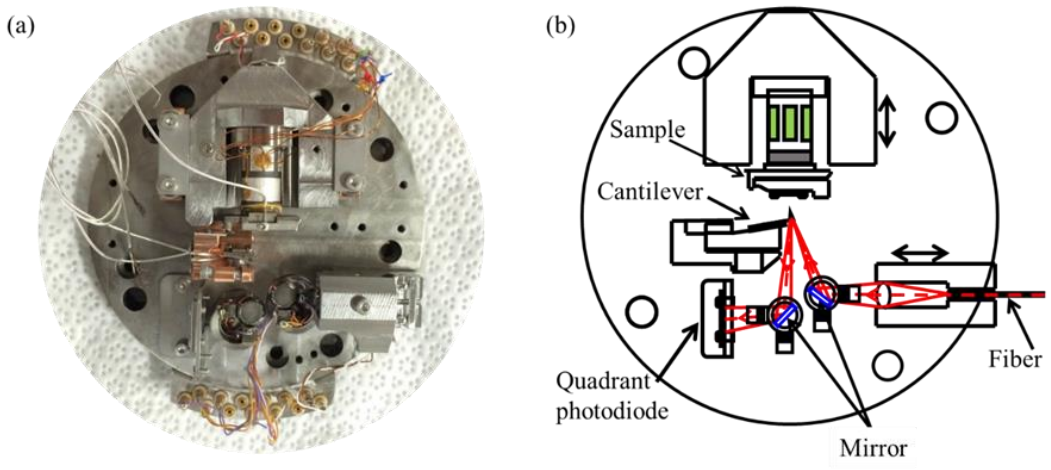

Figure 3.7 Top view of the AFM unit photo (a) and schematic (b).

3.3.1 Sample and cantilever stages

- **Sample stage**

The movement of the sample stage is precisely aligned by the stick-slip approaching mechanism. In the stick-slip approaching part, the approaching piezoelectric actuator is the inertial driven shear piezoelectric element stack, which can generate the stick-slip motion by the stick-slip actuation technology. [1] The sapphire plate is attached on the bottom of the stage to reduce the friction, and a hemispherical ruby ball is fixed on the top of the actuator. The piezoelectric elements are stacked on top of each other. When an external electric filed is applied on both sides of the stacking piezoelectric elements, it can result in the deformation of the elements in a shear direction, as schematically presented in Figure 3.8.

Usually, a saw-tooth voltage is applied to the shearing piezoelectric elements to motivate the stick-slip motion of the sample stage. Firstly, the applied bias voltage gradually increases, which will result in the deformation of the shearing piezoelectric actuators and the movement of the sample stage due to the friction between the ruby ball and the sapphire plate. This process is called

stick mode. When the bias voltage reaches its maximum, it drops suddenly, and the sample stage cannot follow ideally the retraction of the shearing piezoelectric actuators due to its inertia. The sample stage will stay in the place, as shown in Figure 3.8(a), and this process is called the slip mode. The sample stage can gradually approach the tip by repeating this process.

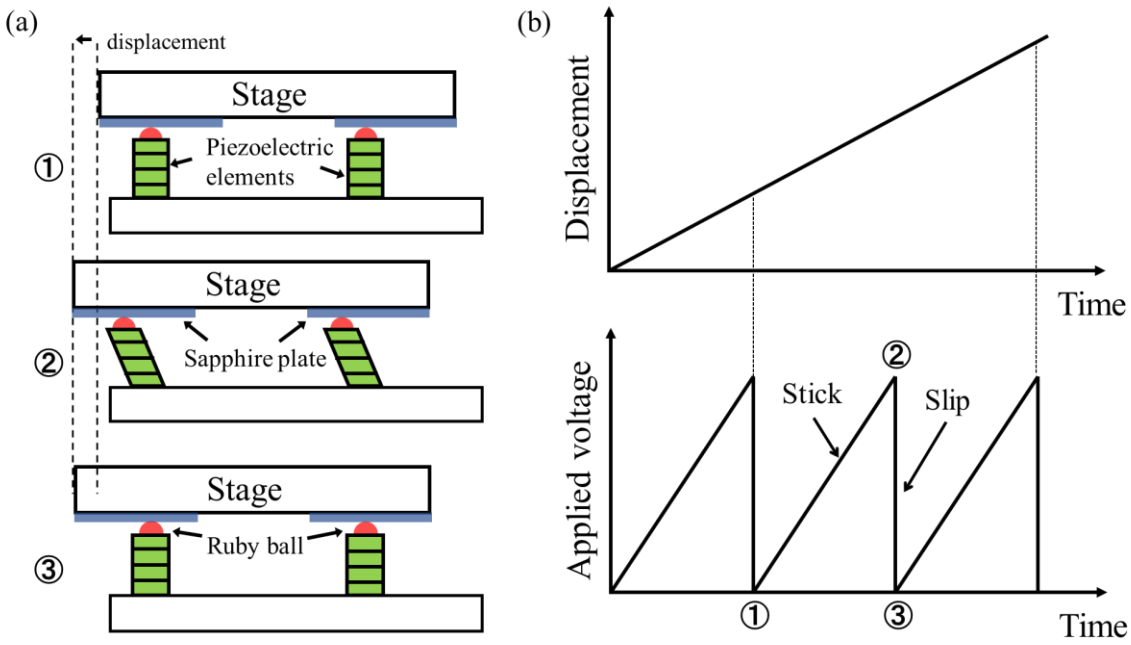

Figure 3.8 Operating mechanism of the stick-slip actuator. The schematic of stick-slip setup (a) and the stage displacement dependence on the applied voltage (b).

On the sample stage, the key component is a piezoelectric scanner (sometimes called tube piezo), which is fabricated by the PZT with high piezo constants and resonance frequency. The tube scanner can control the sample movement in X, Y and Z directions. Six electrodes, including ±X, ±Y and ±Z, are attached to the outside and inside of the tube. The top half of the tube piezo outside is attached to the +Z electrode, and the bottom half of tube piezo was attached to neighboring ±X and ±Y four electrodes, which are oppositely attached, respectively, as shown in Figure 3.9. The

inner continuous metal coating is connected to the -Z voltage, which is grounded. The whole piezo has a same polarization direction. With a positive voltage applied to +Z electrode, the polarization is formed with opposite direction due to the electric field formation with opposite direction. As a result, the whole tube can extend, as shown in Figure 3.9 (d). On the other hand, when the voltage is applied to ±X electrodes, it can result in the polarization of +X side and –X side with same direction. The left part (close to +X electrode) extended, and the right electrode (close to the –X electrode) shrunk, which induce the tube piezo twist to the right, as shown in Figure 3.7 (e).

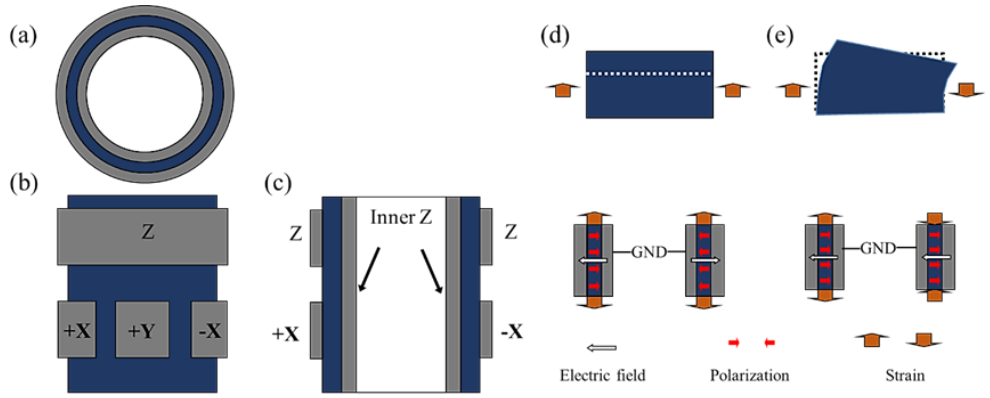

Figure 3.7. Schematic of the tube scanner.

Figure 3.9 (a-c) Schematic structure of the tube scanner. (d-e) The schematic of the tube piezo extending and twisting, respectively.

- **Cantilever stage**

The cantilever stage consists of cantilever holder supporter and cantilever holder, as shown in Figure 3.10. The base plate of the cantilever holder is made of ferromagnetic nickel, and the cantilever holder is fixed on the cantilever holder supporter by the magnet force with a magnet attached on the cantilever holder support. A spring electrode is used for the stabilization of the

cantilever onto the cantilever holder. Between the cantilever holder support and the lower electrode of the piezoelectric actuator, a thin mica plate is used as an insulator. Three ruby balls are used to connect the cantilever holder and act as electrical channels.

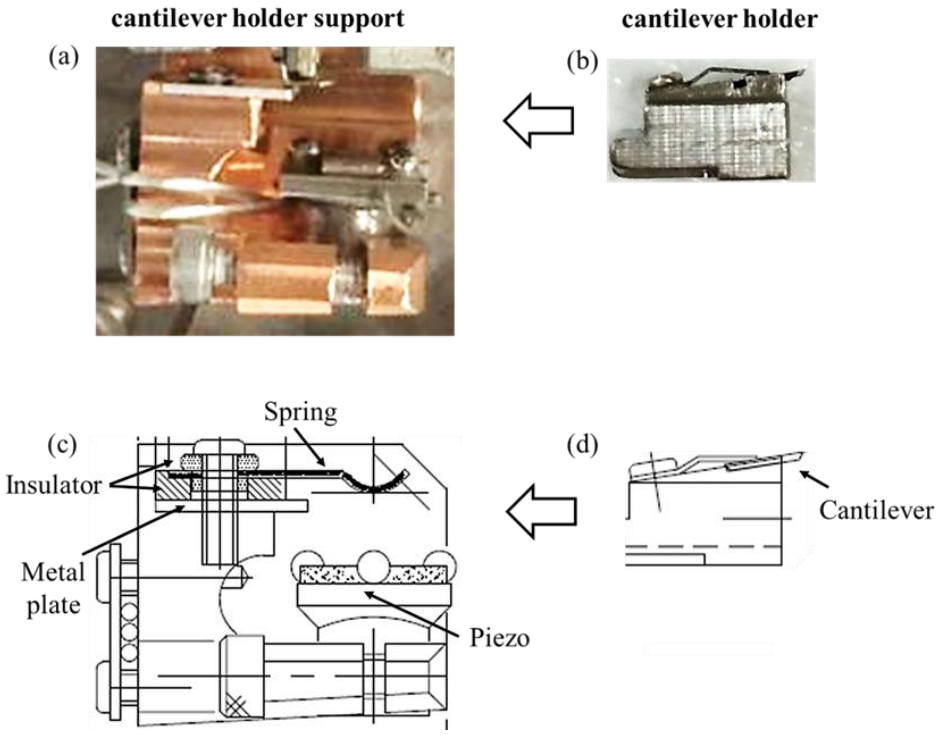

Figure 3.10 (a, b) Photography and (c, d) side views of the cantilever holder support and the cantilever holder.

3.3.2 Deflection detection system

In this study, as the FM-AFM is used to obtain the experimental results, the frequency shift of the resonant frequency of the oscillating cantilever is detected by the phase-lock loop (PLL) as the imaging signal. Therefore, it is necessary to detect the deflection of the cantilever. A wide variety of deflection detection methods of the cantilever have been used, such as piezoelectric force sensor [2-3], optical beam deflection detection (OBD) [4] and optical interferometer

detection [5]. In this study, the optical beam deflection (OBD) detection method is used due to its higher sensitivity, and the principle of the OBD detection is briefly introduced as below.

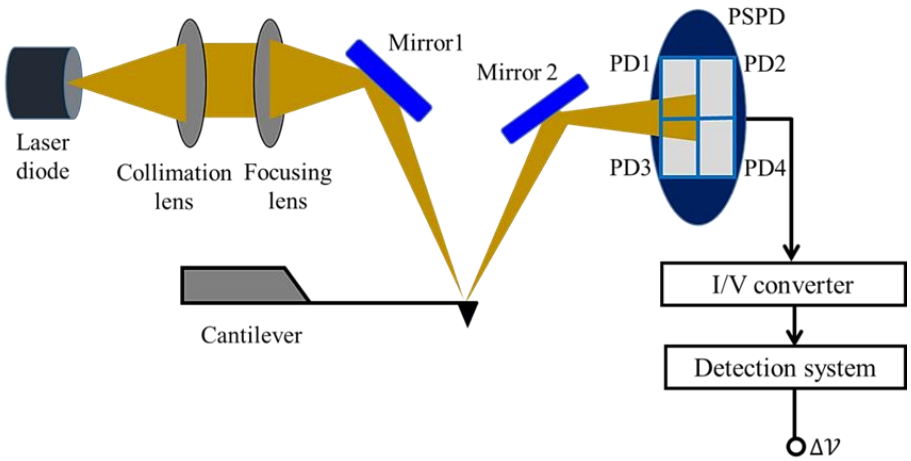

Figure 3.11 Schematic diagram of experimental setup of the OBD method.

The schematic diagram of the experimental setup of the OBD method is shown in Figure 3.11. The laser beam is generated by laser diode outside of the chamber, and an optical fiber is used to transmit the laser into the chamber. Two lenses (collimation lens and focusing lens) are used to focus the laser beam, and then it is irradiated onto the backside of the cantilever by the mirror 1. A position sensitive photodetector (PSPD) can detect the reflected laser beam by the mirror 2. By adjusting the two mirrors to align the laser beam, the laser spot can be positioned on the PSPD center. The laser spot position in the PSPD can be changed due to the cantilever deflection, which will result in the photocurrent change from the PSPD. A voltage amplifier by a I/V convertor is used to amplify the detected photocurrent. As a result, the voltage signal is detected as a detecting signal.

- **Principle of optical beam deflection detection**

The principle of the OBD detection method is introduced in Figure 3.12. [6-7] The deflection

angle of the cantilever and laser beam can change along with the displacement of the cantilever during scanning, which is detected as the measuring signal by the measuring system.

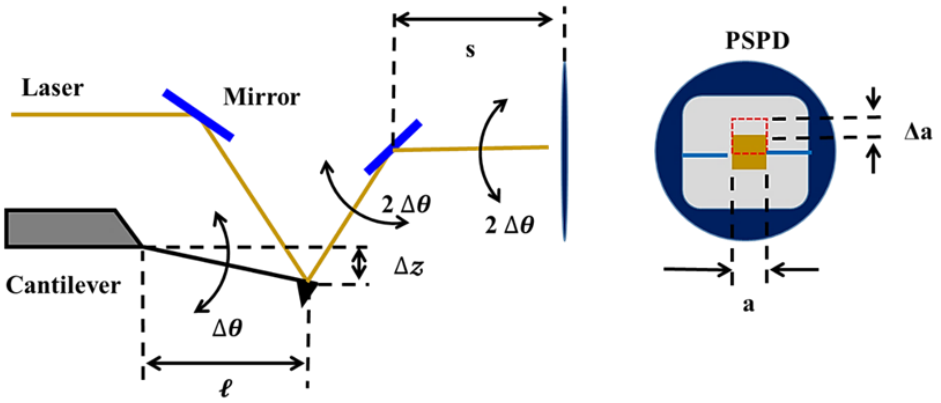

Figure 3.12 Schematic of experimental setup of the OBD method.

The relationship between the displacement and deflection angle of the cantilever is given as follows [6]

$$\Delta\theta = \frac{3}{2}\frac{\Delta z}{\ell} \tag{3.2}$$

Here, l is the length of the cantilever.

The deflection of the cantilever can induce the laser beam deflection on the PSPD, and its value is $2\Delta\theta$. Laser spot position on the PSPD is shifted Δa by deflection.

$$\Delta a = 2\Delta\theta \cdot s\,. \tag{3.3}$$

Substituting the equation 3.1 into 3.2, the expression is written as below

$$\Delta a = 3\frac{s}{\ell}\Delta z\,. \tag{3.4}$$

Here, s is the distance from the laser point on the second mirror to the photodiode. The change in spot position causes the difference of the photocurrent in the photodiode. When the laser spot is assumed to square, the difference of photocurrents is expressed as follows

$$\Delta i_1 = \eta P \frac{2}{a} \Delta a \,. \tag{3.5}$$

Here, η, P, and a are efficiency of the light-to-current conversion at the photodiode, total power of the laser beam irradiated onto the PSPD, and diameter of the laser spot on the PSPD, respectively.

- **Detection system circuit**

PSPD consists of four adjacent photodiodes. The top half photocurrent A is the sum of the PD1 and PD 2. The lower half photocurrent B is the sum of PD3 and PD 4. The difference of the photocurrent is equal to A-B. The detection system circuit contains adder and subtraction circuit, which is shown in Figure 3.13.[8]

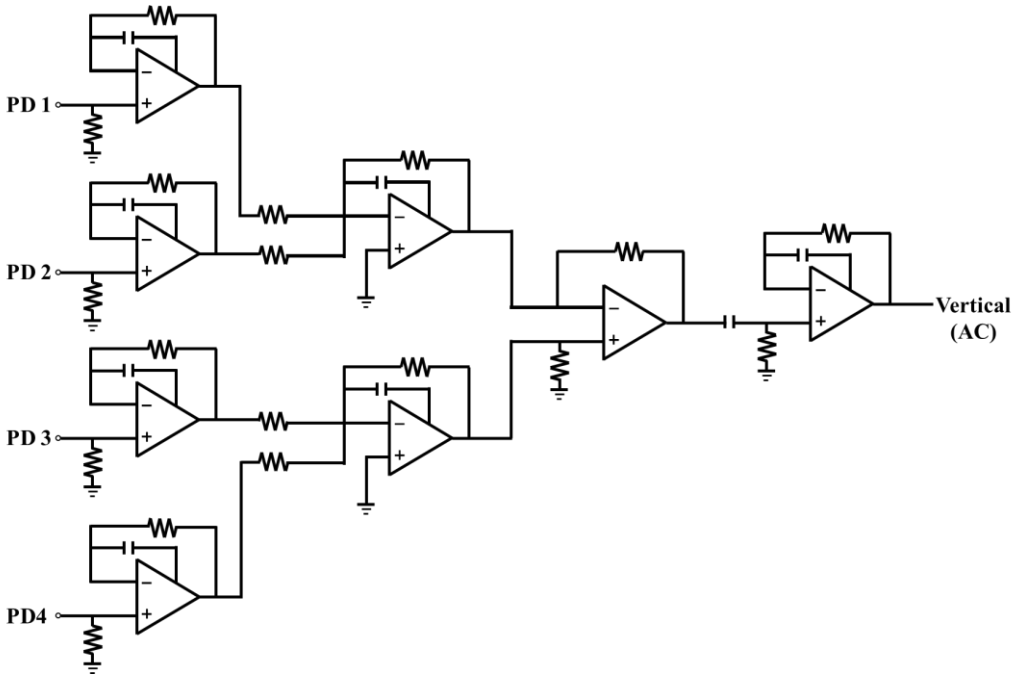

Figure 3.13 Arithmetic circuit of the OBD method.

3.4 Circuits of the operation system

3.4.1 FM-AFM controller circuit

As we have discussed above, the FM-AFM and FM-KPFM measurement modes are used in our experiments. The controller circuit of FM-AFM used in our experiment is shown in Figure 3.14.

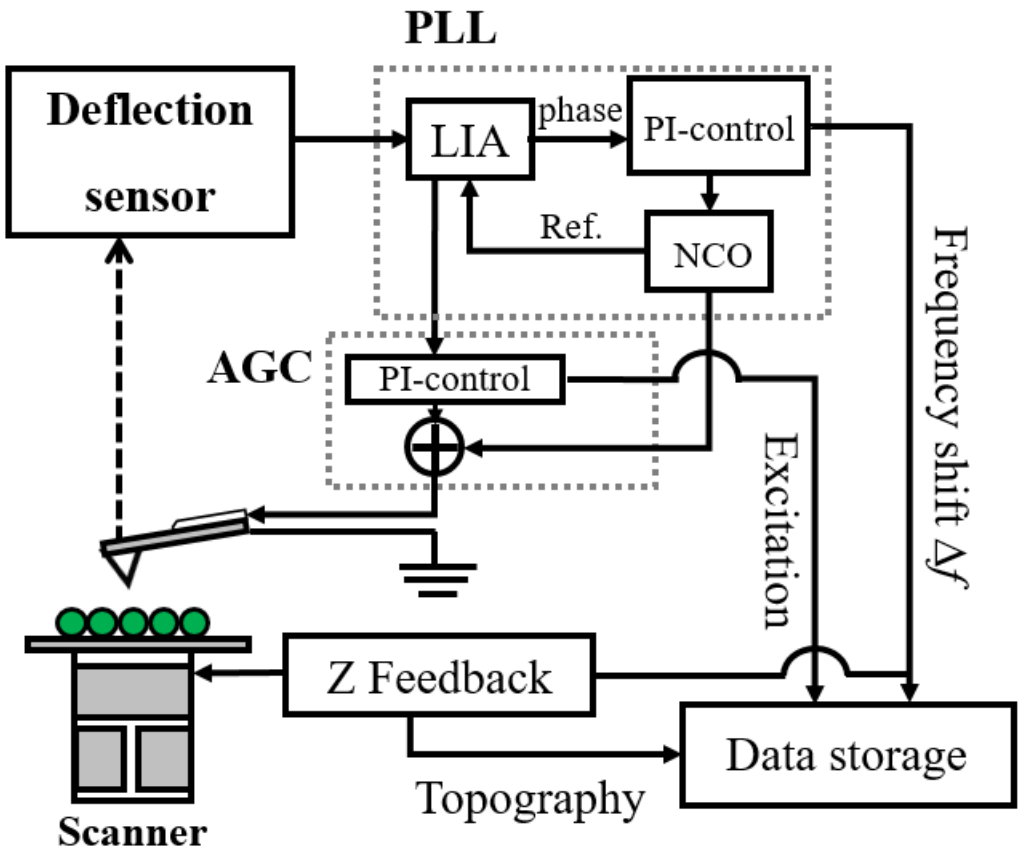

Figure 3.14 Schematic controller circuit of FM-AFM.

In the FM-AFM measurement, the frequency shift of the cantilever vibrating at around it resonance frequency is used as the characterization signal, in which the amplitude of the cantilever oscillation keeps constant. Firstly, the amplitude and phase of the signal are detected by the lock-in amplifier (LIA) in the phase-lock-loop (PLL) circuit. The phase signal is input into the PI-control. It is found

that the actual vibration phase is delayed by 90 degrees when the cantilever is excited at its resonance frequency. Therefore, the signal of the vibration phase is input to the numerically controlled oscillator (NCO), and then is fed back to the cantilever. In this way, the phase difference between the vibration signal of the cantilever and the excitation signal always becomes -90 degrees. The amplitude of the detected signal is input into the automatic gain control (AGC) circuit, in which the PI-control is used to be equal to the oscillated amplitude when it is fed back to the cantilever.

3.4.2 FM-KPFM controller circuit

As we have introduced above, in order to measure the topographic and local contact potential difference (V_{LCPD}) images simultaneously, Kelvin probe force microscopy, operated in frequency modulation mode (FM-KPFM) based on the nc-AFM, was used. Figure 3.15 shows the schematic diagram of the simultaneous nc-AFM and FM-KPFM measurement circuit with bias voltage feedback. In this circuit, a phase lock loop (PLL) was used to generate the frequency shift (Δf) signal from the cantilever deflection detected by the optical beam deflection (OBD) system. The Δf was divided into two circuits, in which one was used to obtain the topographic image and the other one was fed into a lock-in amplifier to obtain the V_{LCPD} image. An AC bias voltage, $V_{\mathrm{AC}} \cos\omega_{\mathrm{m}}t$, generated by an oscillator was used as a reference signal. The ω_{m} component of the Δf was measured by a lock-in amplifier and used as a feedback signal. By controlling the proportional–integral (PI) controller during the surface potential measurement, V_{LCPD} and Δf images with atomic resolution could be obtained simultaneously.

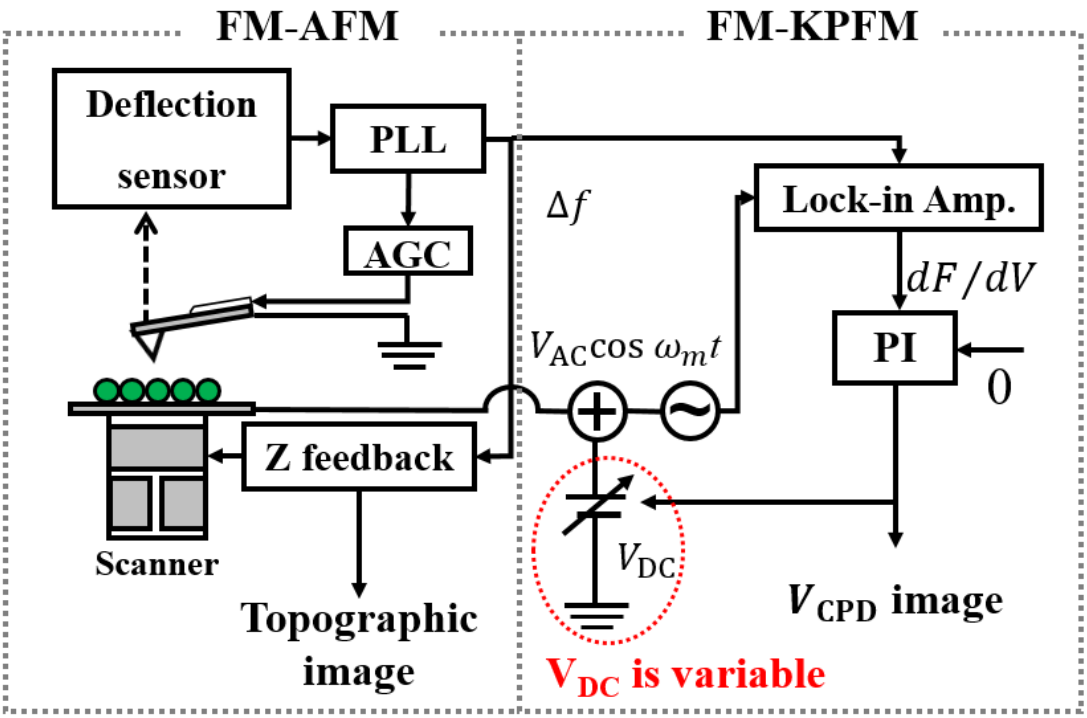

Figure 3.15 Schematic controller circuit of FM-KPFM with bias voltage feedback method.

3.4.3 FM-AFM and STM controller circuit

In our experiment, since the conductive tip (Ir-coated Si tip) was used for the AFM measurement, we can obtain the topography and tunneling current signals simultaneously, namely, the simultaneous AFM and STM measurement. The schematic circuit of the simultaneous AFM and STM measurement is shown in Figure 3.16.

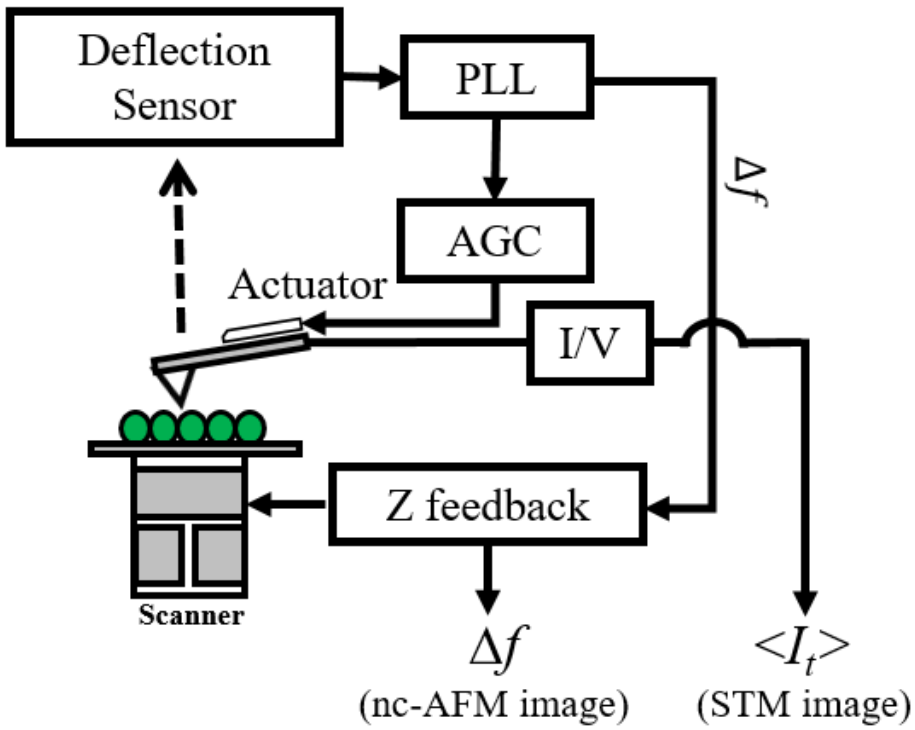

Figure 3.16 Schematic controller circuit of simultaneous AFM and STM measurement method.

The tunneling current is directly obtained from the tip and converted into a voltage single by an I/V converter with a limited bandwidth much smaller than the oscillation frequency of the cantilever f_0. In order to avoid the crosstalk between the topographic and tunneling current signals during simultaneous AFM and STM measurement, the measurement is usually performed in the constant height mode to keep a constant tip-sample distance, rather than the constant frequency shift mode. Note here that the the recorded tunneling current I_t is actually the time-averaged tunneling current $\langle I_t \rangle$, and the tunneling current I_t changes exponentially with the tip-sample distance, as we have introduced in Chapter 2.

3.5 Sample and cantilever

3.5.1 Sample fixation and preparation

- **Sample fixation**

In this study, a rutile TiO_2(110)-(1×1) surface (from Furuuchi Chemical Corporation) is used as

the sample. And a sample holder is employed for sample fixation and preparation. The base plate of the sample holder is made of alumina because of its low thermal conductivity and outgassing at high temperature. Two magnets on the backside of the sample holder support are used to fix the sample holder.

Now we introduce the fixation method of the rutile TiO_2 sample in our experiment. Since the rutile TiO_2 in its stoichiometric form is an insulator, the direct electric annealing is difficult. In addition, though the introduction of point defects can transform it to the semiconductor, the temperature variation occurs due to the influence of the defects structures. Therefore, the indirect heating method is used for sample annealing. Two electrodes connect to the sample holder bottom to apply bias voltage. The metal tantalum (Ta) foil with thickness of 0.01 mm is used as the heater, and the insulator PBN sheet is sandwiched by the Ta foil to indirectly heat the sample, on which the sample is mounted on one additional PBN sheet. This structure can avoid the deformation of the Ta foil during annealing. In addition, the upper part of the sample is fixed with a Ta foil and a PBN sheet, respectively, to prevent current from flowing through the sample and to apply a bias voltage to the sample. The detailed structure of the sample fixation is schematically shown in Figure 3.17.

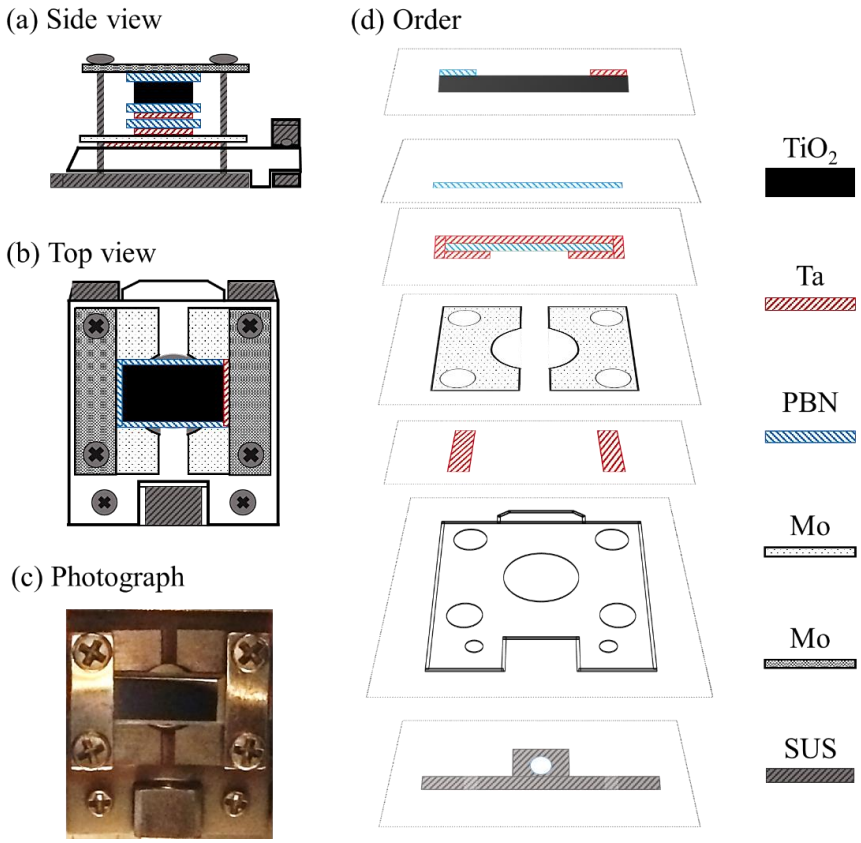

Figure 3.17. Schematic of the sample fixation structure and the components in order.

- **Rutile TiO_2(110)-(1 × 1) preparation**

In this study, a rutile TiO_2(110)-(1×1) surface (from Furuuchi Chemical Corporation) is used as the sample, and it is usually prepared by repeated cycles of Ar ion bombardment and annealing, which is schematically presented in Figure 3.18.

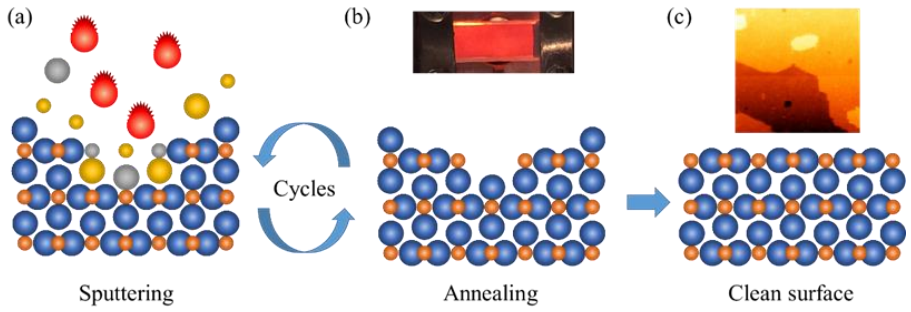

Figure 3.18 Schematic of repeated cycles of Ar ion bombardment and annealing of the rutile

TiO_2(110)-(1×1) surface.

- **Ar ion sputtering**

The rutile TiO_2(110)-(1×1) surface is firstly treated by Ar ion sputtering using the ion gun. During Ar ion sputtering, the emission current is about 22 μA and ion energy is about 1 keV, and vacuum condition is maintained at 1×10^{-6} Torr for 15 min.

- **Thermal annealing**

After sputtering, the rutile TiO_2(110)-(1×1) surface becomes rough. Therefore, thermal annealing is necessary to flatten the rough substrate surface at the atomic-scale. In our experiment, it is heated to a temperature at about 1000K for 30 min, at which the surface atoms can thermally diffuse, and the rough surface can become a uniform and stable surface.

3.5.2 Cantilever

- **Cantilever property**

The resonance frequency f_0 and the spring constant k are the important properties of the cantilever, which is dependent on its dimensions. The relationship between its dimension with a rectangular cross section and the mechanical properties are expressed as below:

$$f_0 = \mathrm{A}\sqrt{\frac{E}{\rho}}\frac{h}{l^2} \tag{3.6}$$

$$k = \frac{Eah}{4l^3} \tag{3.7}$$

Where A is a constant (0.162 here), E is the Young's modulus, ρ is the material density of the cantilever, and a, h and l are the width, thickness, and length of the cantilever, as schematically shown in Figure 3.19.

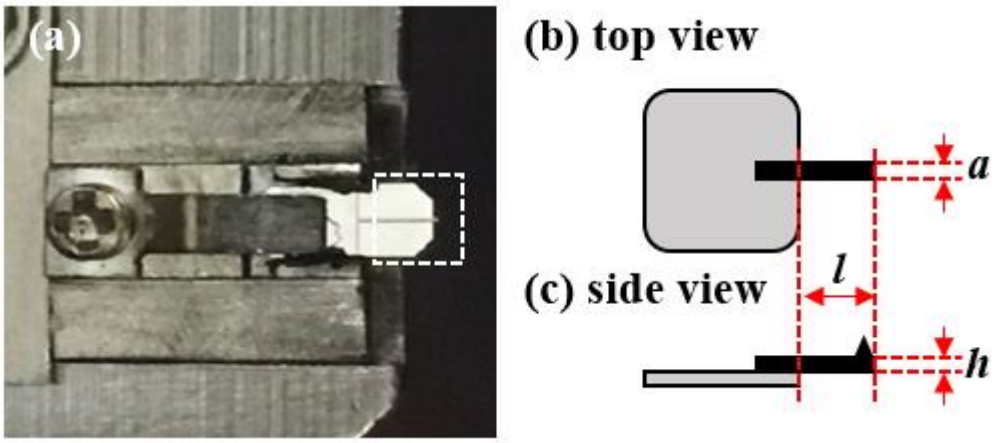

Figure 3.19 (a) Photograph of the cantilever used in our experiment. (b-c) Schematics of top and sized views of the cantilever, as indicated in (a).

- **Cantilever degassing and cleaning**

In this study, a commercially Ir-coated silicon cantilever (Nano sensors SD-T10L100, f_0 ~800kHz) was used. The cantilever is fixed to a silicon support chip, and the diameter of the tip apex is about 5~10 nm. Before surface imaging, in order to remove the oxide layer and contaminants, the tip was degassed at a temperature around 600 K for 5 min and then bombarded by Ar-ion sputtering at a pressure of 5×10^{-7} Torr for 15 min with an emission current of 22 μA and ion energy of 1 keV.

3.6 Summary

In this chapter, we briefly introduce the low temperature UHV nc-AFM system equipped with all the necessary tools for our research, including the UHV generation equipment, nc-AFM unit, block diagram of the operation circuits, sample and cantilever preparation.

Chapter 4 Research about rutile TiO_2(110)

4.1 Introduction

In this chapter, we generally introduce the past researches about rutile TiO_2(110). In section 4.2, the properties and features of rutile TiO_2(110) are briefly discussed, including its surface defects and specifically the subsurface defects, and the polaron nature. In section 4.3, we review the research about the adsorption and dissociation of oxygen species on rutile TiO_2(110) surface, and the charge states of adsorbates. In section 4.4, the investigation of the size effect and charge states of the Au nanoclusters are presented.

4.2 Rutile TiO_2(110)

4.2.1 Surface and subsurface defects on rutile TiO_2(110)-(1 × 1)

The rutile TiO_2(110)-(1×1) surface is the most widely employed plane in the photocatalytic/catalytic reactions. [1] A model of the rutile TiO_2(110)-(1×1) surface is shown in Figure 4.1. It is mainly composed by the five-fold coordinated Ti rows (Ti_{5c}, orange balls) and the bridging two-fold coordinated O rows (O_{2c}, bright balls). The introduction of the surface and interstitial defects can transform the rutile TiO_2 from an insulator to a n-type semiconductor. The surface defects including the oxygen vacancy (O_v) and hydroxyl (OH) on rutile TiO_2(110)-(1×1) surface are formed by removing the oxygen atom form the bridging two-fold coordinated oxygen rows and the dissociation of the water molecules on the five-fold coordinated Ti rows, respectively. The interstitial defects are mainly the Ti interstitial atoms (Ti_{int}) and the subsurface hydrogen

atoms (H_{sub}). The point defects are considered as the excess electron reservoirs for the catalytic reactions. It is clarified that one OH defects can provide one excess electron, and one oxygen vacancy can provide two electrons and one Ti interstitial atom can provide four excess electrons. A large amount of experimental works in combination with the theoretical calculations have been performed to investigate the morphological and electronic properties as well as the electron distribution around the point defects. [19,20]

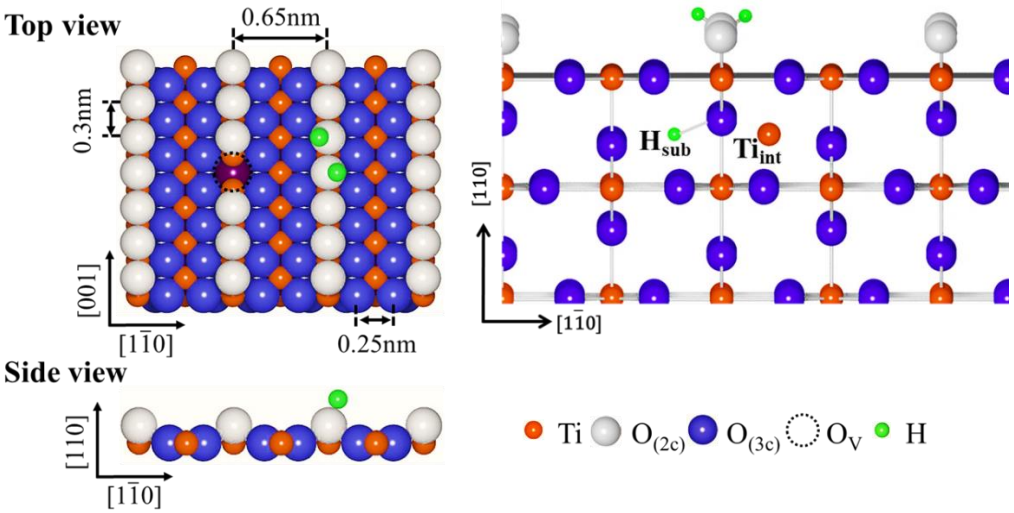

Figure 4.1 The ball model of the rutile TiO_2(110)-(1×1) surface with the surface defects and subsurface defects.

The importance of the TiO_2 surface and subsurface defects have been fully established through abundant experimental and theoretical works. For example, the electronic structure and excess electrons distribution around the surface defects have been clarified by scanning probe microscopies (SPM) at various low temperatures. [2-4] In addition, the surface defects can be diffused, [5-7] desorpted [8-9] and re-deposited at the atomic scale level in a controllable way. [10] Moreover, the surface defects, acting as the reaction intermediates and abundant surface electron donors, can also mediate the water molecules dissociation and oxygen adatoms

adsorption and dissociation on the surface. [11-13] In addition to the surface defects, the Ti interstitials in the near surface region and the subsurface oxygen vacancy in TiO_2 have been systematically investigated and demonstrated to facilitate the oxygen adsorption and enhance the electrical conductivity. [14,15]

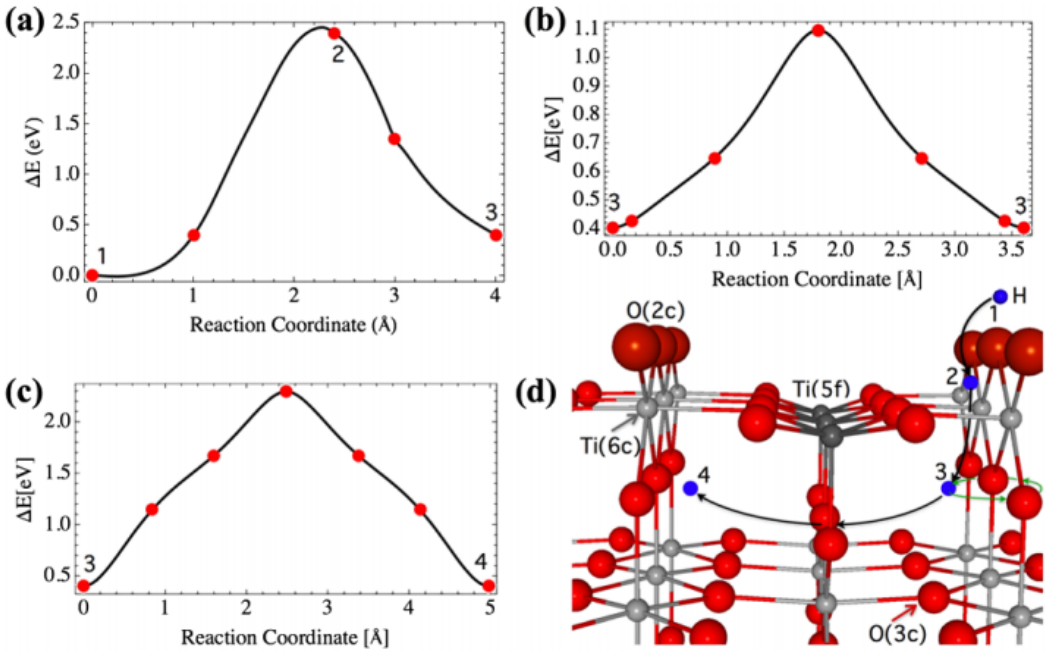

Figure 4.2 Theoretical calculation of the energy path showing the energy diagram for hydrogen movement to subsurface sites. [23]

However, subsurface hydrogen (H_{sub}), as a fundamental and predominant impurity in the near surface regions of metal and metal oxide, [16,17] is yet to be fully investigated, possibly due to the limited analytical methodologies to reveal the subsurface defects with atomic resolution. Specifically, the H_{sub} in rutile TiO_2(110) can strongly affect the local photocatalytic activity and chemical reactivity, [18] while surprisingly only few available literatures have discussed the H_{sub} to data. For example, the experimental and theoretical works have demonstrated that the adsorbed hydrogen atoms can easily diffuse into the TiO_2 bulk through a thermodynamically spontaneous

process with a low activation barrier and remain the stable H_{sub} specie in a wide temperature range. [19-21] Moreover, the residence interstitial locations of the hydrogen atoms between the surface and subsurface layers have been proposed and calculated, as shown in Figure 4.2. [2] In addition, the volumetric maps of the tip-sample interaction force of the H_{sub} have already been revealed by an interplay between simultaneous non-contact atomic force microscopy (nc-AFM) and scanning tunneling microscopy (STM) measurement in constant frequency shift mode, [23] as shown in Figure 4.3.

However, in these works, crosstalk of the topographic and tunneling current signals simultaneously recorded by nc-AFM and STM in constant frequency shift mode makes the interpretation complicated and lack of credibility. In addition, several other important information about the H_{sub} remains a largely unexplored topic, such as the local electronic properties at the single defect level and the possibility of reversible transformation between surface and subsurface layers in a controlled manner, which may have an overriding effect on revolutionizing the investigation and applications of the rutile TiO_2.

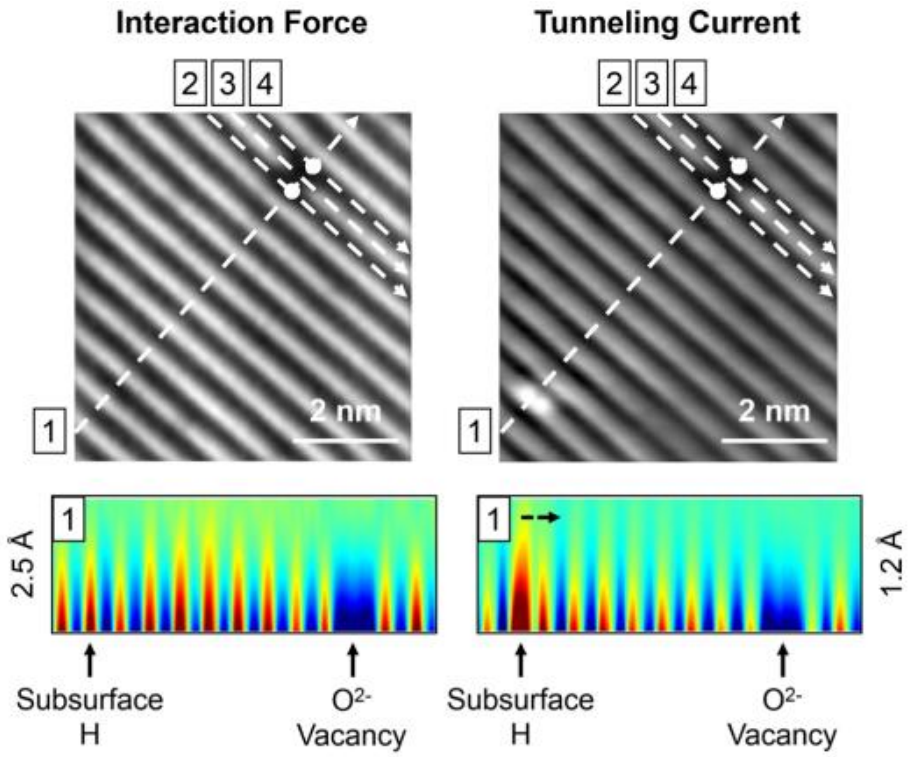

Figure 4.3 Simultaneous AFM and STM measurement of the subsurface hydrogen on rutile TiO_2(110)-(1×1) surface in constant frequency shift mode. [23]

Especially, the electron distribution around the subsurface hydrogen plays a key role in determining its electronic properties and the effects on the catalytic reactions as the electron reservoir. Some theoretical works obtained from the first principle calculations have proposed that the electron around the subsurface hydrogen is mainly localized around the nearby titanium ions in the subsurface layers., which can form polaron-like configurations, as shown in Figure 4.4. [24] However, the experimental works to demonstrate the excess electrons distribution around the subsurface hydrogen still remain an unexplored research topic, which is very important to study its electronic properties.

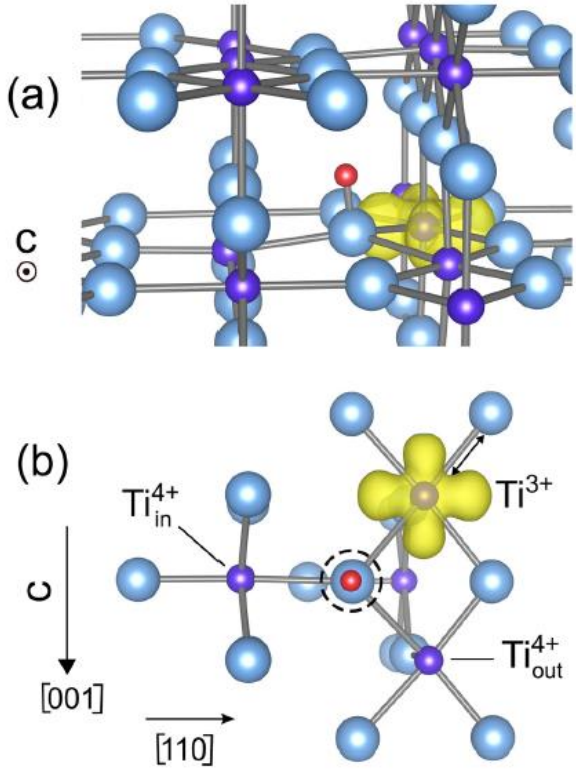

Figure 4.4 Atomistic structure of the neutral hydrogen configuration with the excess electron localized at the out-of-plane Ti ion. [24]

4.2.2 Polaron in rutile TiO_2(110)-(1 × 1)

It is well known that the rutile TiO_2(110) surface has the polaron nature due to the formation of point defects, which is quite different from the anatase TiO_2. STM studies have provided evidence that the spatial distribution of excess electrons surrounding one O_v dramatically depends on the temperature, such as a mirror symmetry in four-lobed shape at 78 K and an asymmetric distribution at 7 K, as shown in Figure 4.5. This temperature dependence of the excess electrons distribution suggests its polaronic nature. [25-27] Furthermore, an experimental study demonstrated that the configurations of the excess electrons associated with the separated O_v can be engineered by the STM tip at low temperature, leading to the redistribution of excess electrons around the O_v complex in a controlled way, indicating that the excess electrons around separated O_v can diffuse across several sites. [25] The

susceptibility of the O_v to the local environment results in a nonuniform local potential in the oxide surface, which can significantly affect the surface reactivity and adsorbates configurations.

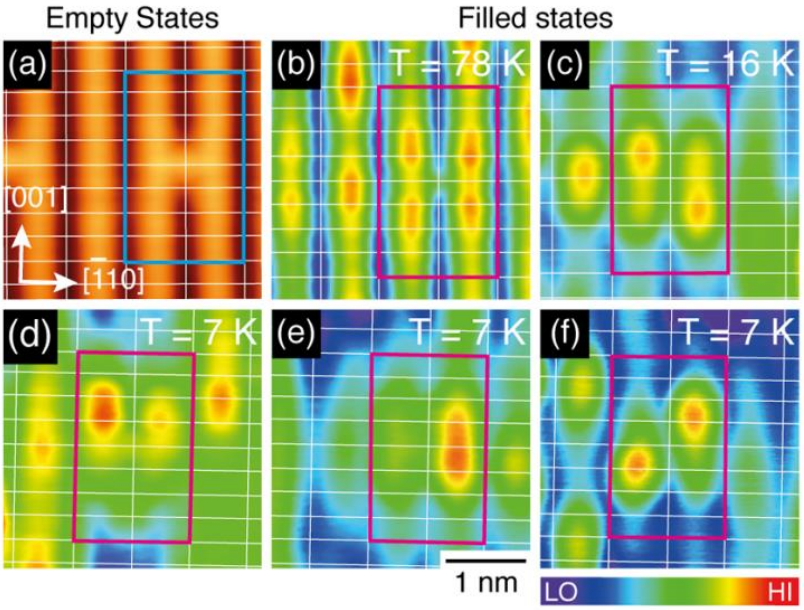

Figure 4.5 Demonstration of the polaron nature of rutile TiO_2 surface using empty and filled states STM images. [25]

4.3 Investigation of oxygen adatoms on rutile TiO_2(110)

4.3.1 Adsorption and dissociation of oxygen adatoms on rutile TiO_2(110)

The oxygen-rich rutile TiO_2(110) surface (O-TiO_2) plays a key role in the investigation of the catalytic reactions. The adsorption and dissociation behaviour of the oxygen molecules and adstoms have been investigated by a large amount of experimental and theoretical works at various low and room temperatures. At the low adsorption temperature, the oxygen molecules cannot dissociate into oxygen adatoms and keep in the form of molecules due to the large

dissociation energy barriers. With the assistance of the oxygen vacancy, the hopping of the oxygen molecules has been experimentally characterized on the rutile TiO_2(110) surface by the time-resolved scanning tunnelling microscopy, and it is demonstrated that the density of the oxygen vacancy strictly determines the hooping rate of the oxygen molecules. [28] In addition, the adsorbed oxygen molecules on the rutile TiO_2(110) surface at low temperatures can be dissociated into the oxygen adatoms by the tunnelling electrons from the tip. [29] At the room temperature, a large amount of experimental works in combination with the theoretical calculations have been performed to demonstrate that the oxygen molecules can spontaneously dissociate into oxygen adatoms, and it is proposed that the excess electrons are provided by the point defects including the surface and interstitial defects. [30,31] Moreover, two dissociation channels of the oxygen adatoms have been proposed recently, namely, 1) the oxygen vacancy-assisted dissociation and 2) the direct dissociation on Ti_{5c} rows, as schematically shown in Figure 4.6. In the 1st dissociation channel, it is proposed that the excess electrons for oxygen dissociation is mainly provided by the oxygen vacancies, and one oxygen adatom can heal the nearby oxygen vacancy and another single oxygen adatom is located on the Ti_{5c} row. In the 2nd dissociation channel, the double oxygen adatoms is paralleled arranged along the Ti_{5c} rows and can spontaneously dissociate from the nearest adhesion state to two separated single adatoms. The dissociation energy barrier as a function of the dissociation distance is presented in Figure 4.7. In this dissociation behaviour, the excess electrons are proposed from the interstitial defects, such as the Ti_{int}.

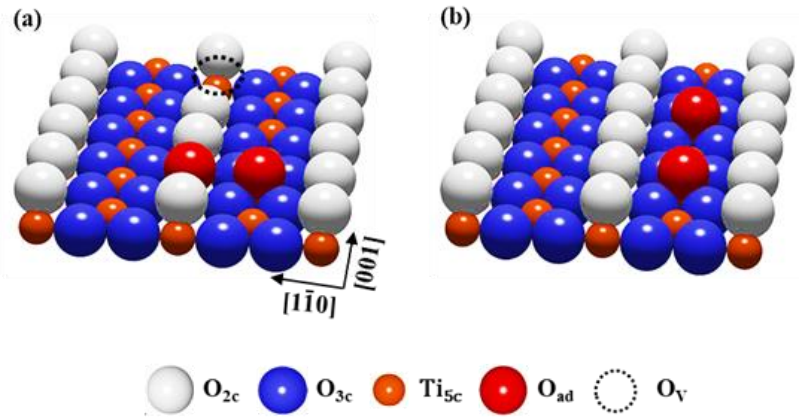

Figure 4.6 Ball model of the dissociation channels of the oxygen adatoms on rutile TiO_2(110)-(1 × 1) surface, (a) the oxygen vacancy-assisted dissociation, (b) directly adsorption on Ti_{5c}.

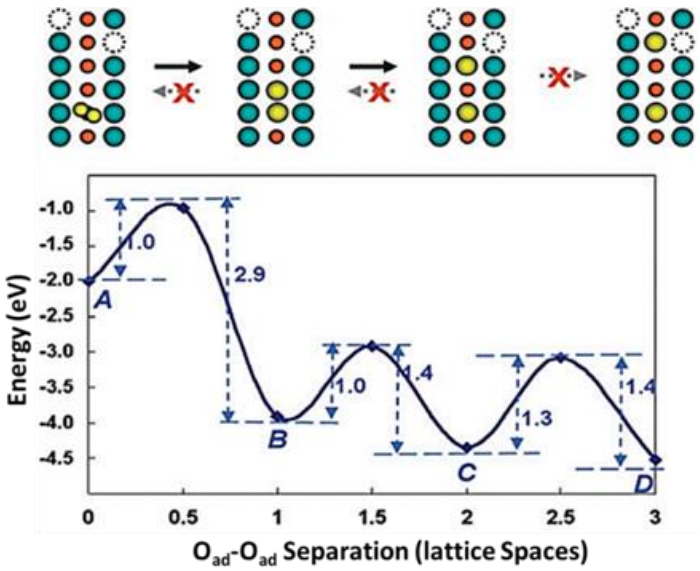

Figure 4.7 Energy barriers for the oxygen adatom dissociation and diffusion on the Ti_{5c} rows as a function of separation lattices. [30]

4.3.2 Charge state of oxygen molecules

Usually the adsorbed oxygen enters the catalytic reaction in a form of a single oxygen adatom (O_{ad}), [25-30] and the activation of the adsorbed O_{ad} is a key factor toward the catalytic reactions, which considerably depends on its charge state. Up to now, some theoretical calculations are

performed to investigate the charge state of adsorbed oxygen molecules, and it has been clearly identified and assigned to neutral O_2, charged $(O_2)^-$ and $(O_2)^{2-}$, [32,33] as shown in Figure 4.8. In addition, the charge state transition of the adsorbed oxygen molecules between O_2 and $(O_2)^-$ has been demonstrated with a combination of nc-AFM and STM on anatase TiO_2 surface. [34] However, despite its importance to catalytic reactions, the possible charge states of adsorbed O_{ad} on rutile TiO_2(110) has been studied to much lesser extent, both experimentally and theoretically.

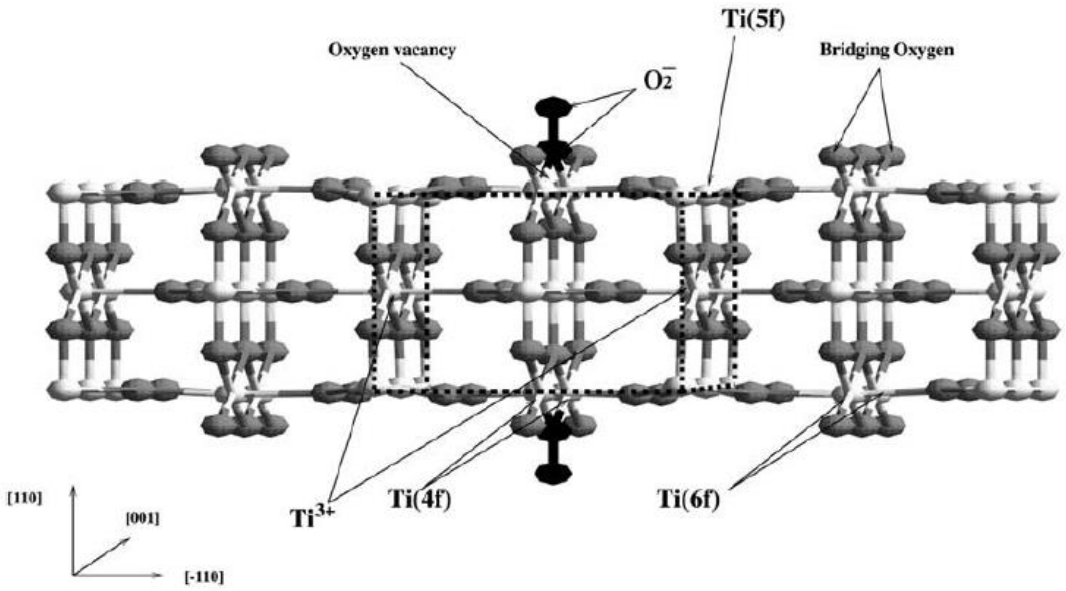

Figure 4.8 Ball model of the dissociation channels of the oxygen adatoms on rutile TiO_2(110)-(1 × 1) surface, (a) the oxygen vacancy-assisted dissociation, (b) directly adsorption on Ti_{5c}. [33]

4.4 Charge state of Au nanoclusters on rutile TiO_2(110)

The distinctive catalytic properties of the dispersed noble metal nanoparticles supported on reducible oxide surface, since the first introduction by Haruta and coworkers, [35,36] have

stimulated enormous experimental and theoretical research interest with the aim of elucidating the catalytic mechanism of this remarkable catalysis. [37-41] Among them, the gold nanoparticles (Au NPs) supported on rutile TiO_2(110) surface are demonstrated as the prototypical heterogeneous catalyst, and have been widely employed in various technological applications because of its high catalytic activity, such as the reduction and oxidation reactions at low temperatures. [42-44] In this regard, extensive studies have been devoted to unveil the key factors responsible for this high catalytic activity and the chemical nature of this catalysis. However, up to now, it is still in intense debate about the dominant factors with few consensuses reached, and the catalytic mechanism of the Au/TiO_2 system has not been fully understood yet, both experimentally and theoretically.

4.4.1 Au nanocluster size effect on catalytic activity

In the Au/O-TiO_2 catalytic system, the morphological and electronic properties of the Au nanoclusters can significantly affect the catalytic activity, such as the size, adsorption site and charge state. In general, it is proposed that the unique catalytic activity of the Au NPs can be dramatically affected by several key factors, which can be roughly categorized into the geometric [45,46] and electronic [51,52] properties of the Au NPs. In details, from a geometric point of view of the Au NPs, the fraction of the active under-coordinated Au atoms is demonstrated to be the governing factors for the high catalytic activity, which strongly depends on the nucleation dynamics, [45,46] size [47] and geometric structures [48-50] of the Au NPs. It is experimentally demonstrated that the size of the Au nanoclusters can exclusively determine the catalytic activity of the catalyst, and it is clarified that the Au nanoclusters with the size of about 2~4 nm show the high catalytic activity for the oxidation reactions, which is presented in Figure 4.9. [49] In addition, the active catalytic site is believed to be the perimeter of the Au/TiO_2 interface, as clarified by the

theoretical calculation in combination with spectroscopic observations. [53-56] Besides that, the dynamic structural fluxionality of the supported Au NPs has been proposed by some theoretical works recently, and it suggests that the coexisting structural configurations of the Au NPs may be formed in an equilibrium state with different chemical activities, which could potentially allow the catalytic reactions to evolve on the most favorable free-energy path. [57-58] While few experimental works have ever discussed and demonstrated such dynamic structure fluxionality, which is possibly due to the strong dependence of the adhesion properties of the Au NPs on the oxides substrate conditions.

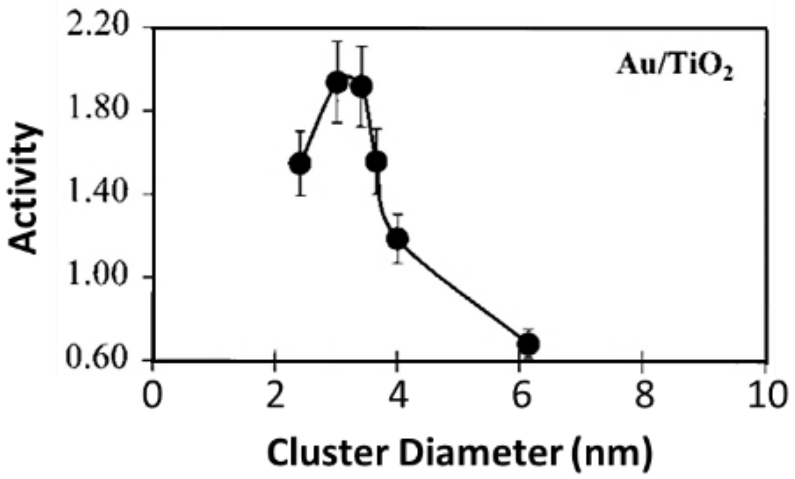

Fig. 4.9 Activity of the Au nanoclusters as a function of the cluster diameter. [49]

4.4.2 Charge state of Au nanocluster

The charge state of the Au NPs and the charge transfer between oxide supports and Au NPs, from an electronic point of view, also play a key role in understanding and controlling the catalytic reactions. [51-53] In this respect, both experimental and theoretical works have demonstrated that, on reduced and hydrated rutile TiO_2 surface, the Au NPs are negatively charged due to the charge transfer from the substrate to Au NPs. [59,60] It is theoretically proposed that the charge states of

the Au nanoclusters are dynamically changed depending on the chemical environment during the catalytic reactions, as shown in Figure 4.10. The Au nanoclusters are always negatively charged in the reducing environment and act as the electron reservoirs for the catalytic reaction. While it is transformed to be positively charged in the presence of oxidizing species, which is due to the charge transfer between the substrate and Au nanoclusters. However, the clear clarification of the charge state of the Au NPs on oxygen-rich rutile TiO_2 surface (O-TiO_2) still remains an unexplored research topic, which calls for convincing experimental works to clarify the charge transfer direction and understand the catalytic mechanism.

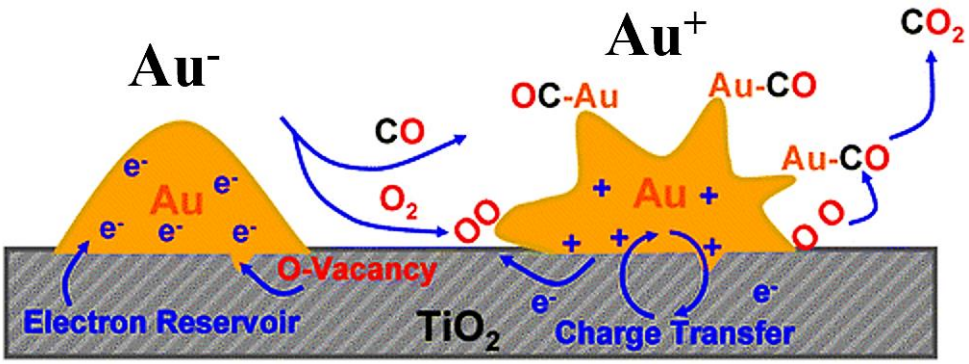

Figure 4.10 Schematic of the dynamic charge states of the Au nanocluster during the catalytic process. [38]

4.5 Summary

In this chapter, we briefly introduced the past researches on rutile TiO_2(110) surface by AFM and STM, including the geometric and electric properties of the point defects (especially the subsurface defects), investigation of oxygen adatoms on rutile TiO_2(110) and the charge states of Au nanoclusters. Specifically, the problems in the research on rutile TiO_2(110) surface are pointed out in details.

Chapter 5 Investigation of subsurface defect on rutile TiO_2(110) by nc-AFM /KPFM

The following chapter is based on the publication:

Zhang, Q., Wen, H. F., Adachi, Y., Miyazaki, M., Sugawara, Y., Xu, R., Cheng, Z. H. and Li, Y. J., Characterization and Reversible Migration of Subsurface Hydrogen on Rutile TiO_2 (110) by Atomic Force Microscopy at 78 K.

The Journal of Physical Chemistry C, *123*, 22595-22602, 2019.

5.1 Introduction

In this chapter, we introduce the systematic investigation of the subsurface defect on rutile TiO_2(110)-(1×1) surface using the multi-channel SPM technique including the simultaneous nc-AFM/STM and nc-AFM/KPFM measurement in constant height mode at 78 K. Here, we propose that, due to the highly localized configuration and reversible migration behavior, the subsurface defect is most possible to be the subsurface hydrogen atoms (H_{sub}). We find that four different configurations of the H_{sub} are clearly characterized and distinguished by nc-AFM/STM measurement. In particular, the V_{LCPD} of the subsurface hydrogen is mapped by KPFM with atomic resolution for the first time. Besides the capability of characterizing the H_{sub} by nc-AFM/STM/KPFM, we also demonstrate that the H_{sub} can be reversibly migrated between the surface and subsurface layers. The movement direction of the H_{sub}, such as upward or downward migration, can be strictly determined by controlling the polarities of the voltage pulse, and the

manipulation mechanism is tentatively attributed to the inelastic electron tunneling effect and local electric field.

5.2 Methods

Simultaneous measurements of the frequency shift Δf and time-averaged tunneling current $\langle I_t \rangle$ signals were performed using the dual-channel nc-AFM and STM approach in constant height mode to avoid the crosstalk between Δf and $\langle I_t \rangle$ signals. [1] The DC bias voltage was applied to the sample, and the $\langle I_t \rangle$ signal was detected from the tip. The frequency modulation KPFM, based on nc-AFM with bias voltage feedback, was used to measure the Δf and V_{LCPD} images simultaneously.[2] As a sensor, an Ir-coated Si cantilever (Nanosensors SD-T10L100, spring constant k = 1500 N/m, quality factor Q = 24500, resonant frequency f_0= 800 kHz) was oscillated with a constant oscillation amplitude (500 pm). All the images in this work were measured in constant height mode, and the atom tracking technique was used to compensate the thermal drift.

5.3 Results and discussion

5.3.1 Characterization of subsurface hydrogen by AFM/STM/KPFM

Figure 5.1 shows four sets of frequency shift ($|\Delta f|$) and time-averaged tunneling current ($|\langle I_t \rangle|$) images of the rutile TiO_2(110)-(1 × 1) surface measured by nc-AFM and STM simultaneously in constant height mode at 78 K. Here, in the nc-AFM ($|\Delta f|$) images, the bright and dark rows correspond to the alternating 2-fold coordinated bridge oxygen rows (O_{2c}) and the 5-fold coordinated titanium rows (Ti_{5c}), respectively. Inversely, in the corresponding STM ($|\langle I_t \rangle|$) images, the bright and dark rows correspond to the Ti_{5c} and O_{2c}, respectively, due to the dominated electronic effects. [3] In Figure 5.1, the surface defects are recorded as dark holes in the nc-AFM images (hole mode) and as bright spots in STM images, respectively. Besides that, some extra

bright spots can be clearly distinguished on the O_{2c} rows in the STM images, while imperceptible in the corresponding nc-AFM images, as the dashed blue circles indicated in Figure 5.1. It suggests that these specific species are not on the topmost surface layer, and the tip-sample interaction force is completely screened in nc-AFM measurement. Here we stress that the experimental challenge exists in directly identifying the subsurface species by STM measurement, and we presume that, based on the following discussed experimental results, these highly localized bright extra spots are most possible to be the subsurface hydrogen atoms (H_{sub}) in the subsurface layer of rutile TiO_2(110).

In our study, four different configurations of the H_{sub} are clearly characterized and distinguished, including the H_{sub} monomer in Figure 5.1 (b), the dimer in Figure 5.1 (e), the trimer in Figure 5.1 (h) and the tetramer in Figure 5.1 (k). Specifically, we note that the characterization of H_{sub} is independent of the tip apex polarity. In addition, the H_{sub} species show various intensity of brightness even with the same configuration, such as in Figures 5.1(e) and 5.1(k), and here the contrast difference is tentatively attributed to the H_{sub} lying at different subsurface layers, as the STM can detect the electronic signal up to several atomic layers beneath the surface. [4] We speculate that these H_{sub} species are formed due to surface hydrogen atoms migration during sample preparation. Some experimental works in combination with theoretical calculations have demonstrated that the surface hydrogen atoms can easily migrate into the bulk with a rather low energy barrier when increasing the temperature, [5-7] and the H_{sub} can remain a more stable subsurface specie than in the under-coordinated sites on the surface, due to the formation of hydrogen bond with other atoms inside the cavity. [7] Note that, among these H_{sub} configurations, the H_{sub} dimer is found to be the most dominant specie, which is in good agreement with previous work. [8] In this work, we note that the H_{sub} with four kinds of configurations has long lifetime to be characterized for several hours and no spontaneous configuration change can be observed

during characterization even with decreased tip-sample distance, which is perfectly consistent with the theoretical calculation. [7] Particularly, the employment of constant height scanning approach in this study completely avoids the crosstalk between the electrostatic force and tunneling current channels induced by the active feedback, which can provide more accurate physical information of the local geometric and electronic properties of the H_{sub} compared to previous works. [8,9] Our experimental measurement systematically reveals four different configurations of the H_{sub}, and demonstrates the unprecedented capability of the dual-channel nc-AFM/STM characterization approach for the subsurface defects.

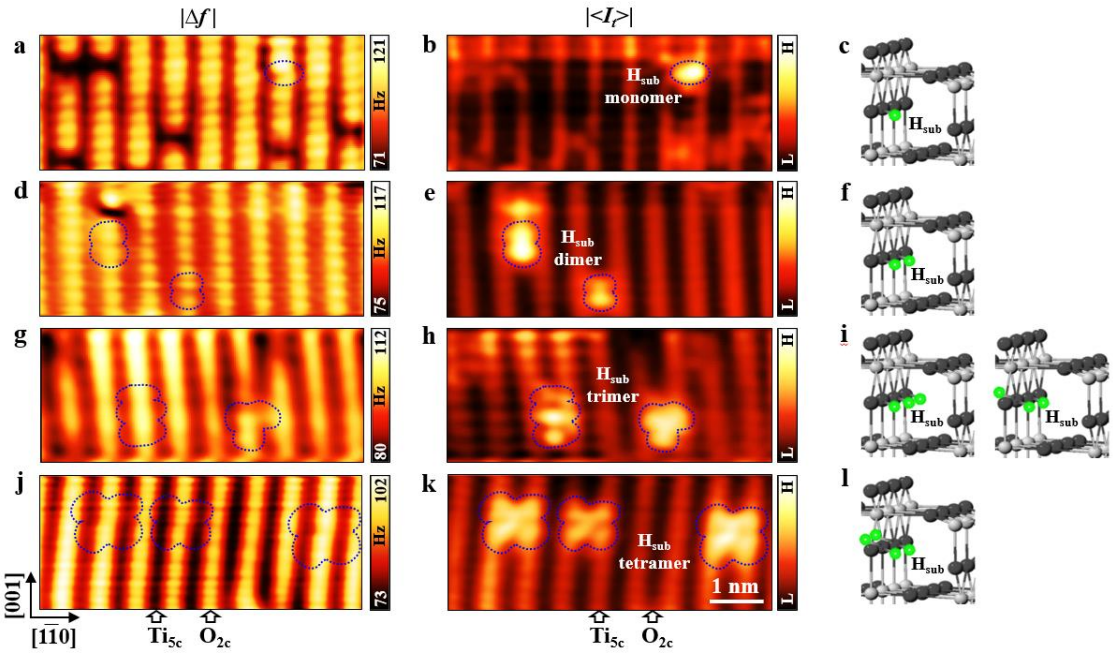

Figure 5.1 Characterization of the subsurface hydrogen (H_{sub}) on rutile TiO_2(110)-(1 × 1) by nc-AFM and STM simultaneously in constant height mode. (a, b), (d, e), (g, h), (j, k), Four sets of simultaneously measured frequency shift $|\Delta f|$ (nc-AFM, hole mode, 2.5 × 6 nm^2) and time-averaged tunneling current $|\langle I_t \rangle|$ (STM, empty state, 2.5 × 6 nm^2) images of rutile TiO_2(110)-(1 × 1) surface, respectively. (c, f, i, l) Corresponding schematic models of the H_{sub} with different configurations. The dashed blue circles indicate the H_{sub} monomer in (b), dimer in (e), trimer in

(h) and tetramer in (k), respectively. O_{2c}: 2-fold coordinated bridging oxygen row. Ti_{5c}: 5-fold coordinated titanium row. Imaging parameters: f_0 = 813 kHz, A = 500 pm, Q = 24500, T = 78 K, V = + 0.8 V.

We now focus on the investigation of the electronic property of the H_{sub} using the multi-channel nc-AFM/STM and nc-AFM/KPFM measurement approach in constant height mode. Figure 5.2 (a, b) show the simultaneous nc-AFM and STM images of the H_{sub} tetramer on rutile TiO_2(110)-(1 × 1) measured in constant height mode. It is clearly observed in the STM image that the H_{sub} tetramer resides on the O_{2c} row with bright contrast, which is in perfect agreement with the experimental results in Figure 5.1. We note that the nc-AFM image in Figure 5.2 (a) is in the protrusion mode now, which indicates that the characterization of H_{sub} is independent of the tip polarity. Also, the H_{sub} tetramer can be slightly observed in the nc-AFM image in Figure 5.2(a), which is possibly due to the smaller tip-sample distance. After the simultaneous nc-AFM and STM characterization of the H_{sub} tetramer, the KPFM with bias voltage feedback measurement is performed to characterize the same area, as shown in Figure 5.2(c). Interestingly, in the KPFM image of H_{sub} tetramer, the dumbbell-like feature is observed rather than the tetramer configuration. We stress here it is first time to obtain the local contact potential difference (V_{LCPD}) image of the subsurface defects with atomic resolution. Since it has been demonstrated that the V_{LCPD} image reflects the charge distribution of the atoms, we tentatively propose here that the bright contrast of the H_{sub} in the V_{LCPD} image may possibly indicates the charge distribution of the H_{sub}. The dumbbell-like feature is mainly located on the O_{2c} rows, as shown in Figure 5.2(c), and we propose that the charge around the H_{sub} tetramer is mainly localized around the nearby Ti atoms, as the yellow circles indicated in Figure 5.2(e), which is consistent with previous

theoretical work. [11] We suggest that further theoretical calculation is necessary to verify our proposition about the charge distribution of the H_{sub}.

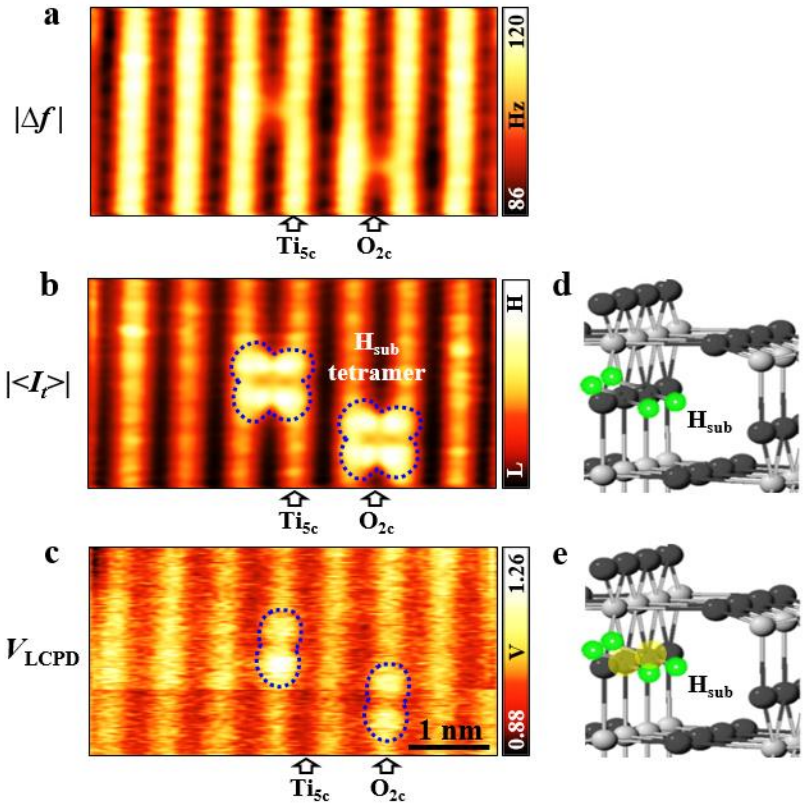

Figure 5.2 Characterization of the H_{sub} tetramer by nc-AFM/STM/KPFM measurement of the same area in constant height mode. (a, b) Simultaneously measured $|\Delta f|$ (protrusion mode, 2.5 × 5 nm^2) and $|<I_t>|$ (empty state, 2.5 × 5 nm^2) images of rutile TiO_2(110)-(1 × 1) surface. (c) Corresponding experimental V_{LCPD} images on the same area as shown in (a, b), respectively. (d, e) The corresponding schematics of H_{sub} configuration and charge distribution. Imaging parameters: f_0 = 813 kHz, A = 500 pm, Q = 24500, T = 78 K, V = + 0.8 V.

Moreover, we perform the identical multi-channel measurement on the H_{sub} dimer, as shown in Figure 5.3. As shown in Figure 5.3, the H_{sub} dimer is characterized by dual-channel nc-AFM/STM

and nc-AFM/KPFM with bias voltage feedback in constant height mode. In V_{LCPD} image, the H_{sub} dimer can be clearly characterized as the dumbbell-like feature on the O_{2c} row.

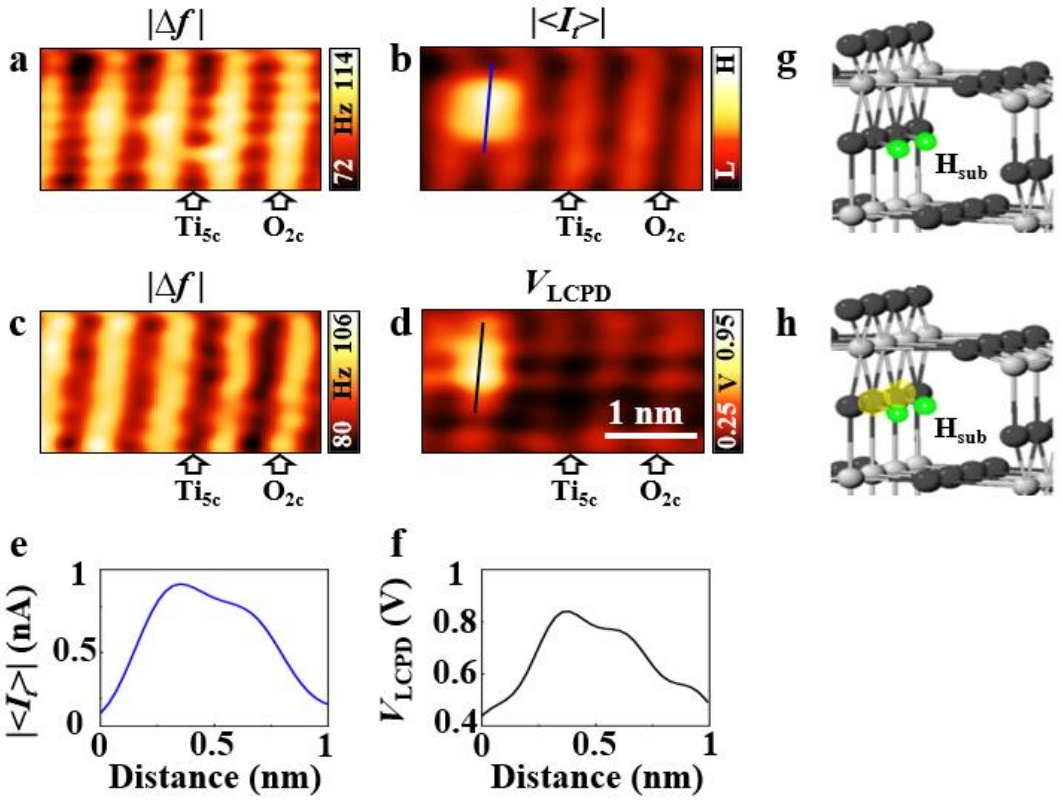

Figure 5.3 Characterization of the H_{sub} dimer by nc-AFM/STM/KPFM measurement of the same area in constant height mode. (a, b) Simultaneously measured $|\Delta f|$ (hole mode, 1.5 × 3 nm^2) and $|<I_t>|$ (empty state, 1.5 × 3 nm^2) images of rutile TiO_2(110)-(1 × 1) surface. (c, d) Corresponding experimental $|\Delta f|$ and V_{LCPD} images of the same area as shown in (a, b), respectively. (e, f) Line profiles of $|<I_t>|$ and V_{LCPD} of the H_{sub} dimer as the blue and dark lines indicated in (b) and (d), respectively. (g, h) The schematic models of H_{sub} dimer and its corresponding charge distribution. Imaging parameters: f_0 = 813 kHz, A = 500 pm, Q = 24500, T = 78 K, V = + 0.8 V.

Quantitatively, the V_{LCPD} measurement can be affected by many external factors, such as the tip apex and tip-sample distance. In order to obtain more comprehensive information, we record the

V_{LCPD} of the same H_{sub} dimer (in Figure 5.3) as a function of the tip-sample distance, as shown in Figure 5.4, ensuring no tip termination change. We can observe that, with decreased tip-sample distance, the contrast of the H_{sub} dimer in V_{LCPD} images is gradually enhanced with stable dumbbell-like feature. It is pointed that KPFM can enable the direct measurement of V_{LCPD} at the atomic level, [10] and here we tentatively propose that the dumbbell-like feature in the V_{LCPD} images possibly indicates the localized charge distribution around the nearby Ti atoms. Our experimental result is consistent with the past theoretical calculation of the charge distribution of H_{sub}. [11] We note that further theoretical calculation such as density functional theory (DFT) is necessary to verify that if the local potential measurement by KPFM can reflect the charge distribution of the H_{sub} species.

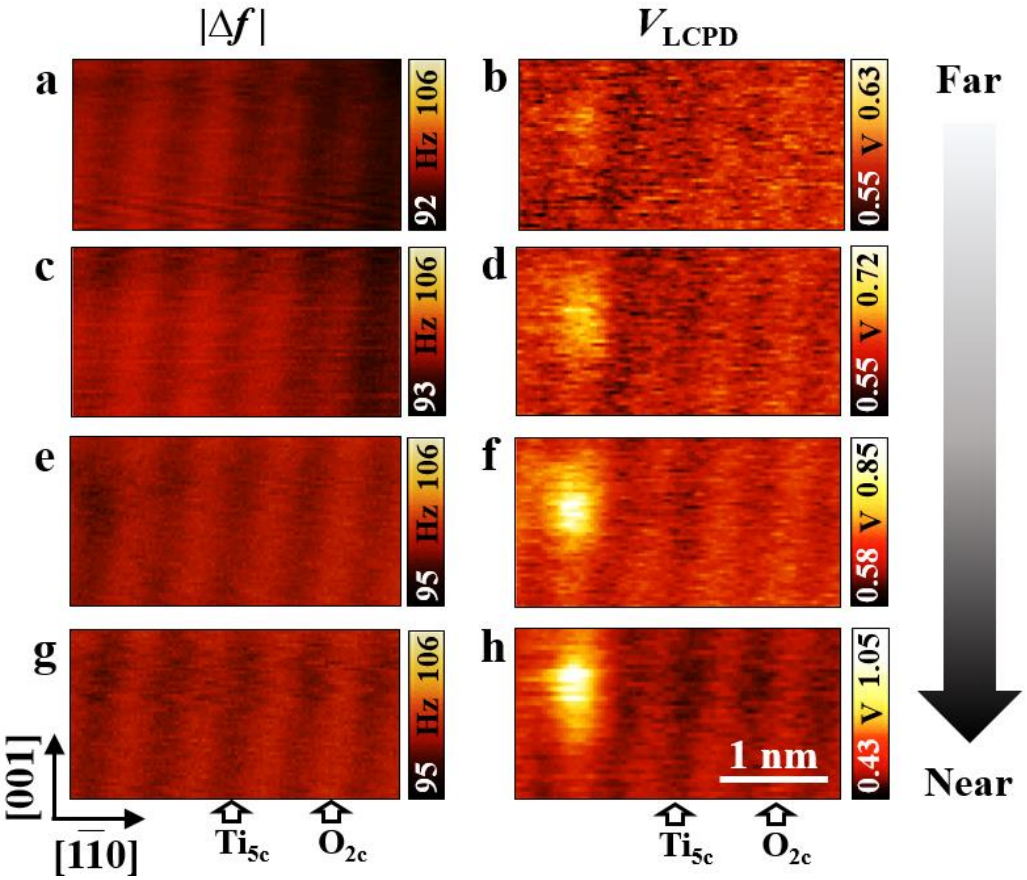

Figure 5.4 Constant-height $|\Delta f|$ (hole mode) (a) (c) (e) (g) and corresponding V_{LCPD} (b) (d) (f) (h) images (1.5 × 3 nm^2) of the same areas on rutile TiO_2(110)-(1 × 1) surface simultaneously measured, respectively. Every set of $|\Delta f|$ and corresponding V_{LCPD} images of the dimer subsurface H_{sub} are recorded after approaching the tip 20 pm near to the sample. Imaging parameters: f_0 = 813 kHz, A = 500 pm, Q = 24500, T = 78 K.

5.3.2 Reversible migration of subsurface hydrogen by AFM

The local geometric configuration and electronic property of the H_{sub} on rutile TiO_2(110)-(1 × 1) have been systematically investigated and clearly clarified using the multi-channel SPM measurement methodology in our study. Now, we extent our capability to deliberately manipulate the H_{sub} by the SPM tip in a controllable manner.

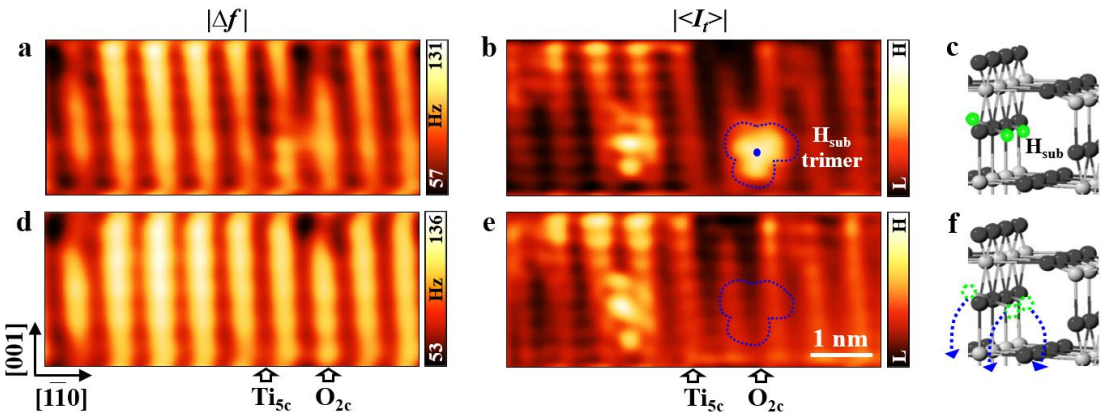

Figure 5.5 Downward migration of the H_{sub} trimer between subsurface layers. (a, b) Simultaneously recorded $|\Delta f|$ (hole mode, 2.5 × 6 nm^2) and $|<I_t>|$ (empty state, 2.5 × 6 nm^2) images of rutile TiO_2(110)-(1×1) surface in constant height mode, respectively. (d, e) Corresponding $|\Delta f|$ (hole mode) and $|<I_t>|$ (empty state) images of the same area as shown in (a, b) after the positive voltage pulse. (c, f) The schematic models of the H_{sub} trimer downward

migration process. Blue dot in (b) means the positive voltage pulse site. Imaging parameters: f_0 = 813 kHz, A = 500 pm, Q = 24500, T = 78 K, V = + 0.8 V.

Figure 5.5 shows the downward migration of the H_{sub} trimer between subsurface layers activated by the positive voltage pulse. In Figure 5.5 (b), the H_{sub} trimer is clearly recorded in the STM image, as indicated by the blue dashed circle. Then, the tip is positioned precisely above the center of the H_{sub} trimer (blue dot in Figure 5.5(b)) and the feedback loop is interrupted. We try the positive voltage pulse from 1 V, which is slightly beyond the scanning bias voltage (0.8 V), and gradually increase the voltage until successive migration event is observed. After each voltage pulse with a duration of up to 10 s, the same area is characterized to check if any migration is triggered. In this experiment, we notice that the H_{sub} trimer completely disappear in the STM image when a 2.5 V voltage pulse is applied, as shown in Figure 5.5 (e). Here we speculate that the H_{sub} trimer migrate into the deeper subsurface layers, which exceeds the detecting limitation of the STM, as shown in Figure 5.5 (f). We suggest the underlying migration mechanism of the surface and subsurface hydrogen atom is tentatively explained by the injection of inelastic electrons tunneling effect (IET) accompanied with the strong local electric field in the tunneling junction. During the positive voltage pulse, the SPM tip acts as the electron source with high local electron density and injects a small fraction of the inelastic tunneling electrons into the H_{sub}. The inelastic tunneling electrons can transfer energy from the tip to H_{sub}. Meanwhile, the strong local electric field can be automatically formed accompanied with tunneling electrons injection, which is confined between the tip apex and the target H_{sub}. With the combined effect of IET and local electric field during the positive voltage pulse, the H_{sub} trimer can be activated to migrate into the deeper subsurface layers, which is speculated to be a new energetically favorable state. Our work

demonstrates that the IET accompanied with local electric field effect offers an efficient approach for the manipulation and migration of the subsurface defects.

Inspired by the one-orientation migration (downward migration) of the surface and subsurface hydrogen activated by the positive voltage pulse, now we try to explore a more complicated migration process of the H_{sub}, namely, a reversible migration between subsurface and surface hydrogen by switching the polarities of the voltage pulse. as shown in Figure 5.6.

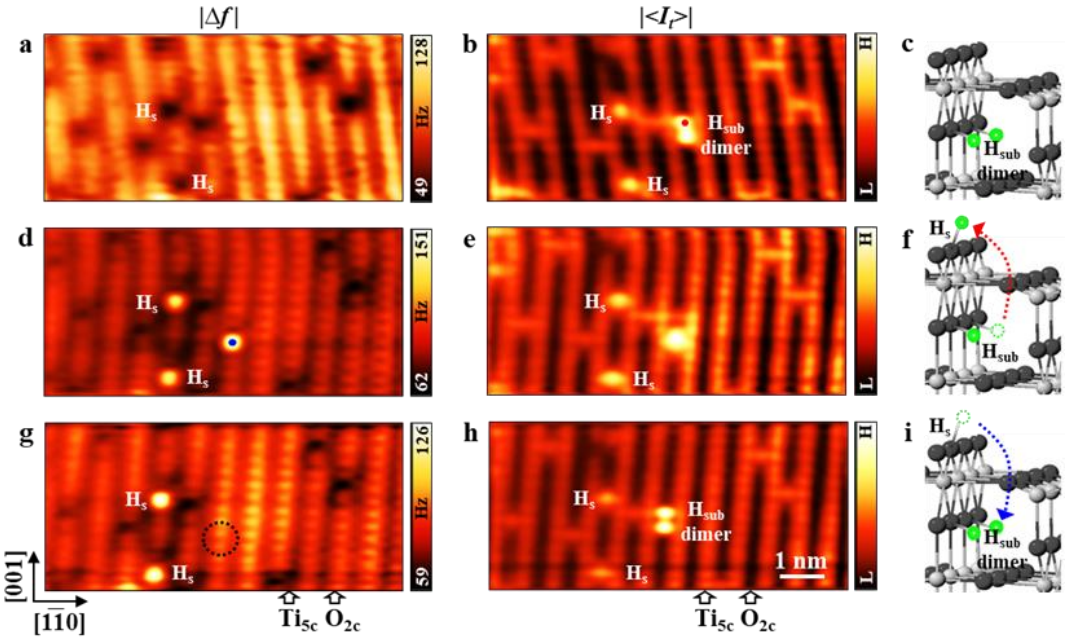

Figure 5.6 Reversible migration of the H_{sub} between subsurface and surface layers by switching the polarities of the voltage pulse. (a, b) Simultaneously measured $|\Delta f|$ (hole mode , 4 × 8 nm^2) and $|<I_t>|$ (empty state, 4 × 8 nm^2) images of rutile TiO_2(110)-(1×1) surface in constant height mode. (d, e) Simultaneous $|\Delta f|$ (natural mode) and $|<I_t>|$ images (empty state) of the same area as shown in (a, b) after the negative voltage pulse. (g, h) Simultaneously recorded $|\Delta f|$ (natural mode) and $|<I_t>|$ (empty state) images of the same area as shown in (d, e) after the positive voltage pulse. (c, f, i) Corresponding schematic models of the reversible switching of the H_{sub}. Red and blue dots in (b) and (d) indicate the negative and positive voltage pulse sites, respectively. H_s:

surface hydrogen atom. Imaging parameters: f_0 = 813 kHz, A = 500 pm, Q = 24500, T = 78 K, V = + 0.8 V.

Here we demonstrate that the H_{sub} can be upward transformed from subsurface to surface layers by the negative voltage pulse (in Figure 5.6(a-f)), and downward migrated from surface to subsurface layers activated by the positive voltage pulse (in Figure 5.8(d-i)). More specifically, as shown in Figure 5.6(a) and 5.6(b), the surface defects, including OH and O_v, are characterized as dark holes in nc-AFM image (hole mode) and as bright spots in STM image. We note that, depending on the contrast in STM image, the two brighter spots of the surface defects in Figure 5.6(b) can be clearly distinguished as OH (surface hydrogen H_s) and others as oxygen vacancy (O_v). One H_{sub} dimer can be clearly observed with brightest contrast in Figure 5.6(b), as the model presented in Figure 5.6(c). As the H_{sub} can downward migrate to the deeper subsurface layers activated by the positive voltage pulse as demonstrated in Figure 5.5, now the negative voltage pulse is employed to transform the H_{sub} from the subsurface to the topmost surface layer. As the red dot indicated in Figure 5.6(b), a voltage pulse of -3.5 V with a duration of 10 s is applied precisely above the upper H_{sub}. The tunneling current is monitored as a function of time during the pulse, as shown in Figure 5.7(b). A sudden jump in current trace is observed after some time, which is indicative of the successful upward migration of the H_{sub} from the subsurface to the surface layer, as schematic model shown in Figure 5.6(f). [12] After that, the same area is characterized again without changing any scanning parameters. Note that the nc-AFM image in Figure 5.6(d) changes to neutral mode now, and, besides the two surface hydrogen (H_s), one additional bright spot on the O_{2c} row is clearly observed on the right side of the nc-AFM image, and only one brighter spot is left in the original H_{sub} dimer position as shown in Figure 5.6(e). We notice that the bright spot on the right side of the nc-AFM image in Figure 5.6(d) shows quite

similar configuration with the left H_s. Hence, we strongly propose that the right bright spot in Figure 5.6(d) is one hydrogen atom lying on the O_{2c} row, which is upward migrated from the subsurface H_{sub} dimer. In addition, the fresh surface hydrogen atom is speculated to be precisely located above the left H_{sub}, resulting the brighter contrast in nc-AFM and STM images, as clearly presented in Figure 5.6(d).

The upward migration of the H_{sub} is demonstrated for the first time in the experiment, and we propose here that the manipulation mechanism of the migration is tentatively attributed to the injection of inelastic tunneling electrons from the polaron in substrate [13] and the local electric field automatically formed in the tunneling junction. After the upward migration process, a positive voltage pulse with magnitude of 2 V is applied on the fresh surface hydrogen atom to activate the downward migration, as the blue dot indicated in Figure 5.6 (d). The tunneling current signal is monitored (shown in Figure 5.7 (c)), and a sudden jump is observed in tunneling current trace after some time, which indicates the downward migration of the surface hydrogen atom (Figure 5.6 (i)). After that, the same area is characterized again without changing any scanning parameters. The surface hydrogen atom disappears from the nc-AFM image (Figure 5.6 (g)), and the H_{sub} dimer is reformed as shown in Figure 5.6 (h). The reversible migration process of the H_{sub} between surface and subsurface layers has been successfully demonstrated for the first time. In addition, we clearly stress here that it needs higher bias voltage to induce upward migration than that inducing downward migration, which indicates the higher energy barrier for the upward migration process than the downward migration. Our experimental results are in perfect agreement with the previous theoretical calculations.[35] Note that, , the surface hydrogen atom can be downward migrated rather than desorbed in this experiment. [14] Here, we speculate that the strong tip-induced electric field confined between the AFM tip and sample surface can compel the surface hydrogen to preferably downward migration rather than desorption. Based on our

experimental results, we tentatively propose that the mechanism of the reversible downward and upward migration of the hydrogen atoms is primarily attributed to the injection of the inelastic tunneling electrons from the tip or from the polaron in the substrate to the target H_{sub} during the positive and negative voltage pulse, respectively. Meanwhile, the direction of the tip-induced local electric field can be can be deliberately controlled by changing the polarities of the voltage pulse. As a result of the combined IET and local electric field effects, the H_{sub} can be delibratedly migrated between the energetically favorable states in a controllable and reversible manner.

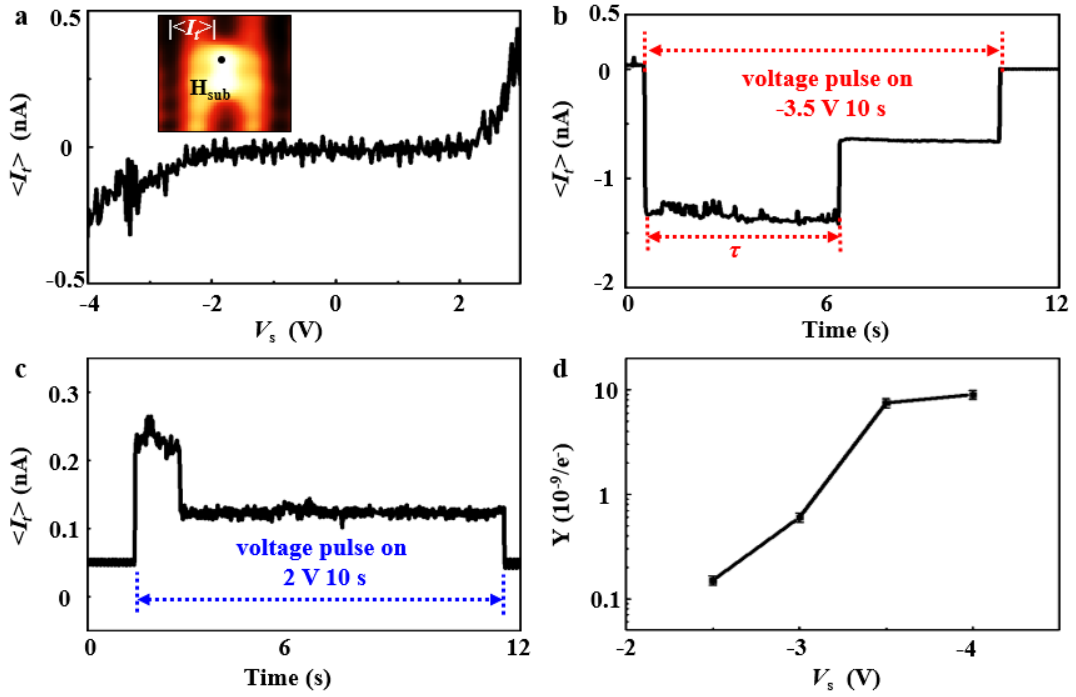

Figure 5.7 Statistical analysis of the H_{sub} and the voltage pulse effect. (a) *I-V* spectrum measured on top of the H_{sub} as indicated in the inset STM image. The black dot in (a) means the tip position during the spectrum. (b) and (c) Tunneling current $<I_t>$ recorded as a function of time during the negative and positive voltage pulse on subsurface and surface hydrogen atoms, respectively. (d) Quantum yield as a function of the negative voltage pulse. Imaging parameters of the inset in (a): f_0 = 813 kHz, A = 500 pm, Q = 24500, T = 78 K, V = + 0.8 V.

To complement the interpretation of the reversible migration of the H_{sub}, a typical *I–V* spectrum recorded precisely on the top of the H_{sub} is presented in Figure 5.7 (a). It shows that the tunneling current can be detected for negative (positive) voltage ≤ -2 V (≥ 2 V), which corresponds to the threshold of the tunneling electrons channel. In addition, according to the tunneling current and the time the sudden jump takes of each effective negative voltage pulse, the quantum yield Y is deduced as a function of voltage pulse V_s, *via* [15]

$$Y = e/I\tau$$

Where *e* is the elementary charge, *I* is the tunneling current during effective voltage pulse, and τ is the time it takes to a sudden jump, as shown in Figure 5.7 (d). The manipulation yield is strongly dependent on the pulse voltage. Specifically, note that, a sudden jump at about -3.5 V in the *I-V* spectrum in Figure 5.7 (a) is observed, which is quite consistent with the sudden increase in the manipulation yield from -3 to -3.5 V in Figure 5.7 (d).

In order to clearly explain the migration mechanism of the H_{sub} in our study, we propose one model to explain the manipulation process of the hydrogen atom by voltage pulse with different polarities, as schematically shown in Figure 5.8.

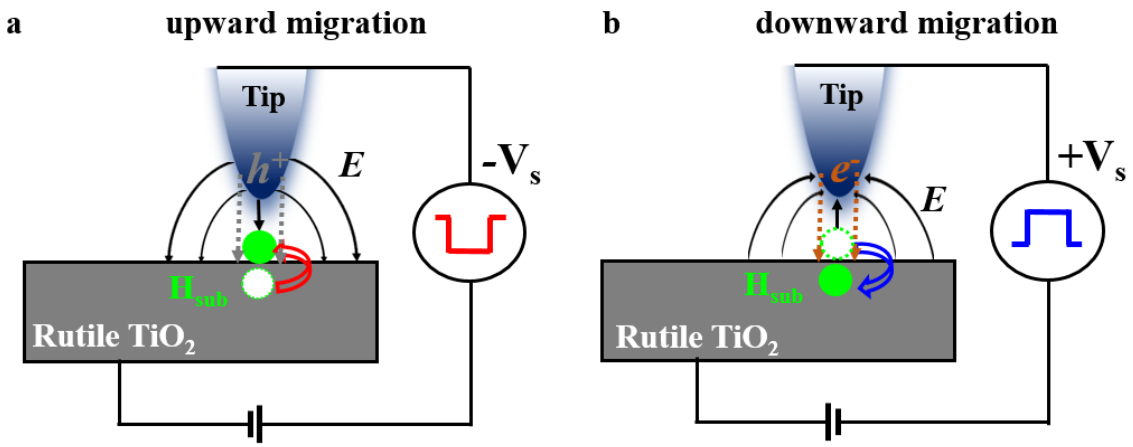

Figure 5.8 Schematic models for the upward and downward migration of hydrogen atom by controlling the polarities of the voltage pulse.

The migration directions of H_{sub}, namely, from the subsurface to surface layers or from surface to subsurface layers, are exclusively dependent on the polarities of the voltage pulse. With the negative (positive) voltage pulse, the local electric field is automatically formed between the tip and sample with the direction pointing from tip to sample (pointing from sample to tip), and the inelastic tunneling electrons can be injected to the target H_{sub} from the sample (tip) with high energy, which can activate the migration process of the hydrogen atom. The H_{sub} can controllably migrated upward or downward by controlling the polarities of the voltage pulse. We tentatively propose that the inelastic tunneling electrons and the local electric field effect play the key roles in the migration process of H_{sub}. It suggests that the electrically-driven migration of the subsurface defect is a much more complicated process, and it deserves further investigation, such as the Kelvin probe force spectroscopy (KPFS) technique.

5.4 Conclusion

In this study, we have systematically characterized and deliberately manipulated the subsurface hydrogen H_{sub} on rutile TiO_2(110)-(1 × 1) by nc-AFM/STM/KPFM in constant height mode at 78 K. Four different configurations of the H_{sub}, including the monomer, dimer, trimer and tetramer, are clearly observed and distinguished using the simultaneous nc-AFM and STM measurement. In addition, the local contact potential difference of the H_{sub} is mapped by KPFM with atomic resolution. In addition to characterizing the local geometric and electronic properties of the H_{sub}, we have also demonstrated our ability to reversibly manipulate the H_{sub} between subsurface and

surface layers by controlling the polarity of the voltage pulse. The reversible downward and upward migrations of the H_{sub} can be triggered by a positive and negative voltage pulse precisely applied above the target H_{sub}, respectively. The underlying mechanism of the reversible migration process of the H_{sub} is tentatively explained by the injection of inelastic tunneling electrons from the tip or from the subsurface polaron in substrate and the local electric field confined in the tunneling junction. Our study provides systematic investigation and unprecedented manipulation approach for the subsurface defect with atomic resolution and may potentially have an overriding effect on revolutionizing the investigation and applications of the catalytic reactions based on the metal oxides.

Chapter 6 Measurement and manipulation of the charge state of adsorbed oxygen adatoms on rutile TiO_2(110) by nc-AFM/KPFM

The following chapter is based on the publication:

Zhang, Q., Li, Y. J., Wen, H. F., Adachi, Y., Miyazaki, M., Sugawara, Y., Xu, R., Cheng, Z. H., Brndiar, J., Kantorovich, L. and Štich, I., Measurement and Manipulation of the Charge State of an Adsorbed Oxygen Adatom on the Rutile TiO_2(110)-1× 1 Surface by nc-AFM and KPFM. *Journal of the American Chemical Society*, *140*, 15668-15674, 2018.

6.1 Introduction

In this chapter, we focus on the investigation of the charge states of the adsorbed oxygen adatoms on rutile TiO_2 surface. Here, we have, for the first time, successfully measured and manipulated the charge state of the O_{ad} adsorbed on the reduced rutile TiO_2(110)-(1×1) surface using a combined system of home-built noncontact atomic force microscopy (nc-AFM) and Kelvin probe force microscopy (KPFM) at 78 K. In particular, we managed to clearly distinguish the differently charged single and double O_{ad} in AFM and KPFM images and assign them to O_{ad}^- (or $2O_{ad}^-$), O_{ad}^{2-} or ($2O_{ad}^{2-}$) and O_{ad}^--O_{ad}^{2-} species, respectively. These charged oxygen species are formed by transferring nominally one or two electrons to a local region around the adsorbed O_{ad} from the inhomogeneously distributed electron donors. This assignment is consistent with the appreciably stronger attractive force and larger V_{LCPD} obtained on the O_{ad}^{2-} compared to the O_{ad}^-. Furthermore,

in addition to our ability to distinguish the charge states of the adsorbed O_{ad}, we also demonstrate our ability to deliberately and reversibly manipulate the charge states between O_{ad}^{-} and O_{ad}^{2-} by changing the frequency shift set point (effectively, the tip height). The charge state transitions can be understood as arising from the tip-induced shifts of the electronic levels of the adsorbates due to inhomogeneous electric field modulated by the tip-sample distance. The experimental phenomena are analyzed by schematic energy models in combination with band-bending theory and density functional theory (DFT) simulations.

6.2 Methods

6.2.1 Experimental method

The nc-AFM images were obtained in the constant-frequency shift (Δf) mode and the KPFM images were recorded with a bias voltage feedback in the constant-height mode. A bias voltage was applied to the sample. All spectra on the target O_{ad} were measured with the atom tracking technique. [1] The clean sample was exposed to oxygen gas of (0.6 L, purity > 99.9 %) at room temperature and then the sample was characterized at 78 K.

6.2.2 DFT simulations

Our calculations were performed in the slab geometry with 3D periodic boundary conditions. The surface was modeled using a six-layer stoichiometric TiO_2 rutile slab. In the *z* direction, the slabs were separated from their periodic images by 15Å vacuum gap, see the SI for details. Calculations of the energies and forces were performed using DFT with projector augmented-wave pseudopotentials [2] along with the hybrid HSE06 exchange-correlation functional [3] and 400 eV plane wave cutoff as implemented in the VASP code. [4] The HSE06 functional was selected since the GGA treatment was unable to ensure localization of polarons and stabilize the O_{ad}^{-}–O_{ad}^{2-} configurations. PBE+U exchange-correlation functional [5,6] with U=2.5 eV was used

to crosscheck the results, where available. In this case the effect of the on-site Coulomb interaction correction on the localized Ti *d* electrons was taken into account. Ionic forces were converged to the accuracy better than 0.01 eV/Å.

Charging of the oxygen adatoms by the tip was modeled by directly adding/removing electrons to/from the oxygen adatoms in the following way. In experiments the charge transferred to the molecule has two possible sources: the tip and the substrate defects. In order to avoid complications of dealing with charged systems in a periodic setup, we model the electron reservoir by providing, as an artificial device, O-H/Ov defects in our simulation cell, ignoring the tip for simplicity, which leads to localized polarons. The charge trapped in the polarons is released either spontaneously or manually by slight structural deviations from the relaxed polaron geometry. This procedure captures correctly the major processes leading to charging of the oxygen adatoms, but ignores much smaller accompanying dipole interactions formed in the process of charging. In order to doubly charge two oxygen adatoms as done experimentally, we provide four electrons from two O_V donor defects built in our model, which leave electrons behind in the Ti *d* orbitals. [7] The same effect could have been achieved by considering the Ti_{int} interstitials which we argue elsewhere are in fact the dominant defects.

Bader analysis [8] of the formal charges was performed, for details see 5.6.10. In order to couple the simulations directly to the experimentally measured images, constant height images have been calculated. Assuming relatively large tip-surface distances *z*, only the local surface electrostatic potential $U_{loc}(z)$ is used to simulate the nc-AFM images. This approach ignores completely the large van der Waals (vdW) interaction and also the presumably much smaller exchange-correlation effects. In this approximation the tip force $F_{ts}(z) = -\frac{d}{dz}U_{loc}(z)$, while the frequency shift was obtained as [9]

$$\Delta f(d) \propto \int_0^{2\pi} F_{ts}(d + A\cos\varphi)\cos\varphi \, d\varphi.$$

This model is relevant to the hole mode imaging used in the experiments and corresponds to a point charge oscillating at a distance *d* with amplitude *A*; we have used *d* = 7Å and *A* = 4 Å.

6.3 Results and discussion

6.3.1 Clarification of the charge state of O_{ad} by AFM/KPFM

A representative atomic-scale nc-AFM image of the O–TiO_2(110)-(1×1) surface is shown in Figure 6.1(a). Here, the dark and bright rows correspond to the alternating five-fold coordinated titanium rows (Ti_{5c}) and two-fold coordinated bridge oxygen rows (O_{2c}), respectively. Several types of oxygen species on Ti_{5c} rows are clearly visible as bright spots with different contrast. The line profiles through two oxygen species of different contrast are shown in Figures 6.1(c,d). Note that precise quantification of the charge localized on each oxygen adatom represents an experimental challenge. We assign the faint single and double spots to O_{ad}^-/$2O_{ad}^-$, and the pronounced single and double spots to O_{ad}^{2-}/$2O_{ad}^{2-}$. The characterization of the charge state of the O_{ad} is performed at a relatively large tip-sample distance to avoid the tip effect. Note that the fact that the double oxygen adtoms are much more abundant than the single ones indicate that the adsorbed oxygen species are primarily dissociated by a non-vacancy mechanism and suggests that the Ti_{int} rather than O_v are the dominant defects. Comparison with calculated Bader charge analysis, [8] suggests that the O_{ad}^{2-} and O_{ad}^- are only charged by 0.75 and 0.45 electrons, respectively, which is due to the charge transferred to the surround substrate and other nearby surface oxygen atoms. In addition, we stress here that the O_{ad}^{2-} and $2O_{ad}^{2-}$ are the distinctly dominant species with a coverage of 0.078 ML (1 ML = 5.2 × 10^{14} /cm^2), compared to the O_{ad}^- and $2O_{ad}^-$ (0.013 ML). Our experimental results are in line with the computed relative energies of

2.66/0.96/0.0 eV for the $2O_{ad}^{-}$, O_{ad}^{-}-O_{ad}^{2-}, and $2O_{ad}^{2-}$ states shown in Figure 6.1 (b). The O_{ad}^{-}, $2O_{ad}^{-}$, O_{ad}^{-}-O_{ad}^{2-} states are local (meta)stable minima with sufficiently long lifetimes at low temperature. These experimentally observed high-energy states at 78 K can be interpreted by the local shortage of the polaronic defects. In addition, most adsorbed O_{ad} maintain their configurations as a pair of adjacent O_{ad} along the Ti_{5c} rows as $2O_{ad}^{-}$ or $2O_{ad}^{2-}$, which is due to the high dissociation energy barriers at the low temperature. [10] Our calculations show that these fully dissociated kinetically hindered states with the adsorbed O_{ad}^{2-} at the second-neighbor lattice distance are ≈0.7 eV lower in energy. Furthermore, the adjacent O_{ad} pairs suggest that the excess charge is primarily provided by the Ti_{int} in the substrate. [11] Though there are experimental challenges to directly characterize the Ti_{int}, the formation of fresh TiO_x islands [11,12] and the adjacent O_{ad} pair configuration indirectly indicate that the Ti_{int} in the substrate rather than the oxygen vacancies plays a dominant role in determining the adsorption and dissociation behaviors as well as the charge states of the O_{ad}.

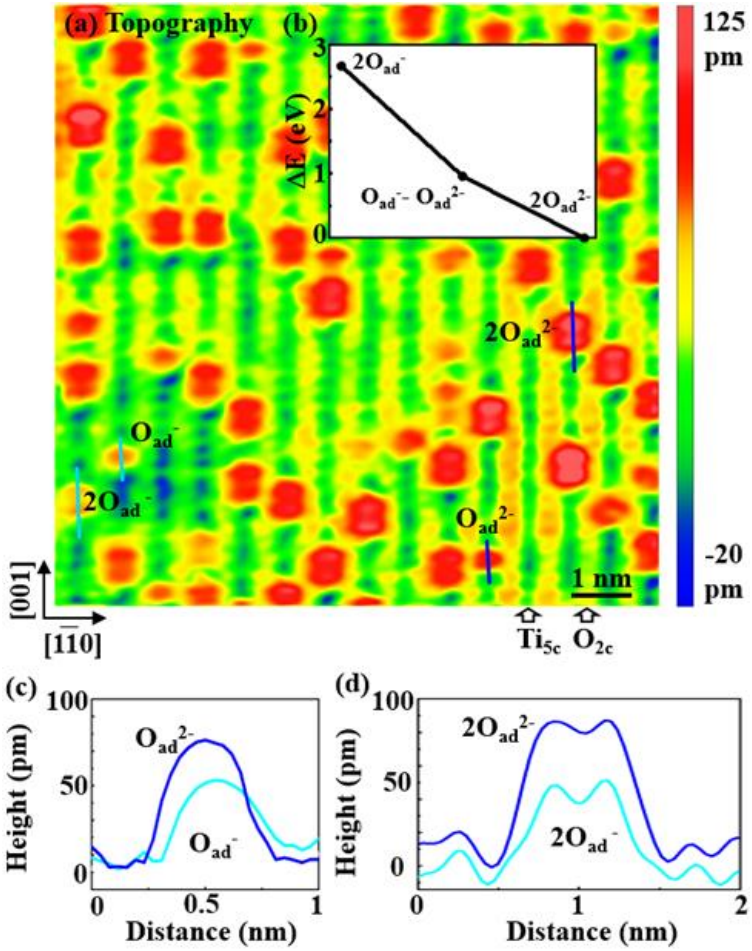

Figure 6.1 (a) Topographic AFM image (hole mode, 10×10 nm^2) of oxygen-rich TiO_2(110)-(1×1) surface. O_{2c}: two-fold coordinated bridge oxygen row. Ti_{5c}: five-fold coordinated titanium row. O_{ad}^-/$2O_{ad}^-$ (0.013 ML) and O_{ad}^{2-}/$2O_{ad}^{2-}$ (0.078 ML): single/double oxygen adatoms with different charge states. Imaging parameters: f_0 = 817 kHz, Q = 13700, T = 78 K, A = 500 pm, Δf = -440 Hz, V = +1.05 V. (b) Computed energies of the O_{ad} with different charge states; (c) and (d) corresponding line profiles of the O_{ad} with different charge states as indicated in (a).

In Figure 6.2, we show the simultaneous AFM (Δf) and KPFM (V_{LCPD}) images of the O_{ad} on rutile TiO_2(110)-(1×1) measured in the constant–height mode. As shown in Figures 6.2(a-c), we have obtained several different contrast patterns of the oxygen adatom species on the Ti_{5c} rows, which we assign to $2O_{ad}^-$ and $2O_{ad}^{2-}$, respectively. Besides that, we also observe O_{ad}^-–O_{ad}^{2-} species

which, compared to $2O_{ad}^{-}$, are theoretically predicted to be energetically much more favorable. The DFT simulated $|\Delta f|$ images of $2O_{ad}^{2-}$, $2O_{ad}^{-}$ and O_{ad}^{-}–O_{ad}^{2-} species are presented in Figures 6.2(d-f), respectively. These computed images exhibit excellent agreement with the measured images. The simulations also suggest that the configuration with the *p*-orbitals rotated from the main $[1\bar{1}0]$ axis is one of several quasi-degenerate local minima the system may assume. And indeed, the experiment/theory comparison strongly suggests a subatomic experimental resolution as rotated oxygen *p*-orbitals of the $2O_{ad}^{-}$ species are imaged as shown in Figures 6.2 (b,e). The corresponding line profiles are shown in Figures 6.2 (j,k). We found that $2O_{ad}^{2-}$, compared to $2O_{ad}^{-}$, yields significantly larger absolute values of the Δf and V_{LCPD}, indicating a larger charge, in perfect agreement with the findings in Figure 6.1. Contrary, the "sizes" of the three oxygen species are broadly similar, both experimentally and from the simulations.

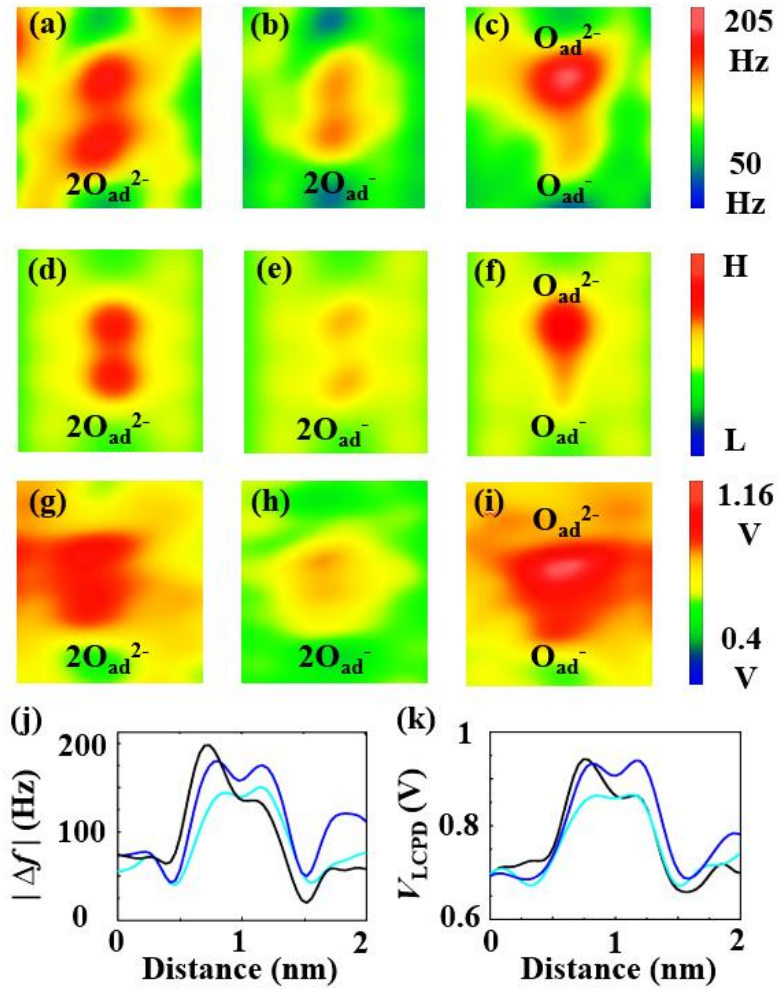

Figure 6.2 (a-c) Experimental and (d-f) simulated $|\Delta f|$ images (0.7×1.5 nm^2) of O_{ad} species on rutile TiO_2(110)-1×1 surface, respectively. (g-i) Experimental KPFM (V_{LCPD}) images of the same area as shown in (a-c). (j) and (k) Line profiles of $|\Delta f|$ and V_{LCPD} of te O_{ad} species with different charge states. Imaging parameters: Q = 13500, f_0 = 817 kHz, A = 500 pm, Δf = -330 Hz.

The different image contrast of the O_{ad} species with different charge states in the AFM images is predominantly attributed to the different short-range force (F_{SR}). We measured the F_{SR} on these two species, as shown in Figure 6.3(a). We find that the maximum attractive force on the O_{ad}^{-} is appreciably smaller than that on O_{ad}^{2-}, which is quite consistent with the experimental results in Figure 6.1. We stress here that we employed the atom tracking-technique to compensate the

thermal drift effects during spectra measurement. [1] After spectra measurements, the same area was characterized again to confirm that no unexpected tip-induced manipulation of the adsorbed O_{ad} happened, such as a charge state transition or lateral displacement.

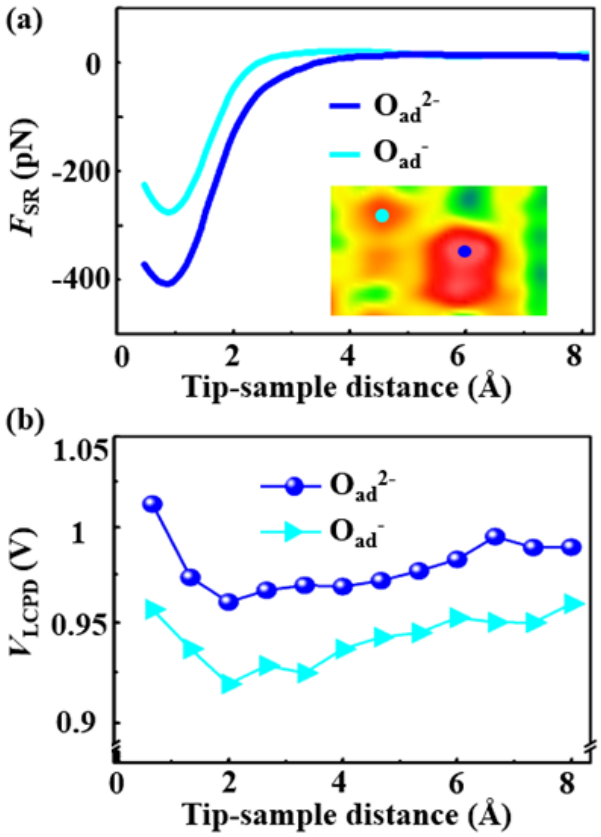

Figure 6.3 (a) Short-range force (F_{SR}) and (b) V_{LCPD} curves measured on O_{ad}^{-} and O_{ad}^{2-}, respectively. Imaging parameters: f_0 = 817 kHz, A = 500 pm, Q = 13700, T = 78 K, Δf = -340 Hz.

We have further investigated the effect of the charge states of the oxygen adatoms on the V_{LCPD} by performing Kelvin probe force spectroscopy (KPFS) as a function of the tip-sample distance. By fitting each parabola of $\Delta f(V)$ at a constant tip-sample distance, the peak positions of the corresponding bias voltage are determined as the V_{LCPD}. Quantitatively, the V_{LCPD} values are affected by many factors, such as the tip apex and tip polarity. As shown in Figure 6.3(b), the

V_{LCPD} trend we obtained in our experiment is that the V_{LCPD} values on O_{ad}^- sites are always smaller than those on O_{ad}^{2-} sites. We attribute this V_{LCPD} trend to the potential difference of the O_{ad} induced by less charge on the O_{ad}^- sites compared to the O_{ad}^{2-} sites, resulting in smaller V_{LCPD} values. On the other hand, the variation of V_{LCPD} values also directly indicates the change of band bending of the substrate. [13,14] Our experimental results demonstrate that the charge states of the O_{ad} can be clearly identified because of the strong (subatomic) AFM and KPFM images contrast.

6.3.2 Manipulation of the charge state of O_{ad} by AFM

Our experiments, corroborated by computed energies, clearly suggest that O_{ad}^{2-} and $2O_{ad}^{2-}$ are ground state configurations whereas O_{ad}^-, $2O_{ad}^-$, and O_{ad}^-–O_{ad}^{2-} are local minima charge configurations made kinetically metastable at the low temperature used here. Therefore, in line with the previous related work, [15-17] which proved applicability of the nc-AFM to controlled manipulation of the charge states of adsorbed atoms and molecules, we explore now the nc-AFM tip as a tool for charge state manipulation of the adsorbed O_{ad}.

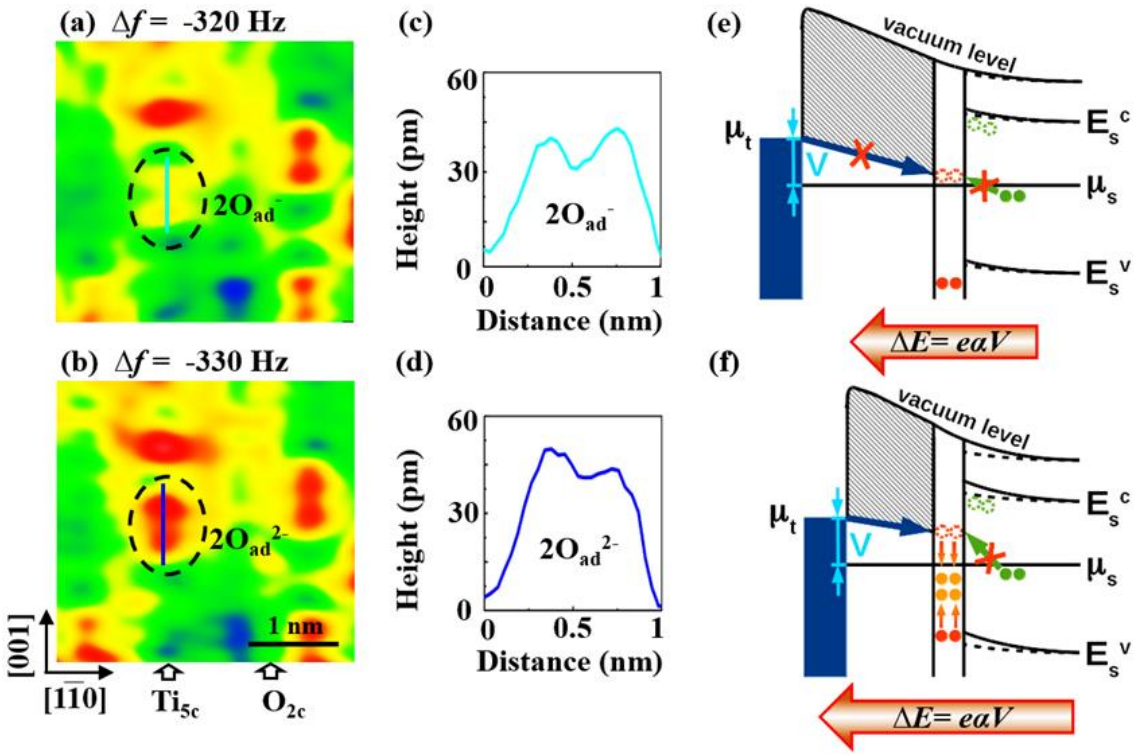

Figure 6.4 (a) and (b) Constant-Δ*f* AFM images of the charging process of the adsorbed oxygen adatoms by the AFM tip. (c) and (d) The corresponding line profiles of target $2O_{ad}^-$ and $2O_{ad}^{2-}$ species labeled by dashed black ovals in (a) and (b). (e) and (f) The corresponding schematic models showing the key electronic energy levels and tunneling barriers responsible for the charging process. *e*, elementary charge; α, level arm; *V*, bias voltage. Occupied/unoccupied states of oxygen electrons (full/empty dashed circle) are depicted in orange/red for $2O_{ad}^{2-}/2O_{ad}^-$. Occupied/unoccupied polaronic states (full/empty dashed circles) are depicted in green, the tip states in blue. μ_t and μ_s are the Fermi energies of the tip and surface, E_s^v and E_s^c are the top and the bottom of the surface valence and conduction bands, respectively. The band bendings shown correspond to the oxygen adsorption (dashed lines) and to the total bending including also the metal-semiconductor contact bias induced field effect (full lines). The arrows indicate the repositioning of the respective levels in energy, the crosses the inhibited processes. The indicated

trends follow from DFT calculations shown in Figure 5.16. Imaging parameters: (a) Δf = -320 Hz, V = +1.05 V; (b) Δf = -330 Hz, V = +1.05 V.

Figure 6.4 shows a charging process of the adsorbed oxygen adatoms induced by a modification of the frequency shift (set point) under a fixed applied positive bias voltage. In Figure 6.4(a), an oxygen adatom pair indicated by a dashed black oval is imaged as a couple of weak contrast spots and accordingly assigned to the $2O_{ad}^{-}$ species. By gradually increasing the frequency shift (decreasing the tip-sample distance) with applied constant bias voltage of +1.05 V, the species is pairwise charged to $2O_{ad}^{2-}$ (two spots with strong contrast), Figure 6.4(b). To shed more light, we show in Figures 6.4(c,d) the corresponding line profiles which corroborate the above assignments. The underlying charging mechanism is explained in Figures 6.4(e,f), which shows the schematics of the key electronic energy levels shifts and the tunneling barrier. Here, the charging process of the O_{ad} species is attributed to the gradually enhanced tip-induced electric field E, [15,16] which is because of the decreased tip-sample distance. The E results in the tunneling electrons transferring from the tip to the adsorbed O_{ad} species. The magnitude of the energy shift induced by the electric field, ΔE, can be modeled as: [16]

$$\Delta E = e\alpha V,$$

where α is the level arm which is inversely proportional to the tip-sample distance d. With a constant bias voltage V, the ΔE only depends on d. As discussed above, the O_{ad}^{-} and $2O_{ad}^{-}$ are kinetically hindered being kept at equilibrium due to the polarons effect. With gradually increased ΔE, the E can induce electron tunneling through the vacuum gap and injection to the $2O_{ad}^{-}$ when the threshold electric field, E_{th}, is reached. As a consequence, the adsorbed $2O_{ad}^{-}$ can be charged to $2O_{ad}^{2-}$. With the charge state transition of the O_{ad}, the unoccupied level of the singly charged O_{ad} is gradually raised up, which is accompanied by further upward band bending. [14] When a

fully charged oxygen species, namely, $2O_{ad}^{2-}$, is formed, further electron injection from the tip is thus hindered. This also indicates that the $O_{ad}^{2-}/2O_{ad}^{2-}$ are the most stable species, which is consistent with the experimental results observed in Figure 6.1(a) as well as with the computed energies of the O_{ad} with different charge states, as shown in Figure 6.1(b).

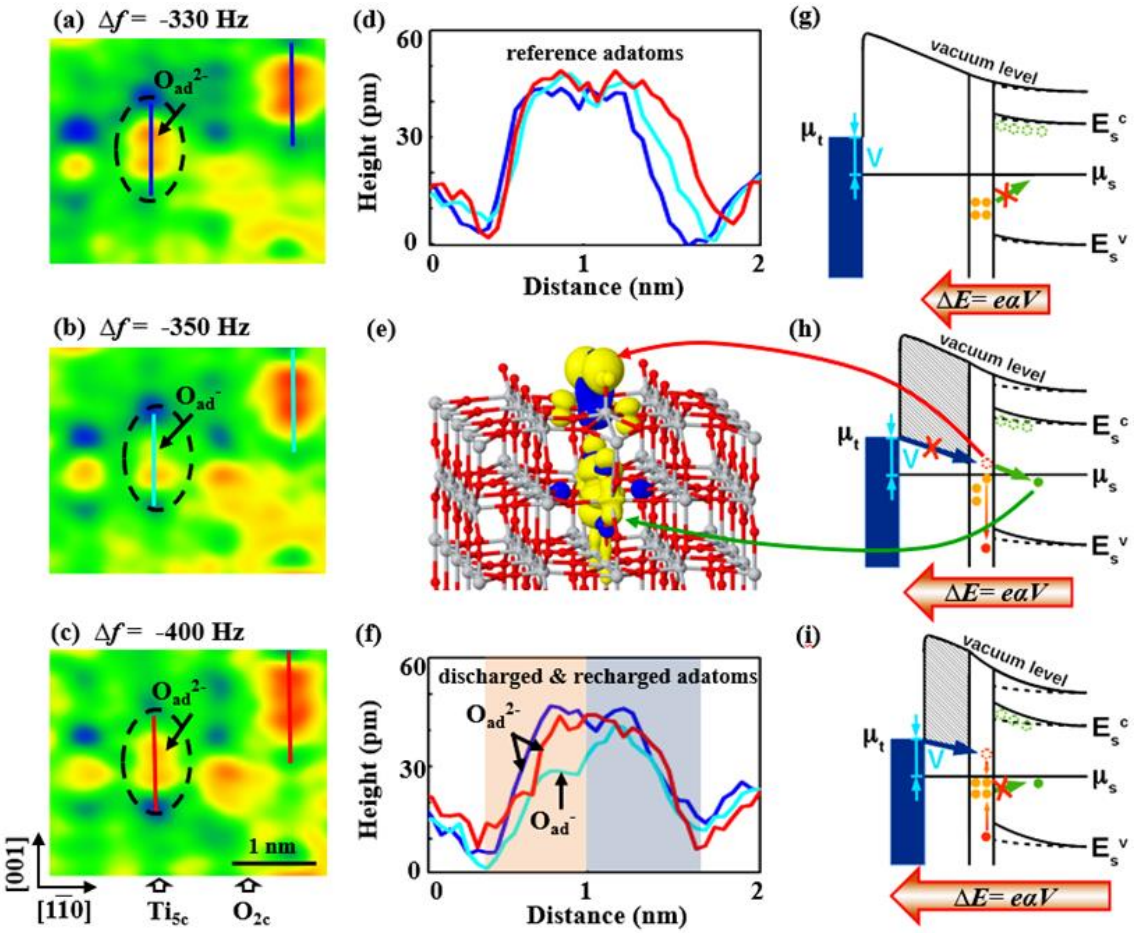

Figure 6.5 Constant-Δ*f* AFM images of (a) $2O_{ad}^{2-}$, (b) O_{ad}^{-} – O_{ad}^{2-} and (c) $2O_{ad}^{2-}$ species. (e) Calculated magnetization (spin density) depicting an empty O_{ad}^{-} orbital along with a subsurface polaron (yellow/blue). (d), (f) Line profiles corresponding to reference and target O_{ad} species as indicated by the same colors in (a-c). (g-i) Corresponding schematic models showing the key electronic energy levels and tunneling barriers responsible for the charging process. The same

notations are used as in Figure 5. Imaging parameters: (a) Δf = -330 Hz, V = +1.05 V; (b) Δf = -350 Hz, V = +1.05 V; (c) Δf = -400 Hz, V = +1.05 V.

After having demonstrated the ability to charge the adsorbed $2O_{ad}^-$ species to $2O_{ad}^{2-}$ by reducing the tip height, we now demonstrate also the opposite process of a reversible discharging/recharging of the adsorbed oxygen adatom simply by a continuous reduction of the tip-sample distance, ***d,*** while keeping the same voltage. The fact that both charging and discharging processes do occur at the same voltage suggests an activation of different processes by the tip via modulating the tip-induced electric field. The process is demonstrated in Figure 6.5. In the charge state transition regime, one of the two O_{ad}^{2-} atoms in Figure 6.5(a) is discharged to O_{ad}^-, Figure 6.5(b), and recharged again to O_{ad}^{2-}, Figure 6.5(c), simply by controlling the tip-sample distance d and hence the electric field E. For clarity, the corresponding line profiles of the reference and target O_{ad} pairs (indicated by the black dashed circles) are presented in Figures 6.5(d,f), respectively. The models of the key electronic energy levels and tunneling barriers are schematically shown in Figures 6.5(g-i). We propose that in the discharging process, from (a) to (b), the enhanced electric field, E, can induce the electrons transferring from the O_{ad}^{2-} to the substrate as a polaron. Meanwhile, the unoccupied O_{ad}^- state is formed and lifted upwards in energy by the AFM tip. As expected, the electron tunneling probability increases with the further decreased tip-sample distance, resulting in the injection of an electron from the tip into the fresh O_{ad}^-. The O_{ad}^{2-} species is reformed as shown in Figure 6.5(c,i). The model presented in Figures 6.5(g-i) assumes discharging into a polaron as explicitly built in our computational model. In reality, as also indicated by Figures 6.5(a,b), instead of charging a polaron in the substrate, the charge may be transferred to the nearby O_{ad}, which has an energy level close to the polaronic levels. Surprisingly, besides the reversible charging and discharging switching process, some

unexpected phenomena are obtained as well. For example, the other O_{ad}^{2-} pairs maintain stable configurations during the charge state switching of the target O_{ad}^{2-}. We interpret this experimental phenomenon by a shortage of states available for draining charge. This is in line with the previous experimental observations on charge manipulation of oxygen molecules on the anatase TiO_2 surface. [13]

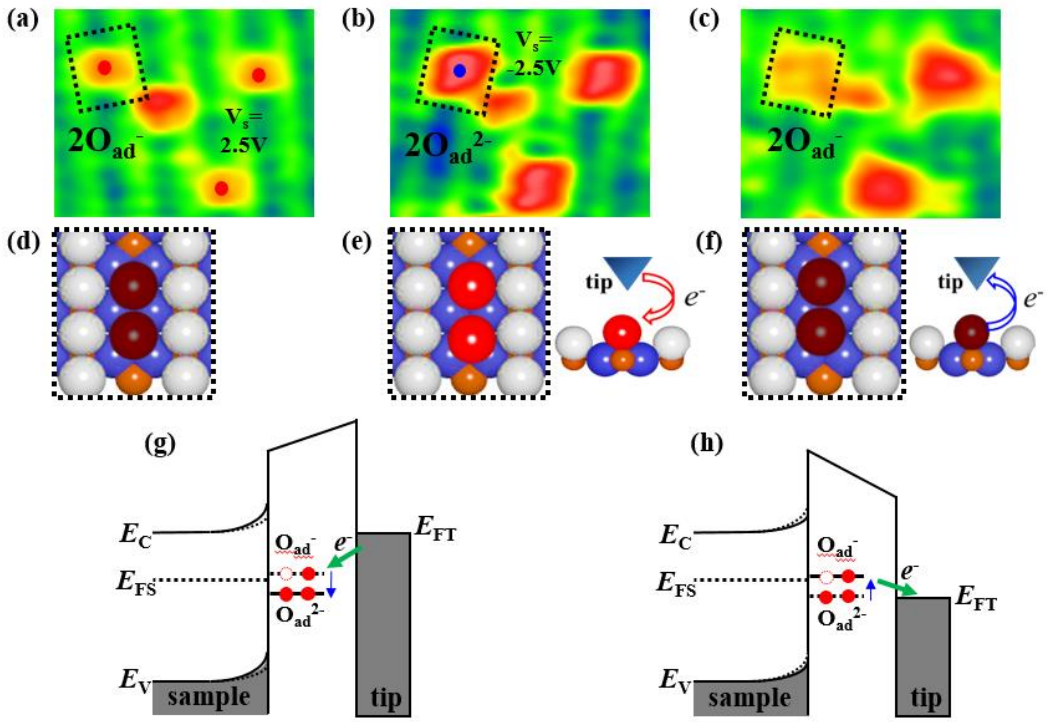

Figure 6.6 (a-c) Constant-Δf AFM images of charge states transition of O_{ad} between $2O_{ad}^{2-}$, and $2O_{ad}^-$ species. (d-f) Corresponding schematics of O_{ad} species and tunneling electron transport. (g, h) Corresponding schematic models showing the key electronic energy levels and tunneling barriers responsible for the charging and discharging process. Imaging parameters: (a-c) Δf = -350 Hz, V = +1.05 V.

The reversible charge states transition of O_{ad} can also be induced by changing the energy lever of the tip by using the voltage pulse with different polarities, as shown in Figure 6.6. In the charging process in Figure 6.6(a,b), the positive voltage pulse of 2.5 V with 100 ms duration was applied in the middle of the O_{ad} pairs, as the red dots indicated in Figure 6.6(a). After that, the O_{ad}^{-} pairs were charged to O_{ad}^{2-} pairs, in which the tunneling electrons can be injected from the tip to the target Oad pairs, as schematically shown in Figure 6.6(e,g). The charged $2O_{ad}^{2-}$ can then be discharged to $2O_{ad}^{-}$ by the negative voltage pulse of – 2.5 V with 100 ms duration, as shown in Figure 6.6(b,c). In the O_{ad} discharging process, the electrons can be extracted from the O_{ad} by the tip, as schematically shown in Figure 6.6(f,h). We demonstrate that the charge states of O_{ad} can be reversibly switched by controlling the voltage pulse qualitatively, and we speculate that the charge states transition yields are dramatically determined by the magnitude of the voltage pulse and the duration time of the voltage pulse. We stress that in the reversible charge states transition of the O_{ad}, the energy level of the tip can be deliberately modulated by controlling the voltage pulse polarity, as schematically indicated in Figure 6.6(g,h), with a constant tip-sample distance. In addition, the downward and upward band bending of the substrate can be induced in the discharging and charging process of the O_{ad} due to the electrons transport, respectively.

We demonstrate that the charge states of adsorbed O_{ad} on rutile TiO_2(110) surface can be reversibly manipulated with single electron sensitivity by controlling the tip-sample distance and the sample bias voltage. In the charge state transition process, the electrons can be injected from the tip to the O_{ad}, or from the adsorbed O_{ad} to the tip or to the substrate to from the polaron, in which the energy level between tip and sample plays a key role in the tunneling electrons transport process.

6.4 Conclusion

In conclusion, we have investigated the charge states of the adsorbed single and double oxygen atoms adsorbed on the rutile TiO_2(110)-1×1 surface by nc-AFM and KPFM at 78K in ultrahigh vacuum. We managed to clearly identify with atomic/subatomic resolution the differently charged single and double oxygen adatoms as $O_{ad}^-/2O_{ad}^-$, $O_{ad}^{2-}/2O_{ad}^{2-}$ and $O_{ad}^-–O_{ad}^{2-}$ species, respectively, combining the measurement of F_{SR} and V_{LCPD} as a function of the tip-sample distance and extensive DFT simulations. $O_{ad}^-/2O_{ad}^-$ and $O_{ad}^-–O_{ad}^{2-}$ species are metastable but can still be observed at low temperatures despite their formation energies being up to ≈ 3 eV higher than the ground state $O_{ad}^{2-}/2O_{ad}^{2-}$ species. Comparison with DFT simulations reveals that the charge transferred to/from the adatoms is smaller than the nominal charge, due, in part, to the fact that charge is transferred also to other nearby surface oxygen atoms. In addition to determining the charge states of the oxygen adatoms, we also succeeded in deliberately charging and discharging, individually and pairwise, the oxygen adatoms by the nc-AFM tip by means of gradually decreasing the tip-sample distance, while keeping the sample at a fixed positive voltage, and by using the voltage pulse with different polarities. The fact that both charging and discharging processes do occur at constant voltage suggests an activation of different processes due to modulating the tip-induced electric field. We argue that the charging processes involve electron tunneling from the tip into the oxygen adatom *p*-states while the discharging process proceeds by draining the charge into polarons or other nearby oxygen adatoms, which all are close in energy. For that reason, manipulation of other adatoms on different parts of the surface may not be possible under otherwise identical experimental conditions due to local shortage of states available for the discharge. The polarons abundant on the rutile TiO_2(110) surface play a vital role in the processes studied. In that respect, the importance of the bulk interstitial defects, Ti_{int}, was

particularly emphasized. Moreover, the reversible charge states switching can also be induced by changing the energy level of the tip using voltage pulse with different polarities. The tunneling electrons can be injected to the target O_{ad} from the tip with positive bias voltage, and can also be extracted from the O_{ad} by the tip with negative voltage pulse. Our study shows a novel route for the measurement and manipulation of the charge states of the adsorbates at the atomic scale and opens a door for further investigation of electronic devices and catalytic reactions based on single atoms.

Chapter 7 Charge state dependence of oxygen adatom conductance switching on rutile TiO_2(110)

7.1 Introduction

In this chapter, we systematically investigated the conductance states of single O_{ad} on rutile TiO_2(110)-(1 × 1) surface depending on its charge states by a combined low-temperature AFM/STM probing system with atomic resolution. We clearly demonstrated that the atomic O_{ad} conductance state exclusively depends on its charge state, that is, the O_{ad}^- shows relatively higher conductance than O_{ad}^{2-}, based on the experimental qualitative and quantitative analysis. In addition, by means of sweeping the bias voltage and tip-sample distance, we successfully managed to reversibly switch the O_{ad} conductance between relatively high and low states by deliberately controlling its charge state between O_{ad}^- and O_{ad}^{2-}. We stress that the abundant surface/subsurface polarons in rutile TiO_2(110) and the tip-induced local electric field play a vital role in the reversible charge and conductance states transformation process. We believe that our work provides a pioneering study about the systematic investigation and reversible transition of the atomic conductance behavior at single atom level, and can potentially revolutionize the charge transfer related reactions, specifically, the catalytic reactions.

7.2 Methods

A dc bias voltage (V_s) was applied to the sample and the time-averaged tunneling current ($<I_t>$) was detected from the tip. Simultaneous frequency shift Δf and $<I_t>$ images were measured in constant height mode to avoid the crosstalk. All spectra were recorded with the atom tracking technique to compensate the thermal drift. Oxygen gas (purity > 99.9%, 0.6 L) was exposed to the clean sample at room temperature, and all the measurements were performed at 78 K.

7.3 Results and discussion

7.3.1 Charge state dependence of O_{ad} conductance state

First, the dependence of O_{ad} conductance behavior on its specific charge state is investigated using simultaneous nc-AFM and STM measurement in constant height mode at 78 K. Here in this work, since a conductive metal AFM tip was used as a sensor that can form a tunnel junction with the sample, the Δf and $<I_t>$ signals can be recorded simultaneously, which provides the electrostatic and electronic information with atomic resolution. [3,4] Based on our previous studies, [1,2] the charge states of O_{ad} can be clearly distinguished and clarified as O_{ad}^{-} and O_{ad}^{2-} with relatively darker and brighter contrast in topographic nc-AFM image, respectively. A set of representative $|\Delta f|$ (nc-AFM, hole mode) and corresponding $|<I_t>|$ (STM, empty state) images of the chemisorbed O_{ad} with different charge states on rutile TiO_2(110) surface is shown in Figure 7.1. The images are simultaneously recorded in a stable fashion with a relatively low bias voltage (+ 1V) and large tip-sample distance to guarantee no unexpected tip-induced geometric or electronic manipulation for the O_{ad}. Here, the dark and bright rows correspond to the alternating 5-fold coordinated titanium rows (Ti_{5c}) and 2-fold coordinated bridge oxygen rows (O_{2c}) in the $|\Delta f|$ image and O_{2c} and Ti_{5c} rows in the $|<I_t>|$ image, respectively. In the $|\Delta f|$ image, two types of

O_{ad} with relatively darker and brighter contrast can be clearly distinguished and assigned to O_{ad}^{-} and O_{ad}^{2-}, according to our previous works. [1,2] Interestingly, in the corresponding $|<I_t>|$ image, the image contrast of O_{ad}^{-} and O_{ad}^{2-} is reversed, that is, the O_{ad}^{-} shows much brighter contrast than O_{ad}^{2-}. Up to now, numerous STM works have been performed to investigate the O_{ad} on rutile TiO_2 surface, [5-10] while rare of them have discussed and distinguished the O_{ad} with different charge states, which we speculate it is possibly because of the similar contrast of O_{ad}^{2-} with the Ti_{5c} row, as shown in Figure 7.1(b). It is worth noting that it is the first time to experimentally distinguish the adsorbates charge state on semiconductors by using STM with atomic resolution, rather than on insulating film. [11,12] We stress that no spontaneous conformational or charge state changes of the O_{ad} was observed during normal characterization with low bias voltage, indicating the high stability of the O_{ad} with different charge states. In this regard, we speculate that the polarons in rutile TiO_2(110) is dominantly responsible for the stabilization of the chemisorbed adsorbates with multiple charge states by localizing and stabilizing the excess electrons. [13,14]

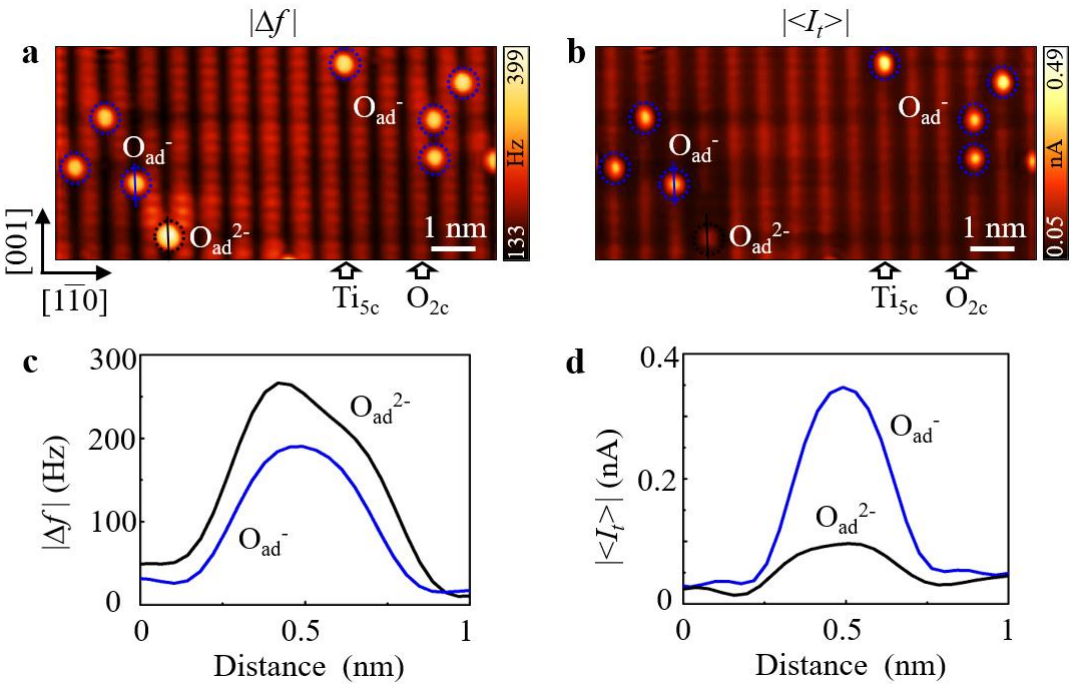

Figure 7.1 Simultaneous nc-AFM and STM characterization of the oxygen adatoms (O_{ad}) on rutile TiO_2(110)-(1×1) surface in constant height mode. a Frequency shift $|\Delta f|$ (nc-AFM, hole mode, 10×4.8 nm^2) image. b Corresponding time-averaged tunneling current $|\langle I_t \rangle|$ (STM, empty state, 10×4.8 nm^2) image of the same area as shown in a. c and d Corresponding line profiles of the $|\Delta f|$ and $|\langle I_t \rangle|$ as the solid blue and black lines indicated in a and b, respectively. O_{2c}: 2-fold coordinated bridge oxygen row. Ti_{5c}: 5-fold coordinated titanium row. O_{ad}^- and O_{ad}^{2-}: single oxygen adatom charged by one and two electrons, respectively. Imaging parameters: f_0 = 807 kHz, A = 500 pm, Q = 21460, T = 78 K, V_s = + 1 V.

More importantly, the simultaneous AFM and STM measurement provides an efficient and convincing approach to investigate the relation between charge and conductance states of the O_{ad}. Here, we tentatively assign that, in the $|\langle I_t \rangle|$ image in constant height measurement mode, the different O_{ad} contrast could be dominantly attributed to the variation of the O_{ad} conductance. [15] Note that the O_{ad}^- and O_{ad}^{2-} are all precisely located on Ti_{5c} row with similar conformation, which excludes the geometric effect on its different conductance behavior. As a consequence, we strongly propose that the different conductance behavior of the O_{ad} is fundamentally governed by its specific charge state, that is, the O_{ad}^- has significantly higher conductance than O_{ad}^{2-}. To gain more information, the line profiles of $|\Delta f|$ and $|\langle I_t \rangle|$ through two oxygen species are shown in Figure 7.1(c,d), which indicate that the O_{ad}^- has around three times higher conductance than O_{ad}^{2-} under current experimental condition. Quantitatively, many factors can affect the conductance values, for example, the tip-sample distance and tip apex termination. [4] In this study, our experimental results qualitatively demonstrate that the O_{ad} conductance state strictly depends on its charge state, and the O_{ad}^- has significantly higher conductance than O_{ad}^{2-}.

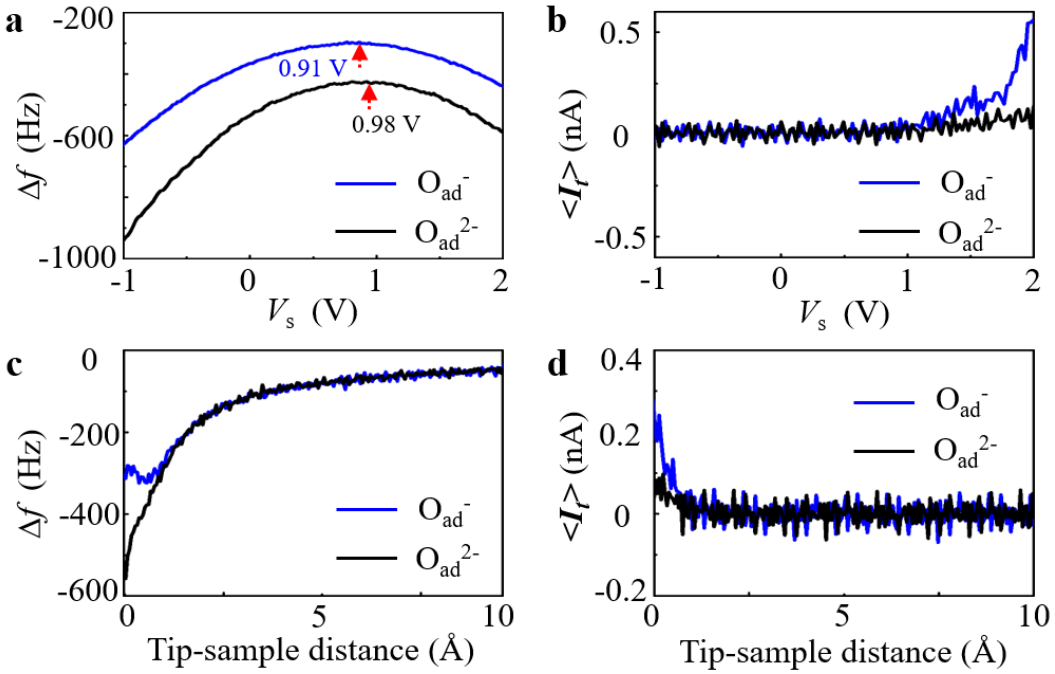

Figure 7.2 Quantitative analysis of the charge and conductance states of O_{ad}^- and O_{ad}^{2-}. a and b Simultaneously recorded frequency shift Δf and tunneling current $\langle I_t \rangle$ signals by ramping the sample bias voltage from -1 V to 2 V, respectively. c and d Δf and $\langle I_t \rangle$ signals measured as a function of the tip-sample distance simultaneously. Each spectrum is precisely recorded on top of the O_{ad}^- (blue lines) and O_{ad}^{2-} (black lines) with V_s of 1 V.

To unambiguously demonstrate our above discussion, we now exploit and clarify the dependence of O_{ad} conductance behavior on its charge state as a function of the bias voltage and tip-sample distance. In Figure 7.2 (a,b), the tip is precisely positioned on O_{ad}^- and O_{ad}^{2-} with atom tracking technique to compensate the thermal drift effect, [16] and the bias voltage is swept from -1 V to 2 V while recording the Δf and $\langle I_t \rangle$ singles simultaneously. By fitting the two parabolas of $\Delta f(V_s)$ in Figure 7.2(a), the peak positions of the corresponding V_s are determined as the local contact potential difference (V_{LCPD}), which is experimentally demonstrated to reflect the accumulation amount of charge on O_{ad}. [1] The V_{LCPD} values of 0.91 V and 0.98 V of O_{ad}^- and

O_{ad}^{2-} directly indicate the different charge states, which is perfectly consistent with our previous work. [1] In the corresponding $<I_t>(V_s)$ curves in Figure 7.2(b), it is noticed that the $<I_t>$ on O_{ad}^{-} is always larger than that on O_{ad}^{2-} after reaching the threshold bias voltage, and the $<I_t>$ difference between O_{ad}^{-} and O_{ad}^{2-} is appreciably growing with increasing bias voltage. Moreover, the tip-sample distance effect on the O_{ad} charge and conductance states is investigated in Figure 7.2(c,d). The larger absolute value of Δf on O_{ad}^{2-} than that on O_{ad}^{-} indicates the stronger maximum attractive force on O_{ad}^{2-} than that on O_{ad}^{-}, which is in good agreement with the experimental results in Figure 1 and our previous experimental results. [1] In the corresponding $<I_t>$ signal in Figure 7.2(d), the $<I_t>$ on O_{ad}^{-} is larger than that on O_{ad}^{2-} when exceeding the threshold tip-sample distance to allow tunneling current flow. We note that, after each spectrum, the same O_{ad} is characterized again with identical scanning parameters to ensure no unexpected tip-induced conformational or electronic manipulation, which can actually also be verified by the smooth spectra in a stable fashion without any discontinuity. It is indeed demonstrated that, though noise exists in the spectra due to the tip oscillation, the O_{ad}^{-} has higher conductance than O_{ad}^{2-}, and it is an inherent property of the O_{ad} determined by its specific charge state, which is independent of the bias voltage and tip-sample distance.

7.3.2 O_{ad} conductance switching induced by charge state transition

As we have previously demonstrated that the charge state of O_{ad} can be controllably and reversibly switched between O_{ad}^{-} and O_{ad}^{2-}, [1,2] therefore, in line with the recent charge induced molecular conductance switching studies, [17-19] we now exploit and demonstrate the ability to deliberately manipulate the O_{ad} conductance behavior by controlling its charge state with single electron sensitivity.

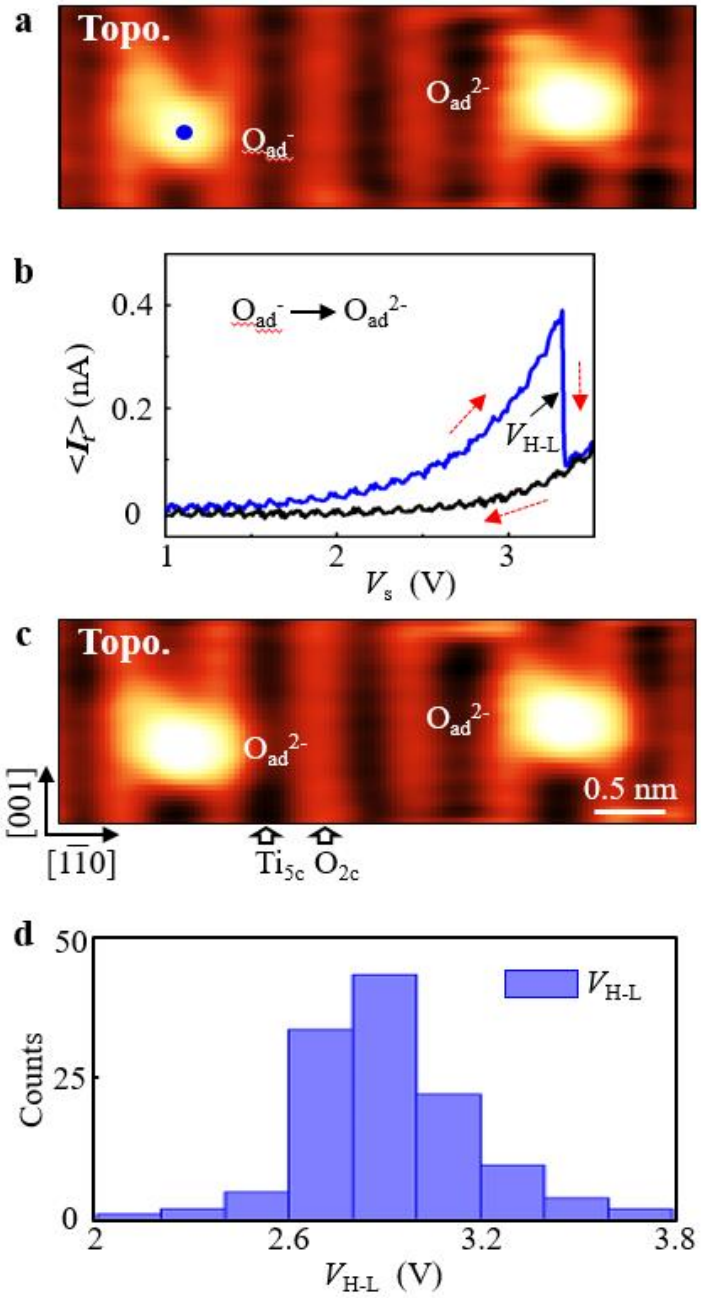

Figure 7.3 O_{ad} conductance transition by switching the O_{ad} charge state from O_{ad}^{-} to O_{ad}^{2-}. a and c Topographic nc-AFM images (hole mode, 4.4×1.4 nm^2) of O_{ad} before and after sweeping the bias voltage, respectively. b Tunneling current $<I_t>$ signal recorded on O_{ad}^{-} by sweeping the sample bias voltage between 1 V and 3.5 V with duration of 1 s. d Transition bias voltages from high conductance to low conductance (V_{H-L}) as indicated in b. The blue dot in a means the site of bias

voltage sweeping. Imaging parameters: f_0 = 807 kHz, A = 500 pm, Q = 21460, T = 78 K, V_s = + 1 V.

Figure 7.3 shows a unidirectional O_{ad} conductance transition process by manipulating its charge state. In Figure 7.3(a), the O_{ad}^- and O_{ad}^{2-} species can be clearly distinguished depending on its contrast in nc-AFM topographic image with a low scanning bias voltage. The tip is precisely positioned on top of O_{ad}^-, as the blue dot indicated in Figure 7.3(a), and then the bias voltage is swept from 1 V (scanning bias voltage) to 3.5 V, and then back to 1 V with a sweeping duration of 1 s while monitoring the $<I_t>(V_s)$ signal. The feedback loop is temporarily interrupted to keep a constant tip-sample distance during bias voltage sweeping. At the start of the bias voltage sweeping, it is in the high conductance state, which is in line with the aforementioned discussion of the high conductance of O_{ad}^-. Then there is a sudden discontinuity in the forward $<I_t>(V_s)$ curve at around 3.3 V, from high conductance state (H) to the low conductance state (L), as shown in Figure 7.3(b). In the backward $<I_t>(V_s)$ curve, it remains in the low conductance state until the bias voltage sweeps back to 1 V. We believe that such dynamic conductance transition is exclusively because of the O_{ad} charge state switching from O_{ad}^- and O_{ad}^{2-}, which is experimentally verified by re-scanning the same area with identical scanning parameters. In this charge and conductance transition process, we speculate that the tip-induced local electric field can dominantly govern the tunneling electrons injection from the conductive tip into the O_{ad} when the bias voltage exceeds a given threshold voltage ($V_{H\text{-}L}$). [1] More than one hundred cycles of conductance transition from high to low state have been performed, and the threshold voltages ($V_{H\text{-}L}$) are summarized in Figure 7.3(d). Though, quantitatively, the $V_{H\text{-}L}$ can be affected by many factors, such as tip-sample distance, tip apex termination and subsurface conditions, it suggests that the $V_{H\text{-}L}$ is dominantly in the range of 2.6 V ~ 3 V by statistical analysis. In addition, in line

with previous works about the reversible conductance switching, [20,21] Here we speculate that the polaron in rutile TiO_2(110) is primarily responsible for the O_{ad} discharging and corresponding conductance switching process by accepting the electrons from O_{ad}, which is electrically activated by the tip-induced local electric field. Our work is quite consistent with the charge induced molecular conductance hysteresis. [18,19] Such tunneling current discontinuity and hysteresis induced by the bias voltage sweeping clearly corresponds to the change of conductance state of single O_{ad}, which is exclusively because of its charge state switching.

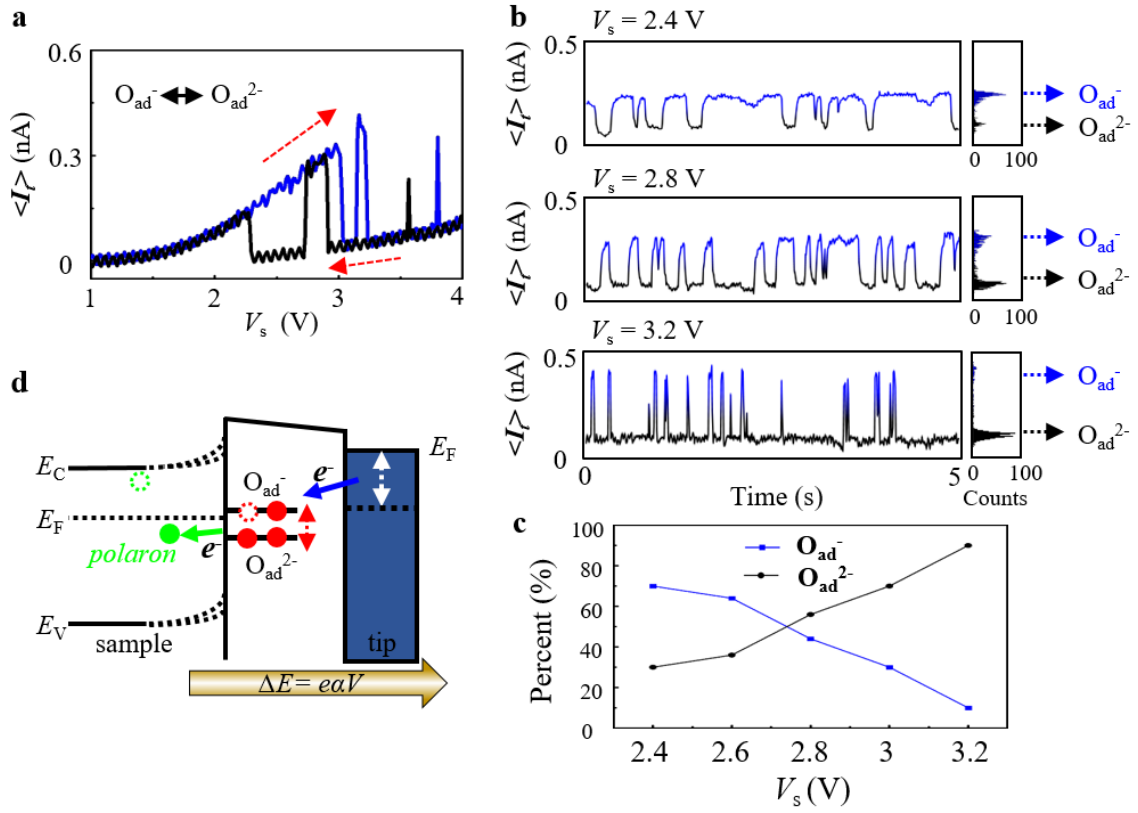

Figure 7.4 Dependence of the conductance hysteresis on the O_{ad} charge state switching between O_{ad}^- and O_{ad}^{2-} by sweeping the bias voltage. a Time-averaged tunneling current $<I_t>$ signal recorded on O_{ad}^- by sweeping the positive bias voltage between 1 V and 4 V with duration of 1 s. b Time traces and corresponding histograms of the $<I_t>$ measured on O_{ad}^- at different bias voltages of 2.4 V, 2.8 V and 3.2 V, respectively. C Quantitative analysis of the charge and conductance

states transition of the oxygen species. d Corresponding schematic diagram of charge state and conductance hysteresis by ramping the bias voltage with electron transferring between tip, O_{ad} and polaron in substrate.

After demonstrating the unidirectional charge and conductance states switching of single O_{ad}, we now explore a reversible charge and conductance hysteresis between high and low states simply by sweeping the bias voltage in the positive range with a constant tip-sample distance. In Figure 7.4(a), an interesting $<I_t>(V_s)$ spectrum is observed while sweeping bias voltage on O_{ad}^- between 1 V and 4 V with duration of 1 s. Here the conductance hysteresis between high and low states is observed in both forward and backward curves, which is believed to be due to the charge state switching between O_{ad}^- and O_{ad}^{2-}. To obtain insight into such conductance hysteresis, the $<I_t>$ signal as a function of time is monitored in real time with the given residence bias voltages, as shown in Figure 7.4(b). The random telegraph-like tunneling current signal always switches between two well-defined states, and no other conductance state can be recorded, which clearly indicates the stochastic switching dynamics of two conductance states due to the charge state transition between O_{ad}^- and O_{ad}^{2-}. The current-trace histograms show the prominent bimodal distribution, exactly indicating the fractional occupation of high (P_H) and low (P_L) conductance states, which corresponds to the O_{ad}^- and O_{ad}^{2-} charge states, respectively. It is noticed that, with the residence bias voltage increasing from 2.4 V to 3.2 V, the P_L is gradually growing at the expense of P_H, which indicates that the O_{ad}^{2-} becomes the dominant specie at relatively high bias voltage, as presented in Figure 7.4(c). Based on our experimental results, we propose that such kind of conductance hysteresis of single O_{ad} induced by charge state transition can be tentatively explained by the electrons transfer between the conductive tip, O_{ad} and polaron in rutile TiO_2(110), as the schematic model shown in Figure 7.4(d). As mentioned above, in this reversible

charge and conductance states transition, the tip-induced local electric field (ΔE) plays a key role in tuning the tunneling barrier and modulating the electrons transferring behavior, in which the magnitude is exclusively governed by the tip-sample distance (the level arm, α) and bias voltage (V). [1,22] In the conductance transition from high to low state, when reaching the threshold bias voltage, the tunneling electrons can be injected from the conductive tip to the O_{ad}, resulting in the O_{ad} charge state transition from O_{ad}^{-} to O_{ad}^{2-}, which is electrically activated by the local electric field. As previously discussed, the fully charged O_{ad}^{2-} is the ground state specie that hinders further electrons injection. Meanwhile, with further increasing the bias voltage, the magnitude of the local electric field is continually enhanced, resulting in the electrons transferring from O_{ad} to the substrate polaron, that is, the O_{ad} discharging from O_{ad}^{2-} to O_{ad}^{-}, and in the meantime the conductance switching from low to high state. The conductance hysteresis induced by reversible charging and discharging process of single O_{ad} can be continuously activated during bias voltage sweeping, in which the polaron in rutile TiO_2(110) can serve as an efficient electron reservoir to crucially modulate the charge and conductance behaviors of the adosrbates.

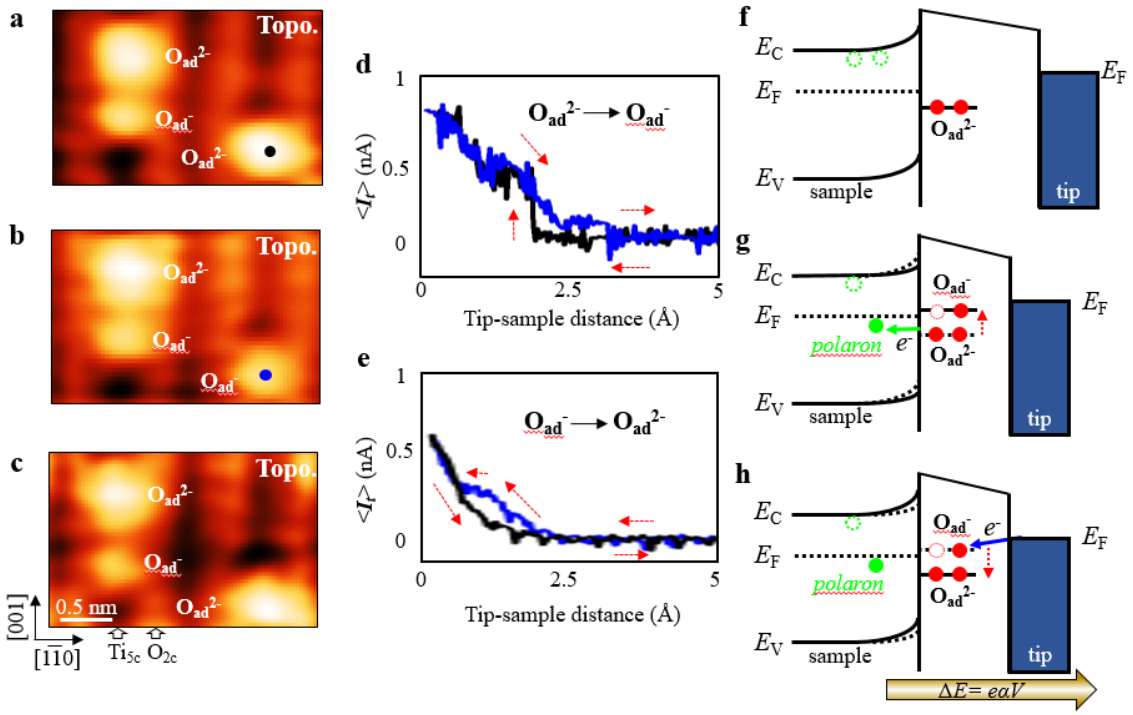

Figure 7.5 Dependence of the conductance switching of O_{ad} on its charge state transition between O_{ad}^{2-} and O_{ad}^{-} by sweeping the tip-sample distance. a-c Topographic nc-AFM images (hole mode, 2.55×1.6 nm^2) of O_{ad} before and after sweeping the tip-sample distance. d and e Tunneling current $<I_t>$ signals recorded on O_{ad}^{2-} and O_{ad}^{-} by sweeping the tip-sample distance with sweeping time of 1 s, as the black and blue dots indicated in a-c, respectively. f-h Corresponding schematic energy diagrams by sweeping the tip-sample distance. Imaging parameters: f_0 = 807 kHz, A = 500 pm, Q = 21460, T = 78 K, V_s = + 1 V.

To round off our discussion about the O_{ad} charge and conductance states transition activated by the tip-induced local electric field, we have further demonstrated that the charge and conductance states transition of single O_{ad} can also be deliberately manipulated by sweeping the tip-sample distance, as show in Figure 7.5. In this transition process, the tip-induced local electric field (ΔE) is controllably modulated by the tip-sample distance (the level arm, α) with a constant positive

bias voltage. We demonstrate that the single O_{ad}^{2-} can be discharged to O_{ad}^{-}, and re-charged back to O_{ad}^{2-} by sweeping the tip-sample distance, as shown in Figure 7.5(a-c). During tip-sample distance sweeping, the $<I_t>$ singles are recorded in real-time, as shown in Figure 7.5(d,e). In the discharging (charging) process, a sudden discontinuity in the forward tunneling current trace is observed, which clearly indicates a conductance transition from low to high (from high to low) state due to the single O_{ad} charge state switching from O_{ad}^{2-} to O_{ad}^{-} (from O_{ad}^{-} to O_{ad}^{2-}). This charge state switching accompanied with conductance state transition can still be tentatively explained by the electrons transferring between tip, O_{ad} and polaron in rutile TiO_2(110). as the corresponding schematic diagrams shown in Figure 7.5(f-h). With the decreased tip-sample distance (increased α), the magnitude of the tip-induced local electric field is enhanced, which can result in the electrons transferring from the O_{ad} to the polaron in the substrate (discharging process, Figure 7.5(g)), or from the conductive tip to the O_{ad} (charging process, Figure 7.5(h)). Note that a relatively longer tip-sample distance is swept to discharge the single O_{ad} than that to charge O_{ad}, which indicates a higher energy barrier to discharge O_{ad}^{2-}. This is in line with our previous discussion that the O_{ad}^{2-} is demonstrated to be the energetically more favorable specie. [1] Specifically, we stress here that the yield ratio of such charge induced conductance transition by sweeping bias voltage and tip-sample distance can be affected by many factors, for example, the inhomogeneous distribution of polaronic defects, [23] the nearby adsorbed atoms [24] and the tip apex termination. [25] We believe that this conductance transition behavior induced by charge states switching at single atom level deserves further investigation, both experimentally and theoretically.

7.4 Conclusion

In this study, we have systematically investigated the charge and conductance states of single O_{ad} chemisorbed on rutile TiO_2(110) surface by simultaneous low temperature nc-AFM and STM measurement at 78 K. The multiple charge states of the chemisorbed O_{ad} on rutile TiO_2(110), namely, the O_{ad}^- and O_{ad}^{2-} species, are unprecedentedly probed and distinguished by STM with atomic resolution, in which we speculate that the polarons in rutile TiO_2(110) is dominantly responsible for the multiple charge states stabilization. Moreover, we clearly demonstrate that the atomic O_{ad} conductance state exclusively depends on its charge state, that is, the O_{ad}^- shows relatively higher conductance than O_{ad}^{2-}, based on the simultaneous nc-AFM and STM probing in constant height mode in combination with the tunneling current measurement as a function of bias voltage and tip-sample distance. In addition, we also demonstrate our ability to reversibly switch the O_{ad} conductance between high and low states by deliberately controlling its charge state by means of sweeping the bias voltage and tip-sample distance. The conductance hysteresis of single O_{ad} between high and low states is observed during bias voltage sweeping, and alternatively, the reversible conductance transition of the O_{ad} can be stepwise achieved by sweeping the tip-sample distance, which is all attributed to the charge state switching between O_{ad}^- and O_{ad}^{2-}. We stress that the polarons in rutile TiO_2(110) play a vital role in the reversible charge/conductance states transition process by accepting the electrons from the charged O_{ad}, which is electrically activated by the tip-induced local electric field. We believe that our work provides a pioneering study about the charge induced conductance switching of the chemisorbed adsorbates on semiconductors at single atom level, and can potentially revolutionize the charge transfer related reactions, specifically, the catalytic reactions.

Chapter 8 Unraveling charge state and structural fluxionality of Au nanoclusters on oxidized rutile TiO_2(110) by nc-AFM/KPFM

8.1 Introduction

In this study, we have systematically investigated the geometric and electronic properties of the Au nanoclusters (NCs) dispersed on oxidized rutile TiO_2(110)-(1×1) surface by nc-AFM and KPFM at 78 K. The Au NCs with the dominant diameter of 2~3 nm are found to nucleate homogeneously on the terraces. By using simultaneous nc-AFM and KPFM characterization with atomic resolution, we clearly demonstrate that the Au NCs supported on O-TiO_2(110) surface are positively charged, indicating the charge transfer from the Au NCs to the oxidized substrate. In addition, the V_{LCPD} of the Au NCs exhibit strong size dependence, and the effect of the substrate direction on the V_{LCPD} distribution within single Au NCs are discussed. Besides the investigation of the electronic properties of the Au NCs, the reversible structural fluxionality of the Au NCs is experimentally demonstrated for the first time by consecutive nc-AFM characterization with atomic resolution.

8.2 Experimental methods

Simultaneous nc-AFM and KPFM measurements were performed in constant height mode to avoid the crosstalk between topographic and electronic signals, in which the bias voltage

feedback approach was used to record the V_{LCPD}. The bias voltage is applied to sample with respect to the tip. When the clean sample was cooled down to room temperature (RT), it was exposed to the oxygen gas (purity > 99.9%, 0.6 L) to obtain the oxidized rutile TiO_2(110). After the pressure decreased to 5×10^{-11} Torr, the Au atoms were deposited onto the oxidized TiO_2(110) surface at RT, in which a home-built crucible heated by Ta wires was employed to evaporate the Au (purity > 99.9%, 0.1 ML). During Au atoms deposition, the pressure was kept below 1×10^{-10} Torr.

8.3 Results and discussion

8.3.1 Clarification of the charge state of Au NCs on oxidized rutile TiO_2

We first investigate the topographic features of the Au NCs dispersed on O-TiO_2(110)-(1 × 1) surface by nc-AFM measurement. In Figure 8.1(a,b), many bright spots are characterized with mainly the hemispherical shape homogeneously distributed on the terrace, and we can distinguish these bright spots as the Au NCs with different size. The size distribution (diameter) of the Au NCs is summarized in Figure 8.1(c), which is recorded rigorously from the cross-sectional measurement along the [1-10] direction. It is shown that the size of the Au NCs is mainly distributed at 2~3 nm, which has been demonstrated as the optimized size with the highest catalytic activity for CO oxidations at low temperatures. [1,2,3] Some experimental studies in combination with theoretical simulation have proposed that the O_{ad}, rather than the surface defects, [4,5] serves as the nucleation sites for the Au NCs on O-TiO_2(110) surface. [6] Therefore, we speculate that some O_{ad} are potentially incorporated in to the Au NPs, which will probably result in the formation of Au-O bond. In addition, we stress here that no spontaneous movement or configurational change of the Au NCs is observed during normal scanning, indicating the extraordinary stability and strong adhesion properties of the Au NCs on oxidized support possibly

because of the Au-O bond, which is perfectly consistent with previous studies. [6]

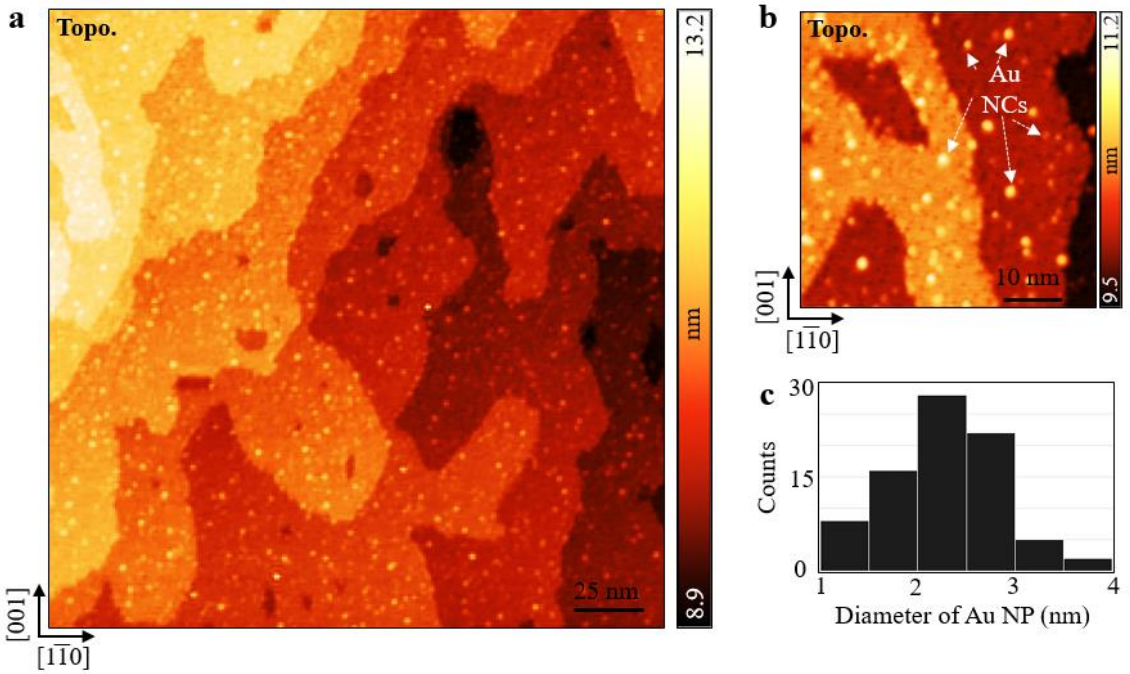

Figure 8.1 Characterization of Au nanoclusters (NCs) adsorbed on oxygen-rich rutile TiO_2(110)-(1 × 1) surface (O-TiO_2). (a,b) Topographic nc-AFM image of Au NCs adsorbed on O-TiO_2 surface (image size: 240× 240 nm^2 and 50× 50 nm^2). (b) Size distribution of Au NCs measured along the [1-10] direction. Imaging parameters: f_0 = 805 kHz, A = 500 pm, Q = 14300, T = 78 K, Δf = -27 Hz.

After studying the structural properties of the Au NCs on O-TiO_2, we now turn to the investigation of its electronic properties. The simultaneously recorded nc-AFM and KPFM images of the Au NCs on O-TiO_2 in constant height mode are shown in Figure 8.2(a,b), in which the adsorbed O_{ad} and the Au NCs can be clearly distinguished with atomic resolution, respectively. In order to get more information of the adsorbates, the line profiles of frequency shift (Δf) and V_{LCPD} of the O_{ad} and Au NCs are obtained, as shown in Figure 8.2(c,d). We can observe that the

O_{ad}^{-} and O_{ad}^{2-} can all be characterized as the bright protrusions, and the O_{ad}^{2-} always shows brighter contrast than O_{ad}^{-} in both nc-AFM and KPFM images, which is consistent with our previous works. [7] Here, as we have demonstrated experimentally and theoretically, the brighter nc-AFM and KPFM image contrast of the O_{ad}^{2-} than that of O_{ad}^{-} can be attributed to the strong attractive force and more charge localized on O_{ad}^{2-} than that on O_{ad}^{-}. [7] Interestingly, the Au NCs are characterized as brightest protrusions in nc-AFM image because of the strongest attractive force. While it is recorded as the dark depressions in the corresponding KPFM image, indicating the lower V_{LCPD} of the Au NCs than that of the O-TiO_2 surface. In this regard, as we have clearly demonstrated before that the O_{ad} with bright contrast in KPFM image are negatively charged by the excess electrons from the surface defects and polarons, [7] here the dark contrast of the Au NCs in KPFM image strongly suggests that the Au NCs on O-TiO_2 surface are positively charged, which clearly demonstrates the charge transfer formation from the Au NCs to the oxidized substrate. We stress here that the simultaneously recorded topography and V_{LCPD} of the Au NCs are obtained with long tip-sample distance, completely excluding the possibility of the tip-induced dipole effect on the V_{LCPD} measurement. [8,9] Our study clearly demonstrates the cationic Au NCs species on O-TiO_2 surface, and provides the convincing evidence to prove the charge transfer from the Au NCs to the oxidized substrate.

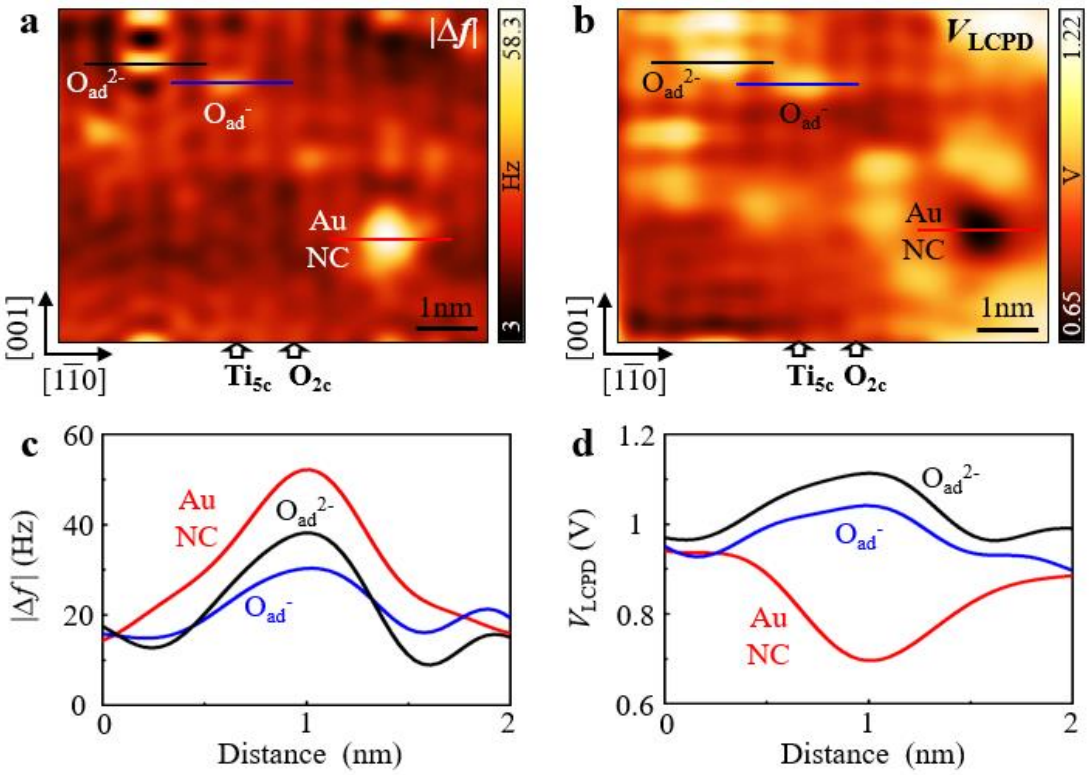

Figure 8.2 Clarification of the charge state of Au NC adsorbed on O-TiO_2 by simultaneous nc-AFM and KPFM measurement. (a, b) Simultaneously measured $|\Delta f|$ (nc-AFM, hole mode, 5.4 × 7 nm^2) and V_{LCPD} (KPFM, 5.4 × 7 nm^2) images of Au NC adsorbed on O-TiO_2 surface in constant height mode. O_{2c}: 2-fold coordinated bridging oxygen row. Ti_{5c}: 5-fold coordinated titanium row. O_{ad}^- and O_{ad}^{2-}: single oxygen adatom charged with one and two electrons on Ti_{5c} row. (c, d) Corresponding line profiles of $|\Delta f|$ and V_{LCPD} of the O_{ad}^-, O_{ad}^{2-} and Au NC as the solid black, blue and red lines indicated in (a, b), respectively. Imaging parameters: f_0 = 805 kHz, A = 500 pm, Q = 14300, T = 78 K, Δf = -39 Hz, V_{ac} = + 0.5 V, f_{ac} = 170 Hz.

The dependence of the V_{LCPD} of Au NCs on its size is demonstrated by KPFM characterization of the larger area with a large tip-sample distance, as shown in Figure 8.3. The Au NCs can be characterized as the bright protrusions with various size and inhomogeneous shape in nc-AFM image and as the dark depressions in the corresponding KPFM, which shows good agreement

with our experimental results in Figure 8.2. In general, one can notice that the Au NPs with larger configurational size shows the darker contrast, namely, the relatively smaller V_{LCPD}, indicating the size effect on the V_{LCPD} of the dispersed Au NCs on O-TiO_2 surface. In order to shed more light onto the size dependence of the V_{LCPD}, the V_{LCPD} values of each Au NCs in Figure 8.3(b) are summarized as a function of its diameter measured along [1-10] direction, as shown in Figure 8.3(c). Besides the size dependence of the V_{LCPD}, one can observe that some quantitative fluctuation of the V_{LCPD} values of some Au NCs with similar size exists, which can be potentially attributed to the inhomogeneous structural configuration, [10] the chemisorbed O_{ad} incorporated in the Au NCs [6] and the subsurface defects on the substrate. [11] Our experimental results demonstrate that the charge transfer is always formed from the supported Au NCs to the oxidized substrate, resulting in the cationic Au species, and the V_{LCPD} shows strong dependence on the size of the Au NCs.

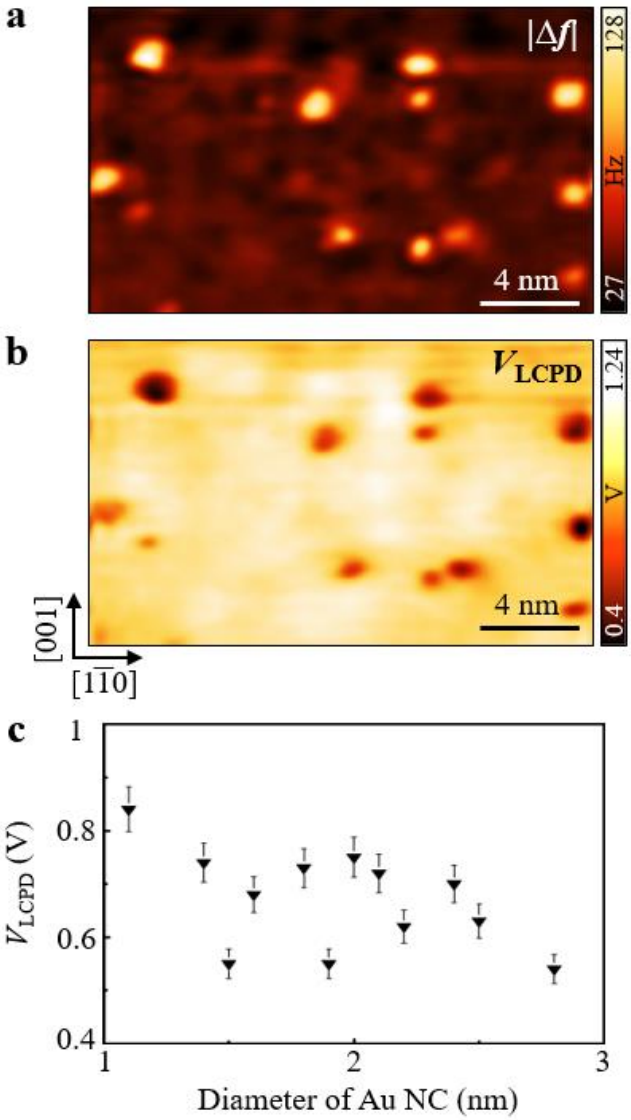

Figure 8.3 Dependence of the Au NCs V_{LCPD} on the size. (a, b) Simultaneous measurement of $|\Delta f|$ (nc-AFM, 12 × 20 nm^2) and V_{LCPD} (KPFM, 12 × 20 nm^2) images of Au NCs adsorbed on O-TiO_2 surface in constant height mode. (c) V_{LCPD} of Au NCs as a function of the diameters with the measurement along [1-10] direction. Error bar in (c) is ± 5 %. Imaging parameters: f_0 = 805 kHz, A = 500 pm, Q = 14300, T = 78 K, Δf = -45 Hz, V_{ac} = + 0.5 V, f_{ac} = 170 Hz.

It is important to stress here that we find the V_{LCPD} distribution of the Au NCs is possibly affected by the substrate direction. Figure 8.4 shows the simultaneous nc-AFM and KPFM measurement

of the Au NCs on O-TiO_2 surface, and the Au NCs are characterized as bright protrusions in nc-AFM image and dark depressions in the corresponding KPFM images, which is consistent with our experimental results in Figures 8.2 and 8.3. Interestingly, we find that some Au NCs show different configurational shapes in their topographic and electronic characterization. For example, the No.1 and 2 Au NCs indicated by dashed red circles show the preferential configuration shape along the along [1-10] and [001] directions, respectively, both in nc-AFM and KPFM images. However, for the No.3-5 Au NCs, they exhibit the preferential configuration shape along [001] direction in the nc-AFM image, while along the [1-10] direction in the corresponding KPFM image, as the dashed green circles indicated. Here we tentatively propose that the interface perimeter of some Au NCs along the [1-10] and [001] directions exhibit different electronic properties, which is possibly attributed to the different Au-Au coordination and charge distribution of the Au atoms depending on the substrate direction. [12] Note that such specific substrate direction dependence of the V_{LCPD} distribution is independent of the size of Au NCs. On the other hand, the No.6 Au NC in Figure 8.4 is characterized as the brightness protrusion in nc-AFM image, while as the weak dark depression with similar configuration in KPFM image. Such mismatch between nc-AFM and KPFM contrast can be attributed to the negatively charged O_{ad} incorporated in the Au NC, resulting in the charge transfer from the Au NC to the O_{ad}. [6,13,14] Therefore, the effect of whether the adsorbed O_{ad} incorporated in the Au NCs on the aforementioned specific V_{LCPD} distribution can be clearly excluded, and the most possible factor is the TiO_2 substrate direction that possibly governs the V_{LCPD} distribution of the Au NCs to some extent.

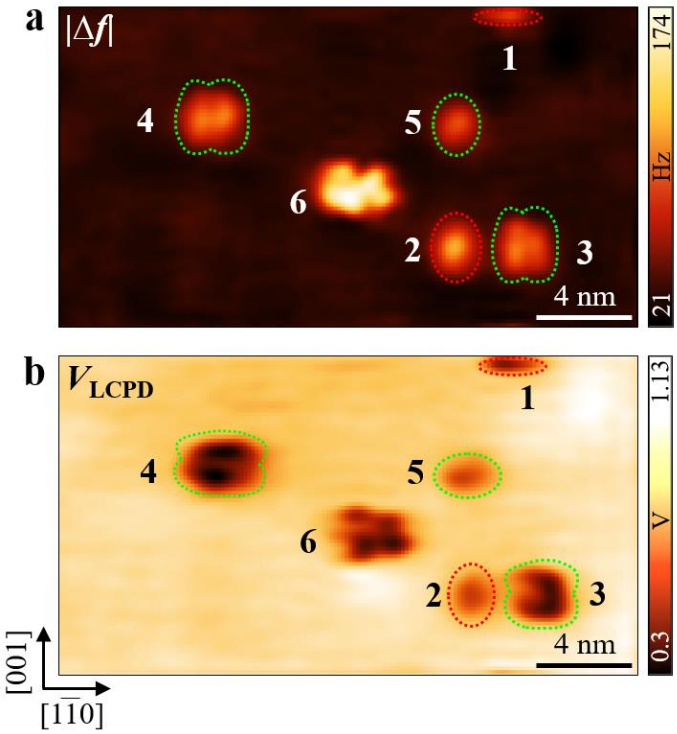

Figure 8.4. Investigation of the dependence of the Au NCs charge distribution on the Au NC configuration and substrate direction. (a, b) Simultaneously recorded $|\Delta f|$ (nc-AFM, 6.6 × 12 nm^2) and V_{LCPD} (KPFM, 6.6 × 12 nm^2) images of Au NCs adsorbed on O-TiO_2 surface in constant height mode. Imaging parameters: f_0 = 805 kHz, A = 500 pm, Q = 14300, T = 78 K, Δf = -55 Hz, V_{ac} = + 0.5 V, f_{ac} = 170 Hz.

8.3.2 Structural fluxionality of Au NCs on oxidized rutile TiO_2

The geometric properties of the Au NCs, besides the electronic property, are also regarded as the key factor to affect the catalytic activities of the catalyst. The effects of the quantum size, [2] geometric shape [1] and presence of under-coordinated Au atoms [15] of the Au NCs on the catalytic reactions have been fully investigated, both experimentally and theoretically. Specifically, the structural fluxionality of the Au NCs has been theoretically proposed to allow the catalytic reactions to evolve on the most favorable free-energy path because of the formation

of Au NCs with different structures and chemical activities in an equilibrium state. [16,17] In this regard, we next explore the structural fluxionality of the Au NCs on O-TiO_2 surface in a completely controllable and reversible manner.

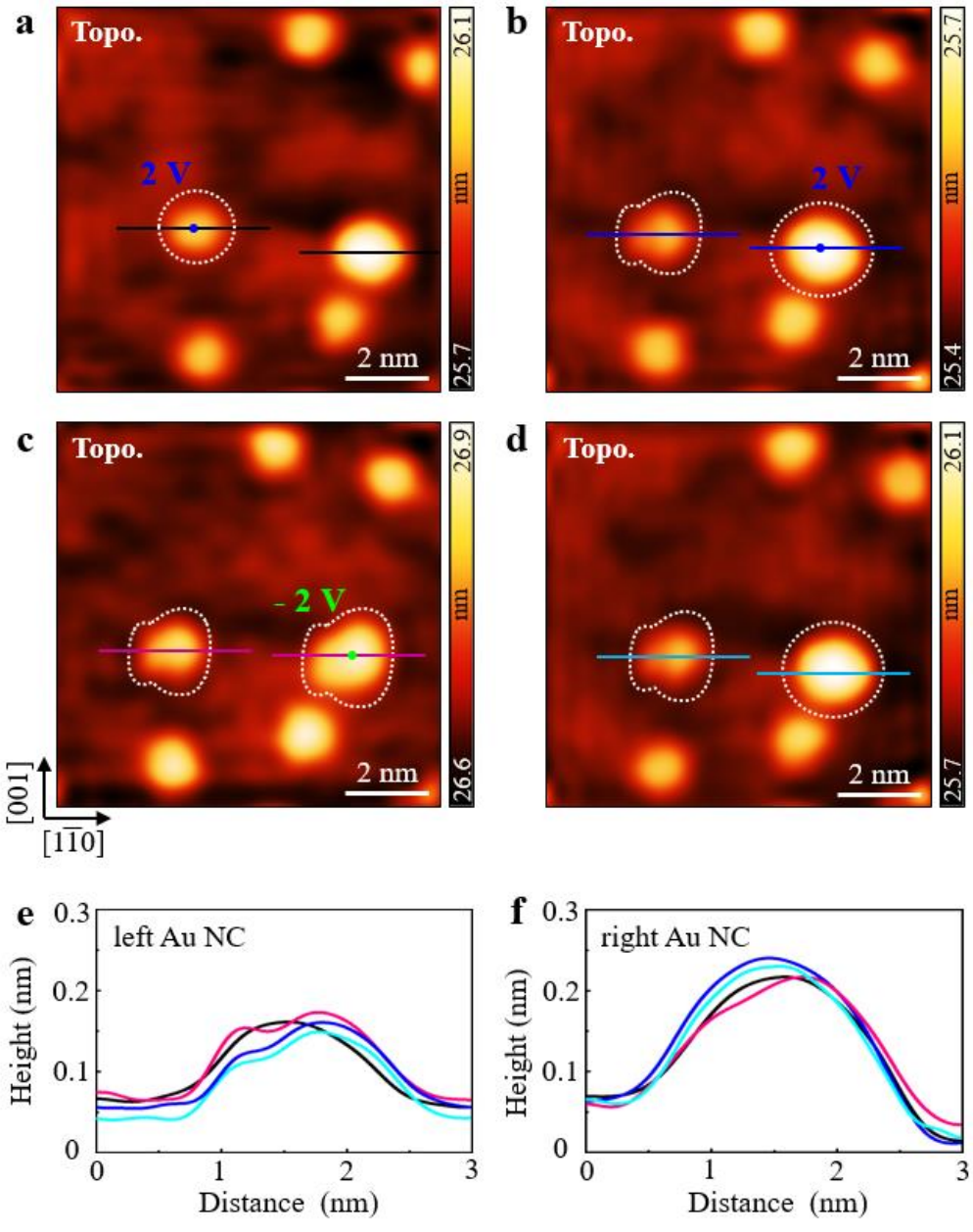

Figure 8.5. Reversible conformational change of Au NCs activated by the voltage pulse. (a-d) Topographic nc-AFM images (9 × 9 nm^2) of Au NCs adsorbed on O-TiO_2 surface. (e, f)

Corresponding line profiles of the Au NCs on left and right sides as the solid lines indicated in (a-d), respectively. Blue and green dots in (a-c) indicate the positive and negative voltage pulse sites with duration of 0.5 s, respectively. Imaging parameters: f_0 = 805 kHz, A = 500 pm, Q = 14300, Δf = -51 Hz, T = 78 K, V_s = + 1.2 V.

The reversible structural fluxionality of the Au NCs on O-TiO_2 surface is presented in Figure 8.5. In general, the topographic structures of the Au NCs are always characterized as the hemispherical protrusions with single peak, as shown in Figure 8.5 (a), which is consistent with previous works. [1,2,6] In order to induce the structural fluxionality, a positive voltage pulse of 2 V with duration of 0.5 s is applied on top the Au NCs, and then the Au NCs are transformed from the hemispherical shape to the double-peak configuration, as the dashed bright circles indicated in Figure 8.5a-c. Interestingly, when a negative voltage pulse of -2 V with duration of 0.5 s is applied on the Au NCs with double-peak configuration, the Au NC can be transformed back to the hemispherical shape with single peak, as shown in Figure 8.5(c-d). The reversible structural fluxionality of the Au NCs can be clearly observed and analyzed from the corresponding line profiles in Figure 8.5(e,f), which also suggests that the total volume dose of single manipulated Au NCs keeps constant in the structural fluxionality process. It is noticed that, during normal scanning, we did not observe any spontaneous movement or structural transformation of the Au NCs with both hemispherical and double-peak shapes, indicating the high stability of these two configurations. [6,16] Note that the voltage pulse is applied with a long tip-sample distance, which can prevent the tunneling electrons flowing during voltage pulse. [11] For this reason, we stress here that it is the structure manipulation, without any charge state transformation of the Au NCs during the structural fluxionality. [18] In addition, we did not observe any other geometric structures of the Au NCs in the reversible structural fluxionality, and the theoretical calculation is necessary to

figure out the energy-stable geometric structures. We think the most possible mechanism that responsible for the structural fluxionality in our experiment is the local electric field automatically formed during voltage pulse, which serves as an external stimulus to activate the rearrangement of the Au atoms in an equilibrium state. [16,19,20] One can anticipate that the threshold voltage pulse for such structural fluxionality strongly depends on the size of Au NCs and the tip-sample distance, for which more experimental works are ongoing now.

8.4 Conclusion

In this study, we have clearly demonstrated the charge state and structural fluxionality of the Au NCs dispersed on O-TiO_2(110)-(1 × 1) surface by nc-AFM and KPFM measurement at 78 K. Firstly, by simultaneously characterizing the Au NCs and the chemisorbed O_{ad} in KPFM image with atomic resolution, we clearly clarify that the Au NCs are positively charged species, which provides sufficient evidence to support the charge transferring from Au NCs to the oxidized substrate. In addition, we demonstrated that the V_{LCPD} of the Au NCs exhibits the size dependence, namely, the smaller Au NCs show relatively lower V_{LCPD}. Quantitatively, the V_{LCPD} fluctuation of some Au NCs with similar size can be potentially attributed to the inhomogeneous structural configuration, the chemisorbed O_{ad} incorporated in the Au NCs and the subsurface defects on the substrate. Moreover, we found some Au NCs show preferential configuration shape along [001] direction in the nc-AFM image, while along the [1-10] direction in the corresponding KPFM image, and here we tentatively propose that the substrate direction may affect the charge distribution of the Au NCs. On the other hand, we qualitatively demonstrate the reversible structural fluxionality of the Au NCs, which is activated by the voltage pulse with opposite polarities. We think the local electric field is most likely responsible for the structural fluxionality,

without any charge state manipulation or displacement of the Au NCs. Our study provides convincing experimental evidence to clarify the electronic and geometrical properties of the noble metal catalyst, and is applicable to numerous other catalytic models based on noble metal nanoparticles.

Chapter 9 Summary and outlook

9.1 Summary

In this doctoral dissertation, I systematically investigated and manipulated the geometric and electronic properties of the reaction components, such as the point defects, oxygen adatoms and Au nanoclusters on rutile TiO_2(110) surface by using noncontact atomic force microscopy and Kelvin probe force microscopy at 78 K under ultra-high vacuum condition, which can contribute to explaining and controlling the catalytic reactions based on the noble metal catalysts on transition metal oxides. Firstly, we found and demonstrated that the subsurface hydrogen on rutile TiO_2(110) can be characterized with atomic resolution by using simultaneous noncontact atomic force microscopy and scanning tunneling microscopy imaging method. Four different configurations of the subsurface hydrogen were observed. In addition, we demonstrated that the subsurface hydrogen can be reversibly migrated between the surface and subsurface layers for the first time, which is electrically activated by the voltage pulse with different polarities. Secondly, the charge states of the oxygen adatoms adsorbed on rutile TiO_2(110) surface were experimentally clarified for the first time at the atomic scale level, and oxygen adatoms charged by one and two electrons were distinguished with different image contrast. Our assignment of the different charge states of the oxygen adatoms were in consistent with the measurement of short range force and V_{LCPD} as a function of tip-sample distance. Moreover, several manipulation methods are proposed to switch the charge states of oxygen adatoms with single electron sensitivity in a controllable manner, such as changing the tip-sample distance and the bias voltage. Thirdly, we investigated the conductance states of the oxygen adatoms by using noncontact atomic force microscopy and scanning tunneling microscopy at the single atom level. We demonstrate that the conductance

behavior of the oxygen adatoms exclusively depends on its charge states, namely, the oxygen adatoms charged by one electron showed higher conductance state than that charged by two electrons. Specifically, the conductance behavior of the oxygen adatoms can be reversibly switched between high and low conductance states by controlling its charge states transition. Lastly, the charge transfer between the Au nanoclusters and oxygen adatoms was experimentally demonstrated using the simultaneous measurement of nc-AFM and KPFM in constant height mode, and the charge state of the Au nanoclusters on oxidized TiO_2(110) surface are experimentally demonstrated to be positively charged. In addition, the structural fluxionality of the Au nanoclusters is experimentally demonstrated with atomic resolution for the first time. Our work provides a systematic investigation and manipulation of the geometric and electronic properties of the catalytic reactions components with atomic resolution, and can contribute to the understanding and controlling of the catalytic reactions based on noble metal catalysts on transition metal oxides.

9.2 Outlook

Our work provides crucial information on understanding and controlling the catalytic reactions by characterizing and manipulating the geometric and electronic properties of the reaction components at the atomic scale levels. Yet, more experimental works should be performed to further investigate the catalytic mechanism of the catalytic reactions. For example,

(1) The geometric and electronic properties of CO molecules on oxidized rutile TiO_2(110) should be investigated at the atomic level.

(2) The dynamic charge state transition of the reactants, such as Au nanoclusters, CO and oxygen species, in the Au/TiO_2 catalytic reactions should be demonstrated experimentally.

References

Chapter 1

1. Kolasinski, K. W., John Wiley & Sons, **2012**.
2. Diebold, U., *Surface science reports* **2003**, *48*, 53-229.
3. Wisniak, J., *Educación química* **2010**, *21*, 60-69.
4. Yeager, E., *Journal of Molecular Catalysis* **1986**, *38*, 5-25.
5. Fu, Q., Li, W.X., Yao, Y., Liu, H., Su, H. Y., Ma, D., Gu, X. K., Chen, L., Wang, Z., Zhang, H. and Wang, B., *science* **2010**, *328*, 1141-1144.
6. Gallon, B. J., Kojima, R. W., Kaner, R. B. and Diaconescu, P. L., *Angewandte Chemie International Edition* **2007**, *46*, 7251-7254.
7. Ollis, D. F. and Turchi, C., *Environmental progress* **1990**, *9*, 229-234.
8. Peral, J., Domenech, X. and Ollis, D. F., *Journal of Chemical Technology & Biotechnology: International Research in Process, Environmental AND Clean Technology* ***70***, 117-140, 1997.
9. Li, G. and Tang, Z., *Nanoscale* **2014**, *6*, 3995-4011.
10. Dong, Z., Le, X., Li, X., Zhang, W., Dong, C. and Ma, J. *Applied Catalysis B: Environmental* **2014**, *158*, 129-135.
11. Harriman, A., Pickering, I. J., Thomas, J. M. and Christensen, P. A., *Journal of the Chemical Society, Faraday Transactions 1: Physical Chemistry in Condensed Phases* **1988**, *84*, 2795-2806.
12. Mootabadi, H., Salamatinia, B., Bhatia, S. and Abdullah, A. Z., *Fuel* **2010**, *89*, 1818-1825.
13. Pan, J., Liu, G., Lu, G. Q. and Cheng, H. M., *Angewandte Chemie* **2011**, *123*, 2181-2185.
14. Reddic, J. E., Zhou, J. and Chen, D. A., *Surface science* **2001**, *494*, L767-L772.

15. Martirez, J. M. P., Kim, S., Morales, E. H., Diroll, B. T., Cargnello, M., Gordon, T. R., Murray, C. B., Bonnell, D. A. and Rappe, A. M., *Journal of the American Chemical Society* **2015**, *137*, 2939-2947.

16. [16] Mutuma, B. K., Shao, G. N., Kim, W. D. and Kim, H. T., *Journal of colloid and interface science* **2015**, *442*, 1-7.

17. Wang, D., Huang, J., Liu, F., Xu, X., Fang, X., Liu, J., Xie, Y. and Wang, X., *Catalysis Today,* **2019**.

18. Binnig, G., Rohrer, H., Gerber, C. and Weibel, E., *Physical review letters **49***, 57, 1982.

19. Binnig, G., Quate, C. F. and Gerber, C., *Physical review letters* **1986**, *56*, 930.

20. Morita, S., Giessibl, F. J., Meyer, E. and Wiesendanger, R. eds., *Noncontact atomic force microscopy* Springer, **2015**.

21. Sugimoto, Y., Abe, M., Hirayama, S., Oyabu, N., Custance, Ó. and Morita, S., *Nature materials* **2005**, *4*, 156.

22. Custance, O., Perez, R. and Morita, S., *Nature nanotechnology* **2009**, *4*, 803.

23. Kawai, S., Foster, A. S., Canova, F. F., Onodera, H., Kitamura, S. I. and Meyer, E., *Nature communications* **2014**, *5*, 4403.

24. Ternes, M., Lutz, C. P., Hirjibehedin, C. F., Giessibl, F. J. and Heinrich, A. J., *Science* **2008**, *319*, 1066-1069.

25. Gross, L., Mohn, F., Liljeroth, P., Repp, J., Giessibl, F. J. and Meyer, G., *Science* **2009**, *324*, 1428-1431.

26. Steurer, W., Repp, J., Gross, L., Scivetti, I., Persson, M. and Meyer, G., *Physical review letters* **2015**, *114*, 036801.

27. Repp, J., Meyer, G., Olsson, F. E. and Persson, M., *Science* **2004**, *305*, 493-495.

28. Kocić, N., Weiderer, P., Keller, S., Decurtins, S., Liu, S. X. and Repp, J., *Nano*

letters **2015**, *15*, 4406-4411.

29. Okamoto, K., Yoshimoto, K., Sugawara, Y. and Morita, S., *Applied surface science* **2003**, *210*, 128-133.

30. Ma, Z. M., Kou, L., Naitoh, Y., Li, Y. J. and Sugawara, Y., *Nanotechnology* **2013**, *24*, 225701.

31. Takeuchi, O., Ohrai, Y., Yoshida, S. and Shigekawa, H., *Japanese Journal of Applied Physics* **2007**, *46*, 5626.

32. Wen, H. F., Li, Y. J., Arima, E., Naitoh, Y., Sugawara, Y., Xu, R. and Cheng, Z. H., *Nanotechnology* **2017**, *28*, 105704.

33. Sawada, D., Sugimoto, Y., Morita, K. I., Abe, M. and Morita, S., *Applied Physics Letters* **2009**, *94*, 173117.

Chapter 2

1. Binnig, G. and Rohrer, H. *Surface science* **1983**, *126*, 236-244.

2. Binnig, G.; Quate, C. F. and Gerber, C. *Physical review letters* **1986**, *56*, 930.

3. Bolshakova, A. V.; Kiselyova, O. I.; Filonov, A. S.; Frolova, O. Y.; Lyubchenko, Y. L. and Yaminsky, I. V. *Ultramicroscopy* **2001**, *86*, 121-128.

4. Giessibl, F. J. *Reviews of modern physics* **2003**, *75*, 949.

5. Moreno-Herrero, F.; Colchero, J.; Gomez-Herrero, J. and Baro, A. M. *Physical Review E* **2004**, *69*, 031915.

6. Giessibl, F. J. and Bielefeldt, H. *Physical Review B* **2000**, *61*, 9968.

7. Martin, Y.; Williams, C. C.; Wickramasinghe, H. K. *Journal of Applied Physics* **1987**, *61*, 4723-4729.

8. Albrecht, T. R.; Grütter, P.; Horne, D. and Rugar, D. *Journal of Applied Physics* **1991**, *69*, 668-673.

9. Morita, S.; Giessibl, F. J.; Meyer, E. and Wiesendanger, R. *Springer*, **2015**, ***3***.

10. Saint Jean, M.; Hudlet, S.; Guthmann, C. and Berger, J. *Journal of Applied Physics* **1999**, *86*, 5245-5248.

11. Giessibl, F. J. *Review of Modern Physics* **2003**, *75*, 949-983.

12. Olsson, L.; Lin, N.; Yakimov, V. and Erlandsson, R. *Journal of Applied Physics* **1998**, *84*, 4060-4064.

13. Albrecht, F.; Repp, J.; Fleischmann, M.; Scheer, M.; Ondracek, M. and Jelinek, P. *Phys. Rev. Lett*. **2015**, *115*, 076101.

14. Sader, J. E. and Jarvis, S. P. *Applied Physics Letters* **2004**, *84*, 1801-1803.

15. Giessibl, F. J. Applied Physics Letters **2000**, *76*, 1470-1472.

16. Lang, N. D. and Kohn, W. *Physical Review B* **1970**, *1*, 4555-4568.

17. Kobayashi, K.; Yamada, H. and Matsushige. K. *Rev. Sci. Instrum*. **2009**, *80*, 043708.

18. Giessibl, F. J.; Pielmeier, F.; Eguchi, T.; An, T. and Hasegawa, Y. *Physical Review B* **2011**, *84*, 1-15.

19. Binnig, G.; Rohrer, H.; Gerber, Ch. and Weibel., E. *Phys. Rev. Lett.* **1982**, *49*, 57-61.

20. Sawada, D.; Sugimoto, Y.; Morita, K. I.; Abe, M. and Morita, S. *Applied Physics Letters* **2009**, *94*, 173117.

21. Cardona, M. and Ley, L. *Springer-Verlag Berlin Heidelberg New York*, **1978**, *26*.

22. Shikler, R.; Meoded, T.; Fried, N.; Mishori, B.; Rosenwaks. Y. *J. Appl. Phys*. **1999**, *86*, 107.

23. Kalinin, S.V.; Gruverman (Eds.), A. Scanning Probe Microscopy, *Springer, New Yor*k, **2007**.

24. Fukuma, T.; Kobayashi, K.; Yamada, H. and Matsushige, K. *Rev. Sci. Instrum.* **2004**, *75*, 4589.

25. Itoh, T., T. Suga. *Journal of Micromechanics and Microengineering* **1995**, 5 231.

26. Tabor, D.; Winterton, R. H. S. *Proceedings of the Royal Society of London. A. Mathematical and Physical Sciences* **1969**, 312, 435-450.

27. Burnham, N. A.; Colton, R. J. *Journal of Vacuum Science & Technology A: Vacuum, Surfaces, and Films* **1989**,7, 2906-2913.

28. Morita, S.; Wiesendanger, R.; Meyer, E. *Springer Berlin Heidelberg New York* **2002**.

29. Lang, N. D. and Kphn, W. *Phys. Rev.* B **1971**, 3, 1215-1223.

30. Arai, T.; Tomitori. M. *Jpn. J. Appl. Phys.* **2000**, 39, 3753-3757.

Chapter 3

1. Darby, A. P. and Pellegrino, S. *Journal of Intelligent Material Systems and Structures* **1997**, *8*, 1001.

2. Watanabe, S. and Fujii, T. *Rev. Sci. Instrum.* **1996**, *67*, 3898-3903.

3. Giessibl, J. and Trafas, B. M. Review of Scientific Instruments **1994**, *65*, 1923-1929.

4. Meyer, G. and Amer., N. M. *Appl. Phys. Lett.* **1990**, *51*, 2089-2091.

5. Yokoyama, K.; Ochi, T.; Uchihashi, T.; Ashino, M.; Sugawara, Y.; Suehira N.; and Morita, S. *Rev. Sci. Instrum*. **2000**, *71*, 128.

6. Fukuma, T.; Kimura, M.; Kobayashi, K.; Matsushige, K.; Yamada, H. *Rev. Sci. Inst.* **2005**, *76*, 053704.

7. Fukuma, T. and Jarvis, S. P. *Rev. Sci. Inst.* **2006**, *77*, 043701.

8. Moreno-Flores, S.; Toca-Herrera, J. L. *CRC Press* **2012**.

Chapter 4

1. Li, M., Hebenstreit, W. and Diebold, U., *Surface science* **1998**, *414*, 951-956.
2. Kou, L.; Li, Y. J.; Kamijyo, T.; Naitoh, Y.; Sugawara, Y. *Nanotechnology* **2016**, 27, 505704.
3. Yim, C. M.; Watkins, M. B.; Wolf, M. J.; Pang, C. L.; Hermansson, K.; Thornton, G. *Phys. Rev. Lett.* **2016**, 117, 116402.
4. Maddox, W. B.; Acharya, D. P.; Leong, G. J.; Sutter, P.; Ciobanu, C. V. *ACS Omega* **2018**, 3, 6540–6545.
5. Cui, X.; Wang, B.; Wang, Z.; Huang, T.; Zhao, Y.; Yang, J.; Hou, J. G. *J. Chem. Phys.* **2008**, 129, 044703.
6. Li, S. C.; Zhang, Z.; Sheppard, D.; Kay, B. D.; White, J. M.; Du, Y.; Lyubinetsky, I.; Henkelman, G.; Dohnálek, Z. *J. Am. Chem. Soc.* **2008**, 130, 9080–9088.
7. Wendt, S.; Matthiesen, J.; Schaub, R.; Vestergaard, E. K.; Lægsgaard, E.; Besenbacher, F.; Hammer, B. *Phys. Rev. Lett.* **2006**, 96, 066107.
8. Minato, T.; Kajita, S.; Pang, C. L.; Asao, N.; Yamamoto, Y.; Nakayama, T.; Kawai, M.; Kim, Y. *ACS Nano* **2015**, 9, 6837–6842.
9. Bikondoa, O.; Pang, C. L.; Ithnin, R.; Muryn, C. A.; Onishi, H.; Thornton, G. *Nat. Mater.* **2006**, 5, 189–192.
10. Acharya, D. P.; Ciobanu, C. V.; Camillone III, N.; Sutter, P. *J. Phys. Chem. C* **2010**, 114, 21510–21515.
11. Tan, S.; Ji, Y.; Zhao, Y.; Zhao, A.; Wang, B.; Yang, J.; Hou, J. G. *J. Am. Chem. Soc.* **2011**, 133, 2002–2009.
12. Matthiesen, J.; Wendt, S.; Hansen, J. Ø.; Madsen, G. K.; Lira, E.; Galliker, P.; Vestergaard, E. K.; Schaub, R.; Lægsgaard, E.; Hammer, B.; Besenbacher, F. *ACS Nano* **2009**, 3, 517–

526.

13. Wahlström, E.; Vestergaard, E. K.; Schaub, R.; Rønnau, A.; Vestergaard, M.; Lægsgaard, E.; Stensgaard, I.; Besenbacher, F. *Science* **2004**, 303, 511–513.

14. Wendt, S.; Sprunger, P. T.; Lira, E.; Madsen, G. K.; Li, Z.; Hansen, J. Ø.; Matthiesen, J.; Blekinge-Rasmussen, A.; Lægsgaard, E.; Hammer, B.; Besenbacher, F. *Science* **2008**, 320, 1755–1759.

15. Lira, E.; Wendt, S.; Huo, P.; Hansen, J. Ø.; Streber, R.; Porsgaard, S.; Wei, Y.; Bechstein, R.; Lægsgaard, E.; Besenbacher, F. *J. Am. Chem. Soc.* **2011**, 133, 6529–6532.

16. Aleksandrov, H. A.; Kozlov, S. M.; Schauermann, S.; Vayssilov, G. N.; Neyman, K. M. *Angew. Chem.* **2014**, 126, 13589–13593.

17. Wen, H. F.; Li, Y. J.; Arima, E.; Naitoh, Y.; Sugawara, Y.; Xu, R.; Cheng, Z. H., *Nanotechnology* **2017**, 28, 105704.

18. Yoon, Y.; Du, Y.; Garcia, J. C.; Zhu, Z.; Wang, Z. T.; Petrik, N. G.; Kimmel, G. A.; Dohnalek, Z.; Henderson, M. A.; Rousseau, R.; Deskins, N.A. *Chem. Phys. Chem.* **2015**, 16, 313–321.

19. Tao, J.; Cuan, Q.; Gong, X. Q.; Batzill, M. *J. Phys. Chem. C* **2012**, 116, 20438–20446.

20. Islam, M. M.; Calatayud, M.; Pacchioni, G. *J. Phys. Chem. C* **2011**, 115, 6809–6814.

21. Yin, X. L.; Calatayud, M.; Qiu, H.; Wang, Y.; Birkner, A.; Minot, C.; Wöll, C. Diffusion versus desorption: complex behavior of H Atoms on an oxide surface. *Chem. Phys. Chem.* **2008**, 9, 253–256.

22. Enevoldsen, G. H.; Pinto, H. P.; Foster, A. S.; Jensen, M. C.; Hofer, W. A.; Hammer, B.; Lauritsen, J. V.; Besenbacher, F. *Phys. Rev. Lett.* **2009**, 102, 136103.

23. Baykara, M. Z.; Mönig, H.; Schwendemann, T. C.; Ünverdi, Ö.; Altman, E. I.; Schwarz, U. D. *Appl. Phys. Lett.* **2016**, 108, 071601.

24. Marinopoulos, A. G., Vilão, R. C., Alberto, H. V., Gil, J. M. *Journal of Physics: Condensed Matter* **2018**, 30, 425503.

25. Yim, C. M.; Watkins, M. B.; Wolf, M. J.; Pang, C. L.; Hermansson, K.; Thornton, G. *Physical review letters* **2016**, 117, 116402.

26. Minato, T.; Sainoo, Y.; Kim, Y.; Kato, H. S.; Aika, K. I.; Kawai, M.; Zhao, J.; Petek, H.; Huang, T.; He, W.; Wang, B. *The Journal of chemical physics* **2009**, 130, 124502.

27. Moses, P. G.; Janotti, A.; Franchini, C.; Kresse, G.; Van de Walle, C. G. *Journal of Applied Physics* **2016**, 119, 181503.

28. Wahlström, E., Vestergaard, E. K., Schaub, R., Rønnau, A., Vestergaard, M., Lægsgaard, E., Stensgaard, I. and Besenbacher, F. *Science* **2004**, 303, 511-513.

29. Tan, S., Ji, Y., Zhao, Y., Zhao, A., Wang, B., Yang, J. and Hou, J. G. *Journal of the American Chemical Society* **2011**, 133, 2002-2009.

30. Du, Y., Deskins, N. A., Zhang, Z., Dohnalek, Z., Dupuis, M. and Lyubinetsky, I., *Physical Chemistry Chemical Physics* **2010**, 12, 6337-6344.

31. Lira, E., Hansen, J. Ø., Huo, P., Bechstein, R., Galliker, P., Lægsgaard, E., Hammer, B., Wendt, S. and Besenbacher, F. *Surface Science* **2010**, 604, 1945-1960.

32. Lu, G.; Linsebigler, A.; Yates Jr, J. T. *J. chem. Phys.* **1995**, 102, 3005-3008.

33. de Lara-Castells, M. P.; Krause, J. L. *Chem. Phys. Lett.* **2002**,354, 483-490.

34. Setvin, M.; Hulva, J.; Parkinson, G. S.; Schmid, M.; Diebold, U. *PNAS* **2017**, 114, 2556-2562.

35. Haruta, M.; Yamada, N.; Kobayashi, T.; Iijima, S. J. *Catal.* **1989**, 115, 301-309.

36. Haruta, M.; Kobayashi, T.; Sano, H.; Yamada, N. *Chem. Lett.* **1987**, 16, 405-408.

37. Hong, S.; Rahman, T. S. *J. Am. Chem. Soc*. **2013**, 135, 7629-7635.

38. Wang, Y. G.; Yoon, Y.; Glezakou, V. A.; Li, J.; Rousseau, R. *J. Am. Chem. Soc.* **2013**, 135,

10673-10683.

39. Yurtsever, A.; Fernández-Torre, D.; Onoda, J.; Abe, M.; Morita, S.; Sugimoto, Y.; Pérez, R. *Nanoscale* **2017**, 9, 5812-5821.

40. Kittel, T.; Roduner, E. *J. Phys. Chem. C* **2016**, 120, 8907-8916.

41. Zhou, X.; Shen, Q.; Yuan, K.; Yang, W.; Chen, Q.; Geng, Z.; Zhang, J.; Shao, X.; Chen, W.; Xu, G.; Yang, X. *J. Am. Chem. Soc.* **2018**, 140, 554-557.

42. Saavedra, J.; Pursell, C. J.; Chandler, B. D. *J. Am. Chem. Soc.* 2018, 140, 3712-3723.

43. Wang, Y.; Widmann, D.; Behm, R. J. *ACS Catal.* **2017**, 7, 2339-2345.

44. Widmann, D.; Behm, R. J. *Angew. Chem*. Int. Ed. **2011**, 50, 10241-10245.

45. Wahlström, E.; Lopez, N.; Schaub, R.; Thostrup, P.; Rønnau, A.; Africh, C.; Lægsgaard, E.; Nørskov, J. K.; Besenbacher, F. *Phys. Rev. Lett.* **2003**, 90, 026101.

46. Mellor, A.; Humphrey, D.; Yim, C. M.; Pang, C. L.; Idriss, H.; Thornton, G. *J. Phys. Chem. C* **2017**, 121, 24721-24725.

47. Subramanian, V.; Wolf, E. E.; Kamat, P. V. *J. Am. Chem. Soc.* **2004**, 126, 4943-4950.

48. Chen, M.; Goodman, D. W. Acc. *Chem. Res.* **2006**, 39, 739-746.

49. Valden, M.; Lai, X.; Goodman, D. W. *Science* **1998**, 281, 1647-1650.

50. Chen, M. S.; Goodman, D. W. *Science* **2004**, 306, 252-255.

51. Zhang, Z.; Tang, W.; Neurock, M.; Yates Jr, J. T. *J. Phys. Chem. C* **2011**, 115, 23848-23853.

52. Wang, J. G.; Hammer, B. *Phys. Rev. Lett.* **2006**, 97, 136107.

53. Duan, Z.; Henkelman, G. *ACS Catal.* **2015**, 5, 1589-1595.

54. Duan, Z.; Henkelman, G. *ACS Catal.* **2018**, 8, 1376-1383.

55. Koga, H.; Tada, K.; Okumura, M. *J. Phys. Chem. C* **2015**, 119, 25907-25916.

56. Green, I. X.; Tang, W.; Neurock, M.; Yates, J. T. *Science* **2011**, 333, 736-739.

57. Vilhelmsen, L. B.; Hammer, B. *Phys. Rev. Lett.* **2012**, 108, 126101.

58. Häkkinen, H.; Abbet, S.; Sanchez, A.; Heiz, U.; Landman, U. *Angew. Chem. Int. Ed.* **2003**, 42, 1297-1300.

59. Madsen, G. K.; Hammer, B. *J. Chem. Phys*. **2009**, 130, 044704.

60. Jing Chung, H.; Yurtsever, A.; Sugimoto, Y.; Abe, M.; Morita, S. *Appl. Phys. Lett.* **2011**, 99, 123102.

Chapter 5

1. Sawada, D.; Sugimoto, Y.; Morita, K. I.; Abe, M.; Morita, S. *Appl. Phys. Lett.* **2009**, *94*, 173117.

2. Zhang, Q.; Li, Y. J.; Wen, H. F.; Adachi, Y.; Miyazaki, M.; Sugawara, Y.; Xu, R.; Cheng, Z. H.; Brndiar, J.; Kantorovich, L.; Štich, I. *J. Am. Chem. Soc.* **2018**, *140*, 15668–15674.

3. Matthey, D.; Wang, J. G.; Wendt, S.; Matthiesen, J.; Schaub, R.; Lægsgaard, E.; Hammer, B.; Besenbacher, F. *Science* **2007**, *315*, 1692–1696.

4. Yoon, Y.; Du, Y.; Garcia, J. C.; Zhu, Z.; Wang, Z. T.; Petrik, N. G.; Kimmel, G. A.; Dohnalek, Z.; Henderson, M. A.; Rousseau, R.; Deskins, N.A. *Chem. Phys. Chem.* **2015**, *16*, 313–321.

5. Tao, J.; Cuan, Q.; Gong, X. Q.; Batzill, M. *J. Phys. Chem. C* **2012**, *116*, 20438–20446.

6. Islam, M. M.; Calatayud, M.; Pacchioni, G. *J. Phys. Chem. C* **2011**, *115*, 6809–6814.

7. Yin, X. L.; Calatayud, M.; Qiu, H.; Wang, Y.; Birkner, A.; Minot, C.; Wöll, C. Diffusion versus desorption: complex behavior of H Atoms on an oxide surface. *Chem. Phys. Chem.* **2008**, *9*, 253–256.

8. Baykara, M. Z.; Mönig, H.; Schwendemann, T. C.; Ünverdi, Ö.; Altman, E. I.; Schwarz, U. D. *Appl. Phys. Lett.* **2016**, *108*, 071601.

9. Enevoldsen, G. H.; Pinto, H. P.; Foster, A. S.; Jensen, M. C.; Hofer, W. A.; Hammer, B.; Lauritsen, J. V.; Besenbacher, F. *Phys. Rev. Lett.* **2009**, *102*, 136103.

10. Wen, H. F.; Li, Y. J.; Arima, E.; Naitoh, Y.; Sugawara, Y.; Xu, R.; Cheng, Z. H., *Nanotechnology* **2017**, *28*, 105704.

11. Marinopoulos, A. G.; Vilão, R. C.; Alberto, H. V.; Gil, J. M. *J. Phys. Condens. Matter* **2018**, *30*, 425503.

12. Kudernac, T.; Ruangsupapichat, N.; Parschau, M.; Maciá, B.; Katsonis, N.; Harutyunyan, S. R.; Ernst, K. H.; Feringa, B. L. *Nature* **2011**, *479*, 208–211.

13. Adachi, Y.; Wen, H. F.; Zhang, Q.; Miyazaki, M.; Sugawara, Y.; Sang, H.; Brndiar, J.; Kantorovich, L.; Štich, I.; Li, Y. J. *ACS Nano* **2019**, *13*, 6917–6924.

14. Minato, T.; Kajita, S.; Pang, C. L.; Asao, N.; Yamamoto, Y.; Nakayama, T.; Kawai, M.; Kim, Y. *ACS Nano* **2015**, *9*, 6837–6842.

15. Nickel, A.; Ohmann, R.; Meyer, J.; Grisolia, M.; Joachim, C.; Moresco, F.; Cuniberti, G. *ACS Nano* **2012**, *7*, 191–197.

Chapter 6

1. Sawada, D.; Sugimoto, Y.; Morita, K. I.; Abe, M.; Morita, S. *Appl. Phys. Lett.* **2009**, *94*, 173117.

2. Blöchl, P. E. *Phys.* **1994**, *50*, 17953.

3. Krukau, A. V.; Vydrov, O. A.; Izmaylov, A. F.; Scuseria, G. E. J. Chem. Phys. **2006**, *125, 224106.*

4. Kresse, G.; Furthmüller, J. *Comput. Mater. Sci.* **1996**, *6*, 15.

5. Perdew; J. P.; Burke. K.; Ernzerhof, M. *Phys. Rev. Lett.* **1996**, *77*, 3865.

6. Dudarev, S. L.; Botton, G. A.; Savrasov, S. Y.; Humphreys C. J.; Sutton, A. P. *Phys. Rev. B* **1998**, *57*, 1505.

7. Deskins, N. A.; Rousseau, R.; Dupuis, M. *J. Phys. Chem.*, **2011**, *C 115*, 7562.

8. Bader, R. F. W., *Atoms in Molecules - A quantum theory*, Oxford University Press, New York, 1990.

9. Giessibl, F. J. *Rev. Mod. Phys.* **2003**, 75, 949.

10. Du, Y.; Deskins, N. A.; Zhang, Z.; Dohnalek, Z.; Dupuis, M.; Lyubinetsky, I. *Phys. Chem. Chem. Phys.* **2010**, *12*, 6337.

11. Wendt, S.; Sprunger, P. T.; Lira, E.; Madsen, G. K.; Li, Z.; Hansen, J. Ø.; Matthiesen, J.; Blekinge-Rasmussen, A.; Lægsgaard, E.; Hammer, B.; Besenbacher, F. *Science* **2008**, *320*, 1755.

12. Zhang, Z.; Lee, J.; Yates Jr, J. T.; Bechstein, R.; Lira, E.; Hansen, J. Ø.; Wendt, S.; Besenbacher, F. *J. Phys. Chem. C* **2010**, *114*, 3059.

13. Setvin, M.; Hulva, J.; Parkinson, G. S.; Schmid, M.; Diebold, U. *Proc. Natl. Acad. Sci.* **2017**, *114*, E2556.

14. Zhang, Z.; Yates Jr, J. T. *Chem. Rev.* **2012**, *112*, 5520.

15. Rahe, P.; Steele, R. P.; Williams, C. C. *Nano Lett.* **2016**, *16*, 911.

16. Kocić, N.; Weiderer, P.; Keller, S.; Decurtins, S.; Liu, S. X.; Repp, J. *Nano Lett.* **2015**, *15*, 4406.

17. Steurer, W.; Fatayer, S.; Gross, L.; Meyer, G. *Nat. Commun.* **2015**, *6*, 8353.

Chapter 7

1. Zhang, Q. Li, Y. J.; Wen, H. F.; Adachi, Y.; Miyazaki, M.; Sugawara, Y.; Xu, R.; Cheng, Z. H.; Brndiar, J.; Kantorovich, L.; Stich, I. *J. Am. Chem. Soc.* **2018**, *140*, 15668-15674.

2. Adachi, Y. Wen, H. F.; Zhang, Q.; Miyazaki, M.; Sugawara, Y.; Sang, H.; Brndiar, J.; Kantorovich, L.; Štich, I.; Li, Y. J. *ACS Nano* **2019**, *13*, 6917-6924

3. Wold, D. J.; Frisbie, C. D. *J. Am. Chem. Soc.* **2000**, *122*, 2970-2971.

4. Zhang, Q.; Wen, H. F.; Adachi, Y.; Miyazaki, M.; Sugawara, Y.; Xu, R.; Cheng, Z.; Li, Y. J. *J. Phys. Chem. C* **2019**, *123*, 22595-22602.

5. Wendt, S.; Sprunger, P. T.; Lira, E.; Madsen, G. K.; Li, Z.; Hansen, J. Ø.; Matthiesen, J.; Blekinge-Rasmussen, A.; Lægsgaard, E.; Hammer, B.; Besenbacher, F. *Science* **2008**, *320*, 1755-1759.

6. Wahlström, E.; Vestergaard, E. K.; Schaub, R.; Rønnau, A.; Vestergaard, M.; Lægsgaard, E.; Stensgaard, I.; Besenbacher, F. *Science* **2004**, *303*, 511-513.

7. Xu, H.; Tong, S. Y. *Surf. Sci.* **2013**, *610*, 33-41.

8. Lira, E.; Hansen, J. Ø.; Huo, P.; Bechstein, R.; Galliker, P.; Lægsgaard, E.; Hammer, B.; Wendt, S.; Besenbacher, F. *Surf. Sci.* **2010**, *604*, 1945-1960.

9. Tan, S.; Ji, Y.; Zhao, Y.; Zhao, A.; Wang, B.; Yang, J.; Hou, J. G. *J. Am. Chem. Soc.* **2011**, *133*, 2002-2009.

10. Matthiesen, J.; Wendt, S.; Hansen, J. Ø.; Madsen, G. K.; Lira, E.; Galliker, P.; Vestergaard, E. K.; Schaub, R.; Lægsgaard, E.; Hammer, B.; Besenbacher, F. *ACS Nano* **2009**, *3*, 517-526.

11. Repp, J.; Meyer, G.; Olsson, F. E.; Persson, M. *Science* **2004**, *305*, 493-495.

12. Gross, L.; Mohn, F.; Liljeroth, P.; Repp, J.; Giessibl, F. J.; Meyer, G. *Science* **2009**, *324*, 1428-1431.

13. Yim, C.; Watkins, M. B.; Wolf, M. J.; Pang, C. L.; Hermansson, K.; Thornton, G. *Phys. Rev. Lett.* **2016**, *117*, 116402.

14. Moses, P. G.; Janotti, A.; Franchini, C.; Kresse, G.; Van de Walle, C. G. *J. Appl. Phys.* **2016**, *119*, 181503.

15. Blum, A. S.; Kushmerick, J. G.; Long, D. P.; Patterson, C. H.; Yang, J. C.; Henderson, J. C.; Yao, Y.; Tour, J. M.; Shashidhar, R.; Ratna, B. R. *Nat. Mater.* **2005**, *4*, 167.

16. Abe, M.; Sugimoto, Y.; Custance, O.; Morita, S. *Nanotechnology* **2005**, *16*, 3029.

17. Wu, S. W.; Ogawa, N.; Nazin, G. V.; Ho, W. *J. Phys. Chem. C* **2008**, *112*, 5241-5244.

18. Schwarz, F.; Kastlunger, G.; Lissel, F.; Egler-Lucas, C.; Semenov, S. N.; Venkatesan, K.; Berke, H.; Stadler, R.; Lörtscher, E. *Nat. Nanotechnol.* **2016**, *11*, 170.

19. Swart, I.; Sonnleitner, T.; Repp, J. *Nano Lett.* **2011**, *11*, 1580-1584.

20. Martínez-Blanco, J.; Nacci, C.; Erwin, S. C.; Kanisawa, K.; Locane, E.; Thomas, M.; Von Oppen, F.; Brouwer, P. W.; Fölsch, S. *Nat. Phys.* **2015**, *11*, 640.

21. Borca, B.; Schendel, V.; Pétuya, R.; Pentegov, I.; Michnowicz, T.; Kraft, U.; Klauk, H.; Arnau, A.; Wahl, P.; Schlickum, U.; Kern, K. *ACS Nano* **2015**, *9*, 12506-12512.

22. Kocić, N.; Weiderer, P.; Keller, S.; Decurtins, S.; Liu, S. X.; Repp, J. *Nano Lett.* **2015**, *15*, 4406-4411.

23. Lira, E.; Wendt, S.; Huo, P.; Hansen, J. Ø.; Streber, R.; Porsgaard, S.; Wei, Y.; Bechstein, R.; Lægsgaard, E.; Besenbacher, F. *J. Am. Chem. Soc.* **2011**, *133*, 6529-6532.

24. Kumagai, T.; Hanke, F.; Gawinkowski, S.; Sharp, J.; Kotsis, K.; Waluk, J.; Persson, M.; Grill, L. *Nat. Chem.* **2014**, *6*, 41.

25. Ternes, M.; González, C.; Lutz, C. P.; Hapala, P.; Giessibl, F. J.; Jelínek, P.; Heinrich, A. J. *Phys. Rev. Lett.* **2011**, *106*, 016802.

Chapter 8

1. Chen, M.; Goodman, D. W. *Acc. Chem. Res.* **2006**, *39*, 739-746.

2. Valden, M.; Lai, X.; Goodman, D. W. *Science* **1998**, *281*, 1647-1650.

3. Hvolbæk, B.; Janssens, T. V.; Clausen, B. S.; Falsig, H.; Christensen, C. H.; Nørskov, J. K. *Nano Today* **2007**, *2*, 14-18.

4. Wahlström, E.; Lopez, N.; Schaub, R.; Thostrup, P.; Rønnau, A.; Africh, C.; Lægsgaard, E.; Nørskov, J. K.; Besenbacher, F. *Phys. Rev. Lett.* **2003**, *90*, 026101.

5. Mellor, A.; Humphrey, D.; Yim, C. M.; Pang, C. L.; Idriss, H.; Thornton, G. *J. Phys. Chem. C* **2017**, *121*, 24721-24725.

6. Matthey, D.; Wang, J. G.; Wendt, S.; Matthiesen, J.; Schaub, R.; Lægsgaard, E.; Hammer, B.; Besenbacher, F. *Science* **2007**, *315*, 1692-1696.

7. Zhang, Q.; Li, Y. J.; Wen, H. F.; Adachi, Y.; Miyazaki, M.; Sugawara, Y.; Xu, R.; Cheng, Z. H.; Brndiar, J.; Kantorovich, L.; Stich, I. *J. Am. Chem. Soc.* **2018**, *140*, 15668-15674.

8. Yurtsever, A.; Fernández-Torre, D.; Onoda, J.; Abe, M.; Morita, S.; Sugimoto, Y.; Pérez, R. *Nanoscale* **2017**, *9*, 5812-5821.

9. Jing Chung, H.; Yurtsever, A.; Sugimoto, Y.; Abe, M.; Morita, S. *Appl. Phys. Lett.* **2011**, *99*, 123102.

10. Zhang, Y.; Pluchery, O.; Caillard, L.; Lamic-Humblot, A. F.; Casale, S.; Chabal, Y. J.; Salmeron, M. *Nano Lett.* **2014**, *15*, 51-55.

11. Zhang, Q.; Wen, H. F.; Adachi, Y.; Miyazaki, M.; Sugawara, Y.; Xu, R.; Cheng, Z. H.; Li, Y. J. *J. Phys. Chem. C* **2019**, *123*, 22595-22602.

12. Vilhelmsen, L. B.; Hammer, B. *ACS Catal.* **2014**, *4*, 1626-1631.

13. Wang, Y. G.; Yoon, Y.; Glezakou, V. A.; Li, J.; Rousseau, R. *J. Am. Chem. Soc.* **2013**, *135*, 10673-10683.

14. Vilhelmsen, L. B.; Hammer, B. *J. Chem. Phys.* **2013**, *139*, 204701.

15. Chen, M. S.; Goodman, D. W. *Science* **2004**, *306*, 252-255.

16. Vilhelmsen, L. B.; Hammer, B. *Phys. Rev. Lett.* **2012**, *108*, 126101.

17. Häkkinen, H.; Abbet, S.; Sanchez, A.; Heiz, U.; Landman, U. *Angew. Chem. Int. Ed.* **2003**, *42*, 1297-1300.

18. Repp, J.; Meyer, G.; Olsson, F. E.; Persson, M. *Science* **2004**, *305*, 493-495.

19. Pawlak, R.; Meier, T.; Renaud, N.; Kisiel, M.; Hinaut, A.; Glatzel, T.; Sordes, D.; Durand, C.; Soe, W. H.; Baratoff, A.; Joachim, C. *ACS Nano* **2017**, *11*, 9930-9940.

20. Lyo, I. W.; Avouris, P. *Science* **1991**, *253*, 173-176.

List of Publications

1. **Quanzhen Zhang**, Huan Fei Wen, Yuuki Adachi, Masato Miyazaki, Yasuhiro Sugawara, Rui Xu, Zhi Hai Cheng, Yan Jun Li. "Electrical Engineering of the Oxygen Adatom and Vacancy on Rutile TiO_2(110) by Atomic Force Microscopy at 78 K." *The Journal of Physical Chemistry C*, 123, 28852-28858, 2019.
2. **Quanzhen Zhang**, Huan Fei Wen, Yuuki Adachi, Masato Miyazaki, Yasuhiro Sugawara, Rui Xu, Zhi Hai Cheng, Yan Jun Li. "Characterization and Reversible Migration of Subsurface Hydrogen on Rutile TiO_2(110) by Atomic Force Microscopy at 78 K." *The Journal of Physical Chemistry C*, 123, 22595-22602, 2019.
3. **Quanzhen Zhang**, Yan Jun Li, Huan Fei Wen, Yuuki Adachi, Masato Miyazaki, Yasuhiro Sugawara, Rui Xu, Zhi Hai Cheng, Ján Brndiar, Lev Kantorovich and Ivan Štich. "Measurement and Manipulation of the Charge State of an Adsorbed Oxygen Adatom on the Rutile TiO_2(110)-1×1 Surface by nc-AFM and KPFM." *Journal of the American Chemical Society*, 140, 15668-15674, 2018.
4. **Quanzhen Zhang**, Huan Fei Wen, Yuuki Adachi, Masato Miyazaki, Yasuhiro Sugawara, Yan Jun Li. "Charge state dependence of oxygen adatom conductance switching on rutile TiO_2(110) by nc-AFM and STM." (To be submitted)
5. **Quanzhen Zhang**, Huan Fei Wen, Yuuki Adachi, Masato Miyazaki, Yasuhiro Sugawara, Yan Jun Li. "Unraveling Charge state and structural fluxionality of Au nanoclusters on oxidized rutile TiO_2(110) by nc-AFM and KPFM." (To be submitted)
6. **Quanzhen Zhang**, Huan Fei Wen, Yuuki Adachi, Masato Miyazaki, Yasuhiro Sugawara, Yan Jun Li. " Investigation of the quantum size effects of Au nanoclusters on rutile TiO_2(110) by nc-AFM and STM." (In preparation)

7. Huan Fei Wen, **Quanzhen Zhang**, Yuuki Adachi, Masato Miyazaki, Yasuhiro Sugawara and Yan Jun Li. “Contrast inversion of O adatom on rutile TiO_2(110)-(1× 1) surface by atomic force microscopy imaging.” *Applied Surface Science*, 505, 144623, 2020.
8. Huan Fei Wen, **Quanzhen Zhang**, Yuuki Adachi, Masato Miyazaki, Yoshitaka Naitoh, Yan Jun Li and Yasuhiro Sugawara. “Direct visualization of Oxygen Reaction with Paired Hydroxyl on TiO_2(110) Surface at 78 K by Atomic Force Microscopy.” *The Journal of Physical Chemistry C*, 122, 17395-17399, 2018.
9. Yuuki Adachi, Huan Fei Wen, **Quanzhen Zhang**, Masato Miyazaki, Yasuhiro Sugawara, Hongqian Sang, Ján Brndiar, Lev Kantorovich, Ivan Štich and Yan Jun Li. "Tip-Induced Control of Charge and Molecular Bonding of Oxygen Atoms on the Rutile TiO_2(110) Surface with Atomic Force Microscopy." *ACS Nano*, 13, 6917-6924, 2019.
10. Huan Fei Wen, Yuuki Adachi, **Quanzhen Zhang**, Masato Miyazaki, Yasuhiro Sugawara and Yan Jun Li. “Identification of Atomic Defects and Adsorbates on Rutile TiO_2(110)-(1×1) Surface by Atomic Force Microscopy.” *The Journal of Physical Chemistry C*, 123, 25756-25760, 2019.
11. Huan Fei Wen, Masato Miyazaki, **Quanzhen Zhang**, Yuuki Adachi, Yan Jun Li and Yasuhiro Sugawara. “Direct observation of atomic step edges on rutile TiO_2(110)-(1×1) surface using atomic force microscopy.” *Physical Chemistry Chemical Physics*, 20, 28331-28337, 2018.
12. Yan Jun Li, Huan Fei Wen, **Quanzhen Zhang**, Adachi Yuuki, Eiji Arima, Yukinori Kinoshita, Hikaru Nomura, Zongmin Ma, Lili Kou, Yoshihiro Tsukuda, Yoshitaka Naitoh, Yasuhiro Sugawara, Rui Xu, Zhihai Cheng. “Stable Contrast Mode on TiO_2(110) Surface with Metal-Coated Tips Using AFM.” *Ultramicroscopy*, 191, 51-55, 2018.

List of Presentations

International Conferences

1. **Quanzhen Zhang**, Huan Fei Wen, Yuuki Adachi, Yoshitaka Naitoh, Yan Jun Li and Yasuhiro Sugawara, "Charge state dependence of O_{ad} conductance switching on rutile TiO_2(110)", The 4th Symposium on "Recent Trends in Analysis Techniques for Functional Materials and Devices, Osaka, Japan, 12.09-10.2019. (**Oral**)
2. **Quanzhen Zhang**, Huan Fei Wen, Yuuki Adachi, Masato Miyazaki, Yan Jun Li and Yasuhiro Sugawara, "Engineering the Subsurface Hydrogen on Rutile TiO_2(110)–(1×1) by nc-AFM/STM at 78 K", The 22nd international conference on Non-Contact Atomic Force Microscopy, Regensburg, Germany, 07.29-08.02.2019. (**Poster**)
3. **Quanzhen Zhang**, Huan Fei Wen, Yuuki Adachi, Yoshitaka Naitoh, Yan Jun Li and Yasuhiro Sugawara, "Measurement and manipulation of the charge state of adsorbed oxygen adatoms on rutile TiO_2(110) surface", ACSIN-14 and ICSPM26, Sendai, Japan, 10.21-25.2018. (**Oral**)
4. **Quanzhen Zhang**, Huan Fei Wen, Yuuki Adachi, Yoshitaka Naitoh, Yan Jun Li and Yasuhiro Sugawara, "Study of the charge states of oxygen adatoms on rutile TiO_2(110) by nc-AFM and KPFM at 78 K", The 21st international conference on Non-Contact Atomic Force Microscopy, Finland, 09.17-21.2018. (**Poster**)
5. **Quanzhen Zhang**, Huan Fei Wen, Yuuki Adachi, Yoshitaka Naitoh, Yan Jun Li and Yasuhiro Sugawara, "Study of the charge states of oxygen adatoms on rutile TiO_2(110) by nc-AFM and KPFM at 78 K", The 6th Japan-China Symposium on Nanomedicine, Matsue, Japan, 05.26-28.2018. (**Poster**)
6. **Quanzhen Zhang**, Huan Fei Wen, Yuuki Adachi, Yoshitaka Naitoh, Yan Jun Li and Yasuhiro

Sugawara, “Discovery of a New Adsorption State of Oxygen Molecules on Rutile TiO_2(110) Surface by NC-AFM”, The 20th international conference on Non-Contact Atomic Force Microscopy, Suzhou, China, 09.25-29.2017. (**Poster**)

7. **Quanzhen Zhang**, Huan Fei Wen, Yuuki Adachi, Yoshitaka Naitoh, Yan Jun Li and Yasuhiro Sugawara, “Identification of Al Atoms Sites on Al_2O_3/NiAl(110) Surface by NC-AFM”, The 2nd Symposium on “Recent Trends in Analysis Techniques for Functional Materials and Devices, Osaka, Japan, 01.12.2017. (**Poster**)

Domestic Conferences

1. **Quanzhen Zhang**, Huan Fei Wen, Yuuki Adachi, Masato Miyazaki, Yasuhiro Sugawara and Yan Jun Li, “Charge state dependence of O_{ad} conductance switching on rutile TiO_2(110)”, The 80th JSAP Autumn Meeting, Hokkaido University, Hokkaido, Japan, 09.18-21,2019. (**Oral**)
2. **Quanzhen Zhang**, Huan Fei Wen, Yuuki Adachi, Masato Miyazaki, Yan Jun Li and Yasuhiro Sugawara, “Engineering the Subsurface Hydrogen on rutile TiO_2(110)–(1×1) by nc-AFM/STM at 78 K”, The 66th JSAP Spring Meeting, Tokyo Institute of Technology, Tokyo, Japan, 03.09-12.2019. (**Oral**)
3. **Quanzhen Zhang**, Huan Fei Wen, Yuuki Adachi, Yoshitaka Naitoh, Yan Jun Li and Yasuhiro Sugawara, “Measurement and manipulation of the charge state of adsorbed oxygen adatoms on rutile TiO_2(110) surface”, The 65th JSAP Spring Meeting, Waseda University, Tokyo, Japan, 03.17-20.2018. (**Oral**)
4. **Quanzhen Zhang**, Huan Fei Wen, Yan Jun Li, “Discovery of a new adsorption state of oxygen molecules on Rutile TiO_2(110) surface by NC-AFM”, 応用物理学会関西支部セミナー「機能性材料・デバイス解析の最前線」Osaka University, Osaka, Japan,

12.05.2017. (**Oral**)

5. **Quanzhen Zhang**, Huan Fei Wen, Yuuki Adachi, Yoshitaka Naitoh, Yan Jun Li and Yasuhiro Sugawara, "Investigation of local surface potential induced by atomic dipole moment on TiO_2(110) surface by Kelvin probe force microscopy", The 64th JSAP Spring Meeting, Pacifico Yokohama, Yokohama, Japan, 03.14-17.2017. (**Oral**)
6. **Quanzhen Zhang**, Huan Fei Wen, Yuuki Adachi, Yoshitaka Naitoh, Yan Jun Li and Yasuhiro Sugawara, "Measurement and manipulation of the charge state of adsorbed oxygen adatoms on rutile TiO_2(110) surface", 関西薄膜・表面物理セミナー　プログラム, Kyoto, Japan, 12.01-02.2017. (**Oral**)

Acknowledgment

First and foremost, I would like to express my deep appreciation to my supervisor Prof. Yan Jun Li and Prof. Yasuhiro Sugawara. They gave me marvelous instructions and exceptional support for my research study in Osaka University.

I thank all the doctoral committee members to review and improve my doctoral dissertation.

My further thanks go to our assistant professor Yoshitaka Naitoh, for giving me lots of valuable advice regarding the experiments and life in Japan.

I would like to express my appreciation to Prof. Lev Kantorovich and Dr. Hongqian Sang from King's College London, Prof. Ivan Štich and Prof. Ján Brndiar from Slovak Academy of Science for their simulation support. Moreover, I thank Huan Fei Wen, Yuuki Adachi and Masato Miyazaki, who shared the same experimental equipment with me, and gave me lots of experimental advice. I give many thanks to the lab members Shanrong Zou, Zhang Qu, Ryo Izumi, Tatsuya Yamamoto, Qiang Zhu, Jiahao Wang, Kousuke Itou, Kouhei Gouda, Miku Hirowatari, Kodai Miyoki, Ikuya Andoh, Kanata Fukuzaka, Hiroki Yamasaki, Syu Makino, Zhaozong Zhang, as well as the students who have graduated. I thank the secretaries of Kyoko Nakagawa and Hinata Yamashita, who helped me a lot in the lab life. I would also like to express my thanks to all my friends, who helped me a lot during my study in Japan.

Last but not least, I appreciate my parents and all the families, who support me and give me deep and selfless love forever!